UNIVERSITY OF OKLAHOMA

GRADUATE COLLEGE

THE APPLICATION OF SPECTRAL ANALYSIS AND ARTIFICIAL INTELLIGENCE METHODS TO WEATHER RADAR

A DISSERTATION

SUBMITTED TO THE GRADUATE FACULTY

in partial fulfillment of the requirements for the

Degree of

DOCTOR OF PHILOSOPHY

By

YADONG WANG
Norman, Oklahoma
2010

THE APPLICATION OF SPECTRAL ANALYSIS AND ARTIFICIAL INTELLIGENCE METHODS TO WEATHER RADAR

A DISSERTATION APPROVED FOR THE
SCHOOL OF ELECTRICAL AND COMPUTER ENGINEERING

BY

Dr. Tian-You Yu, Chair

Dr. Robert Palmer

Dr. Alan Shapiro

Dr. Mark Yeary

Dr. Dusan Zrnić

Acknowledgments

I would like to express my sincere gratitude to all people who have helped, supported and inspired me during my doctoral study.

I want to show my deepest appreciation to my advisor and committee chair, Prof. Tian-You Yu, for his guidance for my research and supervision of my dissertation. His advice and invaluable comments greatly directed my research. I truly appreciate his consistent instruction, help and patience. His perpetual energy and enthusiasm in work deeply motivated me and will continuously inspire me in my carrier.

I would like to acknowledge my committee members, Profs. Mark B. Yeary, Robert Palmer, Alan Shapiro and Dusan Zrnić, who generously contributed their time and effort to my study at the University of Oklahoma. I am very grateful for their support and help. I also want to show my appreciation to Prof. Guifu Zhang for his comment and suggestion about my research.

I would like to acknowledge the support from DOC-NOAA NWS CSTAR program through Grant NA17RJ1227, National Science Foundation through ATM-0532107, the Engineering Research Center Program of the National Science Foundation under NSF Cooperative Agreement EEC-0313747, and the project of advanced tornado detection with WSI/Enterprise Electronics Corporation (EEC). I also would like to thank all the professors and friends in Atmospheric Radar Research Center (ARRC) for their help, the NSSL staff for the collection of level I data and the WFO

in Norman for providing the ground damage survey.

This dissertation would be simply impossible without my family's unflagging love. My parents always encouraged me to pursue my interests and dreams. I would not have the opportunity for the education of a doctoral degree without their unlimited love and support. The last and surely the most, I want to acknowledge my wife Lin and my two loving little boys, Andrew and Daniel for their love, support, encouragement and understanding in dealing with all the challenges I have faced, for always giving me strength and hope.

Contents

List Of Tables

List Of Figures

Abstract

Power spectral density (PSD) of reflectivity and polarimetric variables have the potential to provide the linkage between the dynamics and the microphysical properties of scatterers within the radar resolution volume. The artificial intelligence (AI) methods such as fuzzy logic and neural network have been widely used in weather radar. The main goal of this dissertation is to exploit spectral analysis and AI methods to the two specific areas of tornado detection and the retrieval of microphysical properties of rain-hail mixture.

A novel approach of using both fuzzy logic and neural network, termed neuro-fuzzy tornado detection algorithm (NFTDA), is developed to integrate tornado's shear, spectral and polarimetric signatures for both regular resolution and high resolution with the goal of enhanced and robust detection. The spectral signatures are characterized by spectrum width and three additional parameters derived from the analysis of bispectrum, statistics, and Eigen-ratio. The statistical analysis from numerical simulation and real data has shown that NFTDA provides improved detection compared to the conventional shear-based detection algorithm in terms of probability of detection (POD), false alarm rate (FAR), and detection range. For the retrieval problem, a model of Doppler and polarimetric spectra is first developed for the presence of both raindrops and melting hail. The melting ratio is introduced the first time in the retrieval using weather radar. A genetic algorithm (GA) is introduced to solve the optimization of fitting the observed Doppler and polarimetric spectra to the model. Consequently, the drop size distribution (DSD) of both rain and hail,

the melting ratio, the radial component of ambient wind and spectrum broadening can be retrieved. The retrieval algorithm is demonstrated and tested using numerical simulations.

Chapter 1

Introduction

1.1 Literature Review

Weather radars not only can improve the warnings of severe and hazardous weather, but can also provide important atmospheric information to forecasters and researchers (e.g., Serafin and Wilson 2000; Council 2002). The warning lead time has been increased significantly after the installation of the Weather Surveillance Radar-1988 Doppler (WSR-88D) (Polger et al. 1994; Bieringer and Ray 1996; Simmons and Sutter 2005). The upgrade of the WSR-88D to dual polarization is underway, which can provide benefits such as improved hail detection, better severe thunderstorm warnings, improved rainfall estimation and flood and flash warnings (e.g., Zrnić 2007; Spring et al. 2009). It was reported that enhanced shear signature can be obtained with super-resolution (Brown et al. 2002), which was proposed to be implemented by the WSR-88D (e.g., Torres and Curtis 2007) and is currently available on a number of WSR-88Ds. Enhanced tornado vortex signatures (TVS) with super-resolution have been demonstrated using numerical simulation (Brown et al. 2002).

Reflectivity, mean radial velocity and spectrum width are the three fundamental radar measurements, which are termed Doppler moments (Doviak and Zrnić 1993). Doppler moments have been used in various applications, such as rainrate estimation, tornado detection, clutter filtering and downburst prediction (e.g., Doviak and Zrnić

1993; Mitchell et al. 1998; Sachidananda and Zrnić 2000; Smith et al. 2004). With the capability of dual polarization, microphysical properties of scatterers within radar resolution volume, such as type, size and orientation, can be studied with the help of the polarimetric variables such as differential reflectivity Z_{DR}, differential phase ϕ_{DP}, and cross-correlation coefficient ρ_{hv}. Polarimetric variables have been used to improve several radar applications such as rainrate estimation, drop size distribution (DSD) retrieval, severe hailstorm detection and hydrometeor classification (e.g., Ryzhkov and Zrnić 1996; Bringi and Chandrasekar 2001; Gorgucci et al. 2002; Zrnić et al. 1993; Liu and Chandrasekar 2000). Moreover, polarization variables can help with the diagnosis of supercell thunderstorms, tornado identification and freezing-level estimation etc. (e.g., Kumjian and Ryzhkov 2008; Ryzhkov et al. 2005; Brandes and Ikeda 2004).

The Doppler spectrum, is a power spectral density (PSD) of reflectivity and represents a power-weighted distribution of scatterers' radial velocities within the radar resolution volume. The commonly used Doppler moments are derived from the first three moments of Doppler spectrum. In other words, Doppler spectrum has the potential to provide insight of scatterers' motion within the radar volume. Moreover, the polarimetric spectra of differential reflectivity ($Z_{DR}(v)$), cross correlation coefficient ($\rho_{hv}(v)$) and differential propagation phase ($\phi_{DP}(v)$) for example, can further provide the linkage between the hydrometeors' microphysics and dynamics if their terminal velocities can be Doppler sorted (e.g., Spek et al. 2007; Unal and Moisseev 2004).

Fabry and Keeler (2003) identified spectral processing as one of the trends to enhance the accuracy and sensitivity of weather radar. Spectral processing plays an important role to help in advancing our understanding of the atmosphere, developing new technologies, and improving current algorithms. A tornado vortex was reported to produce bimodal or flattened spectral signatures (Zrnić and Doviak 1975; Zrnić and Istok 1980; Bluestein et al. 1997; Yu et al. 2007). Non-Gaussian Doppler spectra

were observed in a tornadic supercell storm that can be related to strong vertical shears (Yu et al. 2008). Apparent separation between the echoes from clear-air and biological scatterers was observed in the Doppler spectra, Z_{DR} spectra ($Z_{DR}(v)$) and ρ_{hv} spectra ($\rho_{hv}(v)$), which can be used to recover clear-air wind fields (Bachmann and Zrnić 2005). Gaussian model adaptive processing (GMAP) (Siggia and Passarelli 2004) showed better Doppler moment estimation for clutter filtering (Ice et al. 2004). A ground clutter suppression algorithm was developed by Moisseev et al. (2002) based on the different degrees of polarizations for clutter and weather. As a result, improved performance can be obtained even when weather signals have near-zero radial velocities. In addition, Yanovsky et al. (2005) used Z_{DR} spectra to retrieve the turbulence intensity in rain. Furthermore, polarimetric spectra from higher elevation angles offer the possibility of DSD retrieval due to size sorting and the existing relationship between the particles' sizes, shapes and terminal velocities. For example, the rain DSD, turbulence broadening and shape parameters can be retrieved using Doppler spectrum and Z_{DR} (Moisseev et al. 2006). Moreover, the microphysical properties of two types of ice particles above melting layer can be retrieved using the combination of Doppler and Z_{DR} spectra (Spek et al. 2007). The texture of Z_{DR}, ϕ_{dp} and ρ_{hv} spectra exhibits different values for precipitation, clutter and noise. Therefore, these three parameters were combined by fuzzy logic for adaptive clutter filtering and noise suppression (Moisseev and Chandrasekar 2008). Recently, Moisseev and Chandrasekar (2007) developed a classification algorithm for ice particles using both the bulk variables of reflectivity, specific differential phase (K_{DP}), linear depolarization ratio (L_{dr}), and polarimetric spectra of Z_{DR}, ϕ_{DP}, ρ_{hv}.

Doppler and/or polarimetric moments can be used directly to diagnose and detect the weather of interest, but often it is desirable to extract useful information from all the variables. Artificial intelligence (AI) methods such as fuzzy logic and neural network have been widely used in atmospheric radars to integrate all the available

information for detection or estimation. A fuzzy logic approach was proposed to discriminate between clear sky and cloud, and if the clouds are present, to further discriminate between single-layered and multilayered clouds (Baum et al. 1997). Recently, a fuzzy logic algorithm was developed to segregate precipitating from non-precipitating echoes using polarimetric radar observations at C band (Gourley et al. 2007). Kessinger et al. (2003) developed an anomalously-propagated (AP) return filtering algorithm, which can help to improve the estimation of rainfall accumulation. Fuzzy logic methods were also applied to the estimation of the mixing depth of the convective boundary layer with wind profiling radars (Bianco and Wilczak 2002). Moreover, a fuzzy logic method was developed to improve moment estimation while the data are contaminated by birds, aircraft, and range folding (Cornman et al. 1998). The approach of neural network (NN) has been used to solve prediction and estimation problems in weather radar. For prediction, NN was applied to the forcast of damaging winds, tornadoes, and severe-hail size (Marzban and Stumpf 1996, 1998; Marzban and Witt 2001). For estimation, the NN has been applied to improve the rainrate and the retrieval of microphysical properties of precipitation. For example, accurate rainfall rate was estimated using an adaptive NN (Liu et al. 2001). The improved rainfall rate estimation was reported by adding surface data using a NN (Root et al. 2010). Vulpiani et al. (2009) developed a novel algorithm for improving rain DSD retrieval using polarimetric variables based on NN. The combination of NN and fuzzy logic named neuro-fuzzy system has not only the learning capability of NN but also the advantages of the rule-based fuzzy logic system. An novel hydrometeor classification algorithm was developed by Liu and Chandrasekar (2000), where polarimetric variables are considered in a neuro-fuzzy system. Moreover, a genetic algorithm (GA), which is one type of neural networks, shows attractive capability of solving problem of discontinuous, nondifferentiable, stochastic, or highly nonlinear. In this work, a neuro-fuzzy algorithm is developed to improve tornado detection, and

a GA algorithm is introduced to solve the nonlinear optimization of DSD retrieval for the presence of raindrops and melting hail.

The subjective detection of tornadic storms using hook-shape radar returns was first documented by Stout and Huff (1953), and was suggested as an indicator of tornadoes (Fujita 1958). However, Forbes (1981) found that more than half of the tornadoes in his study did not exhibit apparent hook signatures and suggested that hook echoes may not be a reliable indicator. A unique feature of TVS, was first observed by Burgess et al. (1975) and Brown et al. (1978) using a pulsed Doppler radar. The basic idea of the current tornado detection algorithm (TDA) is to search for strong and localized azimuthal shear in the field of mean radial velocities (e.g., Crum and Alberty 1993; Mitchell et al. 1998). However, because of the smoothening effect caused by the radar resolution volume, the shear signature can be significantly degraded if the size of tornado is small compared to resolution volume (Brown and Lemon 1976).

The DSD is one of the most important information to understand the micro-physical property of precipitations, and several DSD retrieval methods using radar data have been developed in the past. The DSD retrieval using VHF Doppler radar was first reported by Wakasugi et al. (1987). In their work, the DSD of precipitation and the background atmospheric parameters such as the mean radial wind and atmospheric turbulence were simultaneously derived from Doppler spectra. Similar to Sato et al. (1990), based on the UHF profiler with vertically incident observations, the ambient air motion and rain DSD can be retrieved by a nonlinear least squares optimization (Williams 2002). It has been shown that using dual-wavelength radar, the DSD of snow can be accurately estimated if the measurements from at least one wavelength is located in a non-Rayleigh region (e.g., Matrosov 1998; Liao et al. 2005). Moreover, a method for rain rate and DSD from polarimetric radar measurements was proposed by Zhang et al. (2001a). Recently, it was reported that

the raindrop size-shape relation and the DSD were retrieved using the combination of Doppler spectrum and the bulk Z_{DR} from a sufficiently high elevation angle (larger than 30^0) (Moisseev et al. 2006). The DSD retrieval becomes more challenging if a mixture of two and more types of precipitations are present because more parameters need to be determined. In Spek et al. (2007), the DSD of both plates and aggregates is retrieved simultaneously by a non-linear fitting to both Doppler and Z_{DR} spectra.

The focus of this research is to exploit the additional information provided by spectral analysis to develop a novel tornado detection algorithm and to retrieve microphysical properties using AI methods.

1.2 Motivations

The main scientific goals of this research are to (1) develop a novel algorithm to improve tornado detection and (2) estimate the melting ratio for the presence of raindrops and hailstones and their DSDs. The motivations for each goal are provide as follows.

The conventional tornado detection algorithm (TDA) searches for gate-to-gate velocity difference (Mitchell et al. 1998), and a prominent tornado feature is identified if the velocity difference is larger than pre-defined thresholds. However, the velocity differences are smoothened by the increasing size of radar volume with range and consequently, missed detection can occur if a tornado is located at far ranges. It was reported that the NSSL TDA has the probability of detection (POD) of 43%, false alarm rate (FAR) of 48%, and critical success index (CSI) of 31% (Mitchell et al. 1998).

Wide and bimodal tornado spectra were observed from both simulations and real data (e.g., Zrnić and Doviak 1975; Zrnić and Istok 1980; Bluestein et al. 1997; Yu et al. 2007). Those results showed that the Doppler spectra from tornadic region have a distinct character that sets these apart from other spectra. Moreover, Yu

et al. (2007) have shown that these distinct features can be maintained while shear signature becomes difficult to identify. In other words, the TSS has the potential in helping tornado detection. In order to apply TSS to tornado detection, they need to be characterized. Another tornado signature from debris observed by polarimetric radars have been reported (e.g., Ryzhkov et al. 2005; Kumjian and Ryzhkov 2008; Bluestein et al. 2006), and can also be used to facilitate or enhance tornado detection. It is desirable to develop an algorithm that can use all the available information with the goal of reliable and robust tornado detection. Moreover, Brown et al. (2002) recently demonstrated that shear signature can be enhanced using half-degree angular sampling (super-resolution) despite slightly increased statistical errors in velocity data.

Compared to legacy resolution associated with Doppler data (radial velocity and spectrum width) on a 250 m-by-1^o grid, super-resolution can provide Doppler data on a 250 m-by-0.5^o grid through finer azimuthal sampling with a smaller effective beamwidth (Brown et al. 2002; Torres and Curtis 2007). To obtain the desired azimuthal resolution and maintain compatibility with existing signal processing functions, the system will collect overlapping signal every 0.5^o (Torres and Curtis 2007). According the setting of WSR-88D, effective beamwidth (θ_b) can be 1.02^o for super-resolution and 1.39^o for legacy resolution, respectively (Brown et al. 2002). Currently, Doppler moments in super-resolution are collected by a number of WSR-88Ds. Therefore, in order to engage with this upgrade of WSR-88D, it is important that the detection algorithm to be developed is capable of handling super-resolution. Additionally, most weather radars only provide Doppler moments. Thus, the detection algorithm to be developed is flexible to take in different combinations of tornado features.

The melting process of hailstones is very important and is related to mircophysics such as terminal velocity, dielectric constant and latent heat transfer. The melting ratio is defined by the ratio of the water fraction over the melting hailstones (Jung

et al. 2007). Simply speaking, one can consider that in the melting process, the water on the surface of the hail core increases as the melting hailstone falls, but the total mass of melting hailstone is conserved. In other words, the shedding and collision of the melting hails are not considered. Since the melting hailstone is water-coated, the water fraction which is associated with higher dielectric constant will increase the hailstone's backscattering cross section during the melting process. However, to our knowledge no algorithm has been developed for the estimation of the melting ratio using weather radar. It is the first time to propose the retrieval of melting ratio using Doppler and Z_{DR} spectra if the radar elevation angle is sufficiently high. Furthermore, the retrieval problem becomes more complicated when the melting hail stones co-exist with raindrops because the number of variables to describe the microphysics increases. In this work, a novel algorithm is developed to retrieve the melting ratio of hailstones in the rain-hail mixture and at the same time, the DSD of raindrops and hailstones using a GA.

1.3 Organization of Dissertation

The main purposes of this study is to explore the application of spectral analysis and AI methods specifically to tornado detection and the retrieval of melting ratio and DSDs for the rain-hail mixture. This dissertation is organized as follows:

- Chapter 2: Doppler and polarimetric Z_{DR} spectra are introduced. The estimation of the two spectra is briefly reviewed. In addition, the bias, standard deviation, and the windowing effect on Doppler spectrum estimator is discussed. The numerical simulation of tornado Doppler spectrum is developed to study the tornado spectral signatures qualitatively.

- Chapter 3: The parameters that can be used to quantify the TSS are developed. The performance of these parameters are statistically analyzed using numerical

simulations developed in Chapter 2. The tornado debris signatures, and the impacts of super-resolution on tornado shear, spectral and debris signatures are also examined.

- Chapter 4: An novel neuro-fuzzy tornado detection algorithm (NFTDA) is developed, which can integrate all existing tornado signatures. In this work, the NFTDA is specifically trained for four different combinations of input features based on (1) availability of feature parameters, (2) performance behavior, and (3) the research values. The performance of NFTDA with both legacy and super-resolution is statistically analyzed and compared to conventional TDA using both simulation and real cases.

- Chapter 5: The application of spectral analysis and GA to retrieve the microphysical properties of rain-hail mixture is introduced. The analytical model of both Doppler and Z_{DR} spectra from the mixture of raindrops and melting hailstones is developed. The relation between the melting ratio and the backscattering cross section is obtained using the 7^{th} order polynomial fitting to the data from T-matrix at C-band. The retrieval problem is formulated as a highly non-linear optimization and is solved using a GA algorithm. The retrieval of the DSDs and melting ratio is demonstrated and tested using numerical simulations. Moreover, the sensitivity of the retrieval algorithm to the input microphysical parameters is analyzed and discussed.

- Chapter 6: A summary of this research is presented. Future work is proposed and discussed.

Chapter 2

Tornado Doppler Spectrum

A pioneering work in the measurement of tornado spectra was done using a 3-cm continuous wave (CW) radar (Smith and Holmes 1961). Atlas (1963) expected a broad and flat spectrum to be observed by a pulsed radar if a tornado is within the radar resolution volume. Although the history of tornado spectrum measurements is long, the number of observed and studied cases is relative small. This is largely because neither the technology to process spectra nor the technology to recored voluminous amounts of time series data were readily available. Analytical simulations have shown that tornado spectral signatures (TSS) with wide and bimodal pattern can be obtained if the tornado is centered close to the radar beam (Zrnić and Doviak 1975). Such wide and bimodal signatures were then verified by both pulsed Doppler radar (Zrnić and Istok 1980; Zrnić et al. 1985) and mobile frequency modulated CW (FM-CW) radar (Bluestein et al. 1993, 1997) with extremely high maximum unambiguous velocity of approximately 90 m s^{-1}. In this work, TSS and TDS is applied to improve the detection of tornado vortices from traditional velocity-based algorithm. Before further investigating tornado Doppler spectrum and its characterization, it is necessary to provide the basic idea of spectrum estimation including the bias, variance and the impact of window function. In this chapter, a review of the Doppler spectrum and the simulation of tornado Doppler spectrum are presented.

This chapter is organized as follows. In section 2.1, a review of Doppler spectrum is presented including the estimation of Doppler spectrum, the bias, variance and the windowing effect in the spectrum estimation. Moreover, the calculation of Z_{DR} spectrum is introduced. In section 2.2, the tornado Doppler spectrum is introduced and the numerical simulation of tornado Doppler spectrum is presented and discussed. Moreover, several factors affecting spectrum shape are analyzed. The summary is presented in section 2.3.

2.1 Review of Doppler Spectrum

2.1.1 Estimation of Doppler spectrum and differential reflectivity spectrum

The Doppler spectrum $S(f)$ is defined as the Discrete Time Fourier Transform (DTFT) of the autocorrelation function $R(l)$:

$$S(f) = \lim_{M\to\infty} T_s \sum_{l=-(M-1)}^{M-1} R(l) e^{-j2\pi f T_s l} \tag{2.1}$$

and the inverse relation can be obtained using the following equation:

$$R(l) = \int_{-1/2T_s}^{1/2T_s} S(f) e^{j2\pi f T_s l} df \tag{2.2}$$

where the Doppler spectrum has a repetitive cycle equal to T_s^{-1}, twice the Nyquist frequency.

The autocorrelation function (ACF) of a complex wide-sense-stationary signal is defined as:

$$R(l) = \lim_{M\to\infty} \frac{1}{M} \sum_{m=0}^{M-|l|-1} V^*(m) V(m+l) \tag{2.3}$$

where $V(m)$ is the complex voltage of the mth sample. For a finite number of samples, the estimate of autocorrelation $\hat{R}(l)$ (the caret is used to denote estimator) is obtained using the following equations:

$$\hat{R}(l) = \begin{cases} \frac{1}{M} \sum_{m=0}^{M-|l|-1} V^*(m)V(m+l) & \text{for} \quad |l| \leq M-1 \\ 0 & \text{otherwise} \end{cases} \tag{2.4}$$

Two methods are commonly used to estimate the Doppler spectrum (power spectral density). The first method is termed the Blackman-Tukey method. Using this method, the power spectrum estimate can be obtained using Eq. (2.1) and the estimate $\hat{R}(l)$ in Eq. (2.4):

$$\hat{S}_1(f) = T_s \sum_{l=-(M-1)}^{M-1} \hat{R}(l) e^{-j2\pi f T_s l} \tag{2.5}$$

The other one named periodogram uses the DTFT to compute $\hat{S}_2(f)$ directly from the data:

$$\hat{S}_2(f) = |Z(f)|^2 T_s / M \tag{2.6}$$

where $Z(f)$ is the DTFT of the complex signals $V(m)$.

$$Z(f) = \sum_{m=0}^{M-1} V(m) e^{-2j\pi f T_s m} \tag{2.7}$$

It can be shown in the following derivation that the two methods of spectrum estimation are identical.

$$\begin{aligned} \hat{S}_2(f) &= \tfrac{T_S}{M} \left[\sum_{m=0}^{M-1} V^*(m) e^{j2\pi f T_s m} \sum_{n=0}^{M-1} V(n) e^{-j2\pi f T_s n} \right] \\ &= \tfrac{T_s}{M} \sum_{m=0}^{M-1} \sum_{n=0}^{M-1} V^*(m)V(n) e^{-j2\pi f T_s (n-m)} \\ &= T_s \sum_{l=-(M-1)}^{M-1} \hat{R}(l) e^{-j2\pi f T_s l} \\ &= \hat{S}_1(f) \end{aligned} \tag{2.8}$$

where $l = n - m$. The equivalence between these two equations indicate that we do not need to estimate the ACF. Instead, Doppler spectrum can be estimated more efficiently by applying FFT to the time series data (periodogram).

The differential reflectivity spectrum can be estimated as (Yanovsky et al. 2005; Bachmann and Zrnić 2005, 2006):

$$Z_{DR}(f) = 10 \times \log_{10} \frac{S_{hh}(f)}{S_{vv}(f)} + C \qquad \text{(dB)} \tag{2.9}$$

where $S_{hh}(f)$ and $S_{vv}(f)$ are the Doppler spectra obtained with horizontally and vertically polarized waves, respectively, and C is the calibration constant that accounts for the difference in the system gains of the two channels. It should be noted that normally the $S_{hh}(f)$ is represented by $S(f)$.

2.1.2 Quality of Spectrum Estimates

Bias and variance are the two fundamental attributes for measuring the quality of the estimators. If $E[\hat{S}_2(f)] = S(f)$, $\hat{S}_2(f)$ is unbiased, where $S(f)$ is the true spectrum. The bias and variance of periodogram estimation have been derived in Doviak and Zrnić (1993). In order to investigate the impact of window function on the spectrum estimation, the finite segment of complex sequence $V_M(m)$ is introduced as (Doviak and Zrnić 1993):

$$V_M(m) = V(m)d(m) \tag{2.10}$$

where

$$d(m) = \begin{cases} 1 & 0 \le m \le M-1 \\ 0 & \text{otherwise} \end{cases} \tag{2.11}$$

The weighting sequence $d(m)$ is referred to as the data window because it has only a finite portion (of length M) of the infinite sequence $V(m)$. With $V_M(m)$ expressed by Eq. (2.10), the expectation of Eq. (2.6) can be written as:

$$\begin{aligned} E[\hat{S}_2(f)] &= \frac{T_S}{M} \left[\sum_{l=-(M-1)}^{M-1} \sum_{m=0}^{M-1-|l|} d^*(m)d(m+1)E[V^*(m)V(m+1)]e^{-j2\pi f T_s n} \right] \\ &= T_s \sum_{l=-(M-1)}^{M-1} R(l)e^{-j2\pi f T_s l} \sum_{m=0}^{M-1-|l|} \frac{d^*(m)d(m+1)}{M} \\ &= T_s \sum_{l=-(M-1)}^{M-1} w(l)R(l)e^{-j2\pi f T_s l} \end{aligned} \tag{2.12}$$

Note we have assumed $V(m)$ to be wide-sense stationary (WSS), which means that $E[V(m)V^*(m+l)]$ is independent of m (only a function of l). Therefore, only the data window product is summed over m. The sum of data window products is the correlation of the data window samples and is called the lag window $w(l)$ (Doviak and Zrnić 1993):

$$w(l) = \frac{1}{M} \sum_{m=0}^{M-1-|l|} d^*(m)d(m+l) \tag{2.13}$$

If a rectangular data window function is used, a triangular (i.e., Bartlett) lag window function will be produced:

$$w(l) = \begin{cases} 1 - \frac{|l|}{M} & -M \leq l \leq M \\ 0 & \text{otherwise} \end{cases} \tag{2.14}$$

By substituting Eq. (2.14) into Eq. (2.12), the expected value of spectrum estimate can be rewritten in the following form:

$$E[\hat{S}_2(f)] = T_s \sum_{-(M-1)}^{M-1} (1 - \frac{|l|}{M}) R(l) e^{-j2\pi f T_s l} \tag{2.15}$$

Eq. (2.15) equals the true spectrum of Eq. (2.1) only if $M \to \infty$. Therefore the periodogram is a biased estimate of the Doppler spectrum (or asymptotically unbiased). However the bias can be reduced by collecting longer data set (i.e., larger M).

If the in-phase and quadrature components of $V(m)$ are assumed to be zero-mean white Gaussian distribution, the variance of periodogram estimate is derived in Doviak and Zrnić (1993) as shown in the following equation.

$$\text{var}[\hat{S}_2(f)] = E^2[\hat{S}_2(f)] \tag{2.16}$$

It is clear that unlike the bias, the variance is not reduced by a longer data set. However, the variance can be decreased through averaging a number of spectrum estimates:

$$\hat{S}_{av}(f) = \frac{1}{N} \sum_{n=1}^{N} \hat{S}_2^n(f) \tag{2.17}$$

where $\hat{S}_2^n(f) = \frac{T_s}{M}|\sum_{m=0}^{M-1} V_n(m)e^{-j2\pi fmT_s}|^2$. Each $V_n(m)(n = 1, 2, ..., N)$ is a M point data sequence. If $\hat{S}_2^n$ are independent of each other, then the variance can be decreased as:

$$\text{var}[\hat{S}_{av}(f)] = \frac{\text{var}[\hat{S}_2(f)]}{N} \tag{2.18}$$

2.2 Doppler Spectrum From Tornado Vortices

2.2.1 Observations of tornado spectra

The Doppler spectrum for weather is defined by the following equation (Doviak and Zrnić 1993).

$$S(\mathbf{r_0}, v) = \int_{v=\eta} CW_r^2(\mathbf{r}) f_b^4(\theta) Z(\mathbf{r}) |\nabla v(\mathbf{r})|^{-1} ds_1 ds_2 \tag{2.19}$$

where $\mathbf{r_0}$ is a vector in 3D space, C is a parameter that is a function of radar wavelength, peak transmitted power, range, and antenna gain, $W_r^2(\mathbf{r})$ is the range weighting function, $f_b^4(\theta)$ is the two-way antenna pattern, $Z(\mathbf{r})$ and $v(\mathbf{r})$ are the reflectivity and radial velocity fields, respectively, and ds_1 and ds_2 are two orthogonal differential lengths on the surface of a constant v (isodop). The radar is located at the origin and radar resolution volume is centered at $\mathbf{r_0}$. The term of velocity gradient is used to adjust the density of scatterers between the two isodop surfaces. The magnitude of Doppler spectrum represents the return power from all the scatterers within the radar resolution volume that have the same radial velocity. The mean Doppler velocity and spectrum width are defined from the first and second moments of a Doppler spectrum (Doviak and Zrnić 1993). Note that $f = -\frac{2v}{\lambda}$, where f, v and λ is the Doppler frequency, radial velocity and wavelength in Hz, m s^{-1} and m, respectively.

Recently, Yu et al. (2007) reported that tornado spectra observed from systems and setting that are similar to the operational WSR-88D are often flat, similar to a white noise spectrum but with significant signal-to-noise ratio (SNR). These results have shown that the Doppler spectra from tornadic regions have a distinct character

that sets these apart from other spectra. To study tornado spectrum quantitatively, numerical simulations of tornado spectrum are performed in the following section.

2.2.2 Numerical simulation of tornado spectra

To fully understand the characterization of tornado Doppler spectra under different situations such as different size/range, multiple vortexes, background wind, shear environment etc., the numerical simulation of tornado spectra developed by Yu et al. (2007) is adopted in this work. To simplify the problem, in the simulation it is assumed that the reflectivity and velocity are independent of height. In addition, the velocity field of each vortex is modeled by a combined Rankine vortex (Kundu and Cohen 2002). A virtual WSR-88D with 1.39^o effective beamwidth (θ_b) and 250-m range resolution was used. Consequently, the Level I time series data are generated with desirable SNR and the three spectrum moments are estimated using the autocovariance method (Doviak and Zrnić 1993). Under the assistance of this simulation tool, the signatures of tornado spectra under different situation, such as range, reflectivity structure and shear environment can be understood clearly.

2.2.2.1 Simulation approach

A Doppler spectrum represents the power weighted radial velocity distribution of scatterers within the radar volume. The magnitude of Doppler spectrum at a velocity v is the return power from all scatterers with the same radial velocity v. The received power from each scatterer is determined by the reflectivity and radar weighting function at the scatterer's location. For a maximum unambiguous velocity of V_a, the velocity bins are defined as $v_k = -V_a + k\Delta v, k = 1, 2, ...M$, where $\Delta v = 2V_a/M$. The maximum unambiguous velocity is determined by $V_a = \lambda/(4T_s)$, where T_s is the pulse repetition time. For given reflectivity and velocity fields, the Doppler spectrum $S(v)$ can be simulated by summing the return power from scatterers of radial velocity

v within the radar resolution volume. In this work, it is assumed that the reflectivity and velocity are independent of height. As a result, only 2D horizontal fields are considered. An example of reflectivity and velocity fields are shown in Fig. 2.1.

The size of radar volume centered at r_0 is defined by the range weighting function W_r^2 and antenna pattern $f_b^4(\theta)$ in range and azimuth, respectively, as depicted by the white box. Each radar volume consists of 1500×500 grid points in the x and y directions, respectively. A Doppler spectrum was simulated using the following equation:

$$S(r_0, v) = \sum_i \sum_j W_r^2(i,j) f_b^4(i,j) Z(i,j) \tag{2.20}$$

summation only for $v - \frac{\Delta v}{2} \leq v_r(i,j) < v + \frac{\Delta v}{2}$, where r_0 is the center of radar volume, i and j are indices for the grid points in the x and y directions, and $Z(i,j)$, $W_r^2(i,j)$ and $f_b^4(i,j)$ are the reflectivity, range weighting function, and two-way antenna pattern at Cartesian grid. In this work, the reflectivity pattern associated with a tornado vortex is modeled by the following equation (Zrnić and Doviak 1975):

$$Z(i,j) = Z_m \exp\left[\frac{-1}{2}\left(\frac{r_{ij} - r_{0z}}{W_z}\right)^2\right] \tag{2.21}$$

where Z_m is the maximum reflectivity, r_{0z} is the radius of maximum reflectivity, W_z is the width of reflectivity, and r_{ij} is the distance between the grid point (i,j) and the center of tornado. Therefore, a doughnut-shaped reflectivity can be produced.

Moreover, a uniform reflectivity and a Gaussian-shaped reflectivity can be obtained by setting $W_z \approx \infty$, and $r_{0z} = 0$, respectively. An example of Gaussian-shaped reflectivity is presented in Fig. 2.1. A reflectivity pattern for multiple vortices can be obtained by the superposition of each individual reflectivity pattern. At each grid, the radial velocity is given by the following equation:

$$V = V_0 + V_s + \bar{V} \tag{2.22}$$

where $V_0 = [u_0, v_0, w_0]$ is the uniform background flow in the radial direction; V_s is the contribution by the 2D horizontal shear; and $\bar{V}$ is the radial velocity from

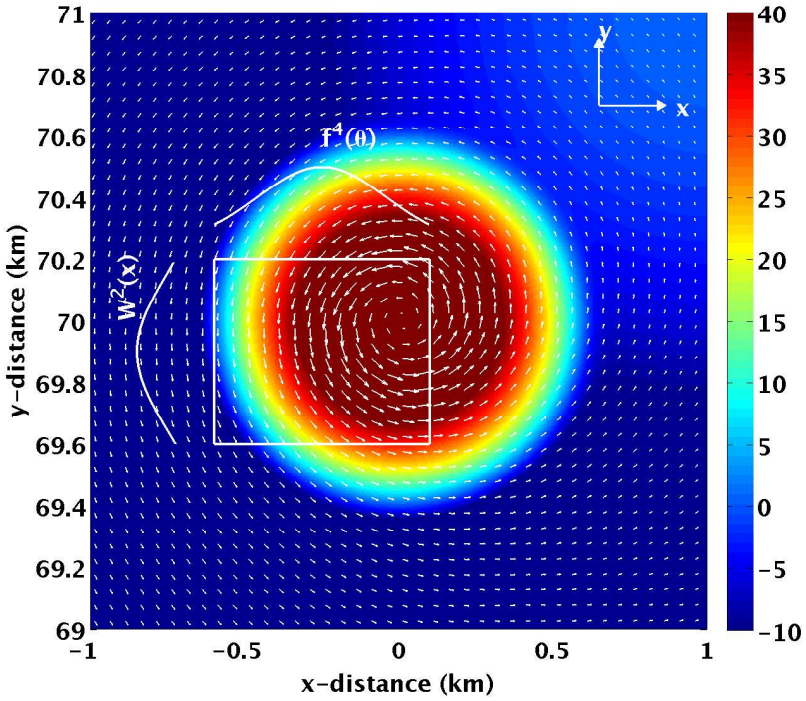

Figure 2.1: A schematic diagram to demonstrate the simulation of Doppler spectrum. The reflectivity pattern is depicted by color contour and the horizontal wind field is denoted by the arrows.

one or multiple vortices. A tornado is simulated using a vortex with given radius R, maximum tangential velocity V_T, and maximum radial velocity V_R. If $v(i,j)$ is outside the range of $(-V_a, V_a)$ (velocity aliasing), then it will be adjusted by $v(i,j) \pm 2nV_a$ until it is between $(-V_a, V_a)$. Consequently, the Doppler spectrum at radial velocity v is the sum of $W_r^2(i,j) f_b^4(i,j) Z(i,j)$ at those grids with radial velocity between $v - (\Delta v/2)$ and $v + (\Delta v/2)$. The resultant spectrum is defined as the model spectrum. A similar scheme was used by Bluestein et al. (1993) to simulate Doppler spectrum and by Brown and Wood (1991) and Wood and Brown (1997) to simulate the mean Doppler velocity.

The complex time series signals are obtained by taking an inverse Fourier transform of the model spectrum and noise as described in Zrnić (1975). The three spectrum moments (signal power, mean Doppler velocity, and spectrum width) can be estimated using either autocovariance or spectral method (Doviak and Zrnić 1993). The proposed simulation scheme has a number of attractive features: 1) it can include more general environmental conditions such as background flow, shears and multiple vortices; 2) time series data that can be used to test various signal processing techniques are generated; 3) it provides desirable statistics of the three moment estimates, which can be used to investigate the statistical performance of a new detection algorithm; 4) a realistic noise corruption is simulated; 5) the velocity aliasing is also simulated in a realistic manner.

Note that the approach used in this work is flexible enough to simulate other types of radars such as the Collaborative Adaptive Sensing of the Atmosphere (CASA) radars (e.g., Brotzge et al. 2005). Moreover, different vortex model such as Burgers-Rott, which has been shown to better describe some tornado vortexes (e.g., Bluestein et al. 2003), can also be implemented.

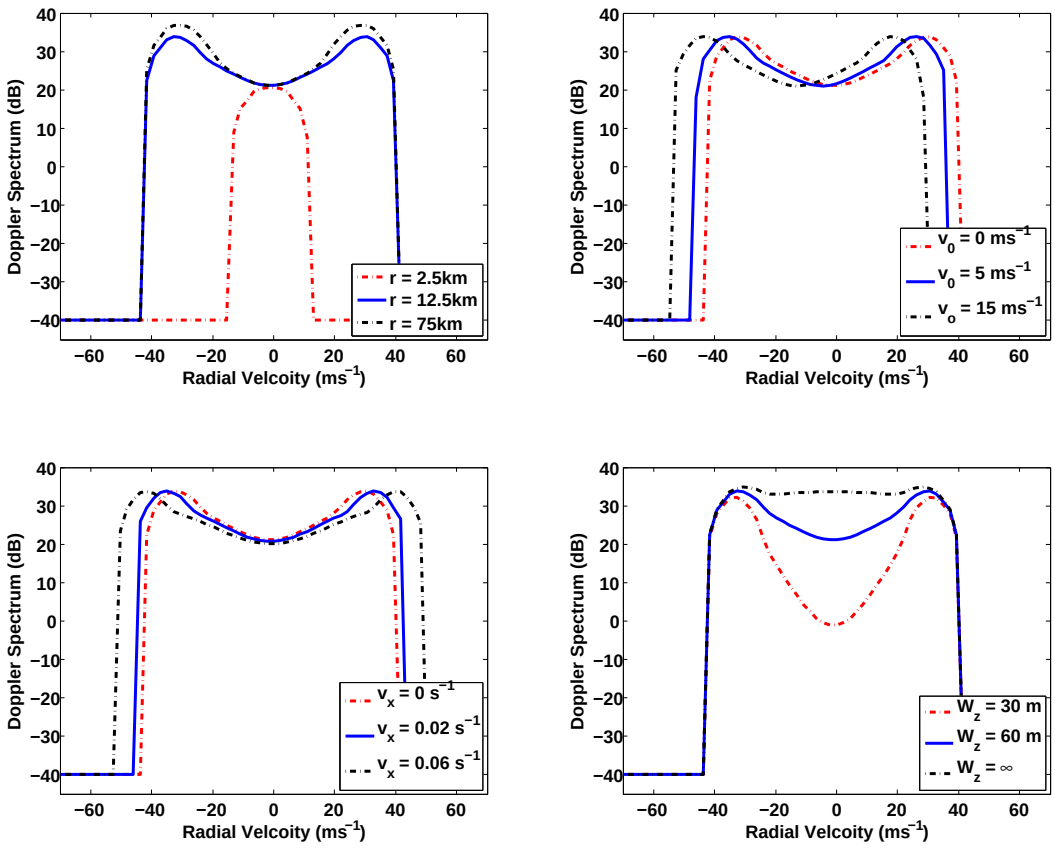

Figure 2.2: A demonstration of tornado spectra as a function of range (r_0), uniform background wind (v_0), horizontal shear (v_x), and the width of reflectivity (W_Z). A tornado-like vortex with maximum tangential wind of 50 m s^{-1} and a radius of 200 m is located at the north of the radar at range r_0.

2.2.2.2 Sensitivity analysis of tornado Doppler spectrum

Dependence of tornado spectra on the range, background wind, horizontal shear, and reflectivity structure is demonstrated in Fig. 2.2. To investigate the impact of these four factors on a spectrum, only one parameter changes for each of these cases. In the simulation the default mean background flow is zero ($v_o = u_0 = 0$ m s^{-1}) and no shear is presented ($v_x = dv/dx = 0$ s^{-1}, $u_y = du/dy = 0$ s^{-1}). The reflectivity of the tornado is simulated using Eq. (2.21) with $W_z = 60$ m and $r_{oz} = 220$ m. As a result, a pattern of low reflectivity surrounded by high reflectivity (i.e. doughnut-shaped reflectivity) is produced, whereby the location of maximum reflectivity is slightly outside the tornado core (Dowell et al. 2005). Therefore, the r_{oz} of 220 m is invariant in this work. No mesocyclone is included in this case. The maximum unambiguous velocity (V_a) is set as 90 m s^{-1} such that no velocity aliasing occurs. Moreover, the radar resolution volume is collocated with the center of the vortex. Ideal tornado spectra at three different ranges ($r_0 = 2.5$, 12.5 and 75 km) are shown on the top left of Fig. 2.2. Note that the statistical fluctuation in Doppler spectrum (Zrnić 1975) is not included in this case for the purpose of clear demonstration although a constant noise level of -40 dB (associated with SNR of 40 dB) is used. It can be observed that the tornado spectrum become wider and bimodal when the range increase from 2.5 to 12.5 km. If the tornado is close to the radar (2.5 km in this study), only the center portion with small velocities of the tornado is sampled by the radar resolution volume. Therefore, the velocity components above 20 m s^{-1} and below -20 m s^{-1} can not be observed (depicted by red line). Larger velocity components can be observed due to the increase of radar resolution volume with range (blue and black lines), until the maximum radial velocity from the vortex is reached. After that, the dependence of spectrum pattern on range is relatively small as shown in the figure for range increases from 12.5 to 75 km. The results are consistent with previous results presented by Zrnić and Doviak (1975) in which a different simulation approach was used. On the top right panel,

Doppler spectra from a tornado within a horizontal flow at 12.5 km with magnitude of 0, 5, and 15 m s^{-1} are shown. It is clear that the constant background wind shifts the spectrum by its radial component without varying the spectrum pattern. Therefore, it is desirable that the parameter characterizing TSS is not sensitive to the shift of the pattern. Several reasons could cause the Doppler spectrum broadening. Because the cited spectral broadening mechanisms are independent of one another, the square of the spectrum width σ_v^2 can be considered as a sum of contributions by each as (Doviak and Zrnić 1993):

$$\sigma_b^2 = \sigma_s^2 + \sigma_\alpha^2 + \sigma_o^2 + \sigma_t^2 \tag{2.23}$$

where σ_s^2 is due to shear, σ_α^2 to antenna motion, σ_o^2 to change in orientation or vibration of hydrometeors and σ_t^2 to turbulence (Doviak and Zrnić 1993). The spectrum broadening caused by shear is shown in the lower left panel. It is clear how horizontal shear changes spectrum. On the lower right panel, the results exhibit that different reflectivity structures do not change the maximum radial velocity, but can have a significant impact on the shape of the tornado spectrum. In this study, uniform reflectivity ($W_z = \infty$), wide ($W_z = 60$) and narrow ($W_z = 30$) band doughnut shape reflectivity are simulated. Approximately rectangular shape spectrum is obtained from uniform reflectivity. With the decreasing of the doughnut band (W_z), Doppler spectrum becomes more bimodal (double peaks) shape. Note that other factors such as the location of the tornado within the radar resolution volume and velocity aliasing can further alter the spectrum shape. In practice the statistical fluctuations in the spectrum is inevitable and could degrade the signatures. Moreover, a spectrum is obtained by signals from a 3D radar resolution volumes, and therefore the spectrum shape will also depend on the vertical profile of reflectivity and velocity distribution within the radar resolution. Several high-resolution vertical profiles of tornado structure have been reported using mobile Doppler radar (e.g., Wurman and Gill 2000). The Doppler spectrum from a 3D radar volume can be considered as the

super-position of the spectra from the 2D simulations at a number of heights within the radar volume that are weighted by the antenna pattern in the vertical direction.

To further demonstrate the unique features of tornado spectrum, an idealized tornado within a mesocyclone is simulated. The model reflectivity and horizontal velocity fields are shown in the upper left panel of Fig. 2.3. Both the tornado and mesocyclone are modeled by the Rankine vortex with a core radius of 200 m and 2 km, respectively. The center of the tornado and mesocyclone are separated by 1 km. The maximum tangential velocity for the tornado and mesocyclone is 50 and 25 m s^{-1}, respectively, and a maximum radial velocity of 5 m s^{-1} is used for both vortices. The reflectivity structures associated with the mesocyclone and tornado are simulated by a Gaussian and doughnut-shaped functions, respectively. The effective beamwidth (θ_b) and angular sampling ($\Delta\theta$) are set as 1.39 ^{o}, and 1.0 ^{o}, which are typically used by WSR-88D (Brown et al. 2002). Spectra from five consecutive radials and ranges observed by a virtual WSR-88D from the tornadic region, as specified by the white box in the top of Fig. 2.3 are shown in decibels in the lower panels. The center of tornado is located at r_o = 25 km and $\phi_o = 0$ ^{o}, where r_o is the range and ϕ_o is the azimuth angle of radar beam. The maximum unambiguous velocity is 35 m s^{-1}, and therefore velocity aliasing occurs. Moreover, a constant noise level of -55 dB (associated with SNR of 50 dB) with the statistical fluctuations is simulated to generate 64 time series data points using the scheme proposed by Zrnić (1975). The mean Doppler velocities are also indicated in each spectrum by the location of triangles. In addition, the inbound and outbound directions are denoted by downward and upward triangles, respectively. Note that no apparent bimodal signature is observed given V_a = 35 m s^{-1} due to velocity aliasing. Spectra similar to white noise can be observed in azimuthal direction from -1 ^{o} to 1 ^{o}, and range from 24.75 km to 25.25 km. Obvious velocity aliasing can be observed at (-1^o, 25 km), (-2^o, 24.75 to 25.25 km), (1^o, 25.5 km) and (1^o, 24.5 km). Although the estimated radial mean velocity from the center

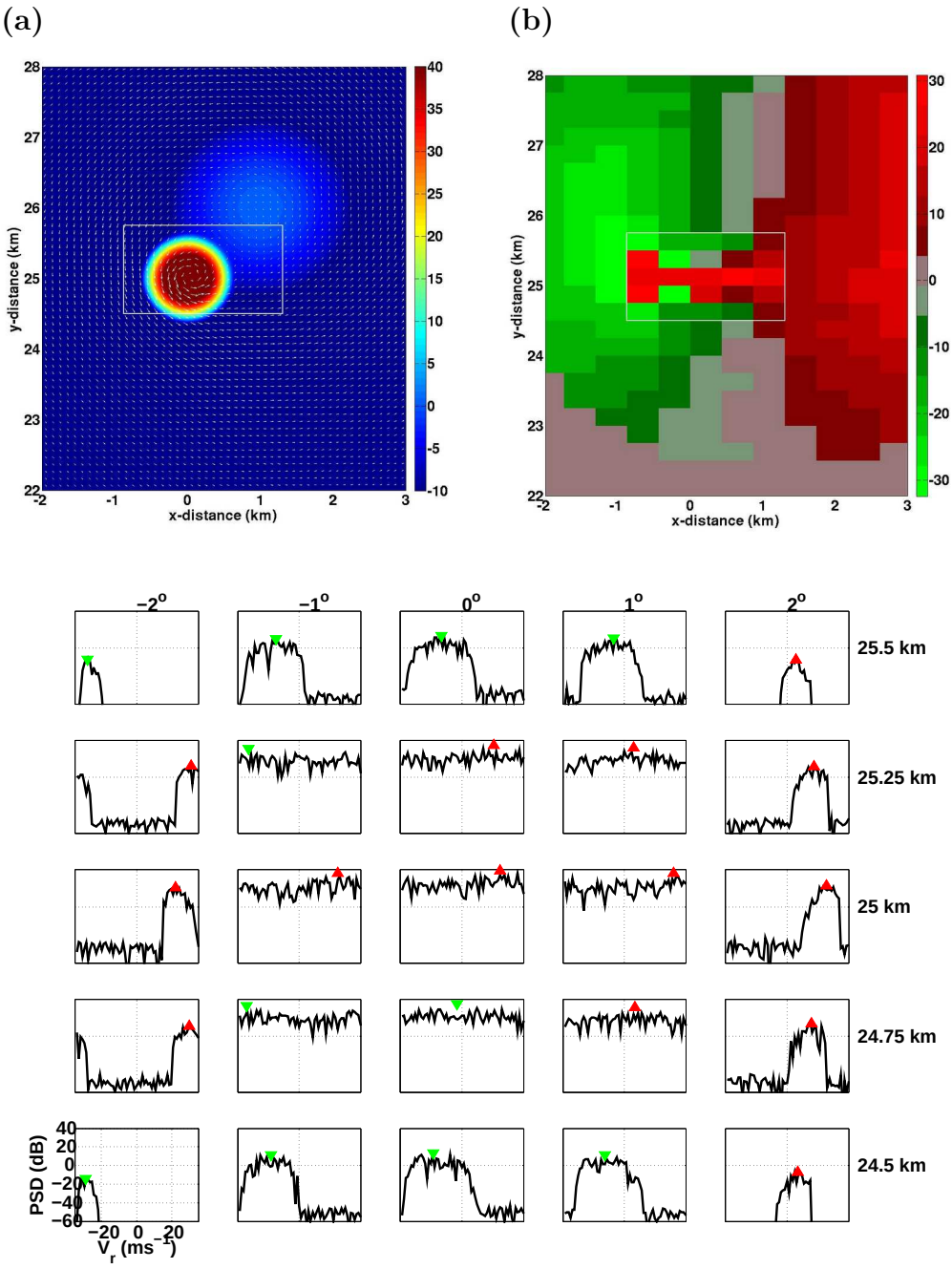

Figure 2.3: (a) Model reflectivity and horizontal wind field. The tornado is located at 25 km north from the radar and a mesocyclone is centered at 1 km northeast from the tornado. (b) The velocity field observed by a virtual WSR-88D. (bottom) Spectra from the region of tornado vortex, denoted by a block box.

of tornado (0^o, 25 km) shows large positive value (> 20 m s^{-1}), large variation is expected caused by the fluctuation.

2.3 Summary

The Doppler spectrum was introduced in this chapter, and its properties in terms of bias and variance, and the impact of window functions on the estimation of Doppler spectrum was reviewed and discussed. Since the periodogram method shows equivalence to the Blackman-Tukey method but is more efficient in computation, the periodogram will be used in later part of this dissertation. Moreover, the numerical simulation of tornado Doppler spectrum was developed. The dependence of spectrum on range, background wind, shear, and reflectivity structure was investigated. When the ambiguous velocity is large (90 m s^{-1} in the simulation), a wide and bimodal Doppler spectrum is obtained from a tornado. This feature can be maintained under different background wind, shear environment, and at relative far ranges. When the maximum unambiguity velocity is low (35 m s^{-1} for example), the tornado Doppler spectrum becomes more flattened due to the velocity aliasing. This wide and bimodal feature can separate a tornado spectrum from other typical Gaussian spectra, and make the application of tornado spectrum to tornado detection possible. In order to take advantages of the wide and bimodal tornado spectrum signatures in tornado detection, parameters that can quantify these features need to be developed, which will be discussed in next chapter.

Chapter 3

Tornado Spectral Signatures (TSS) and Tornado Debris Signatures (TDS)

In Chapter 2, broad and bimodal tornado spectral signatures (TSS) have been shown using simulations. Such features have also been observed by pulsed Doppler radar (Zrnić and Istok 1980; Yu et al. 2007). It was shown that some TSS can be maintained at far ranges which have the potential to facilitate tornado detection (Yu et al. 2007).

The upgrade of WSR-88D network to dual polarization supported by the National Weather Service (NWS) began in late 2009 and was planned to be accomplished about 1.5 years later (Zrnić 2007). Polarimetric variables can provide information about the scatterers' shape, size, and orientation, which can be used for retrieving drop size distribution, classifying the types of hydrometeors, and improving rainfall rate estimation, for example (e.g., Spek et al. 2007; Liu and Chandrasekar 2000; Ryzhkov and Zrnić 1996). Tornado debris signatures (TDS) defined as anomalously low values of cross-correlation coefficient ρ_{hv} and very low (or negative) differential reflectivity Z_{DR} were observed by an S-band polarimetric radar (Ryzhkov et al. 2005). This is because debris typically can have large size, very irregular nonspherical shapes, a high refractive index, and low degree of common alignment. Kumjian and Ryzhkov (2008) and Bluestein et al. (2006) further identified TDS during tornadic supercell storms using an S-band and a mobile X-band dual-polarization Doppler radars.

These tornado spectral and polarimetric signatures have the potential to improve tornado detection and need to be carefully examined. Therefore, in this chapter TSS and TDS observed by S-band weather radars will be characterized quantitatively and investigated systematically for both legacy and super-resolutions. This chapter is organized as follows: In section 3.1, the tornado spectral signatures are introduced and quantified by four parameters. In section 3.2, the tornado debris signatures are examined using real tornado cases. In section 3.3, the impact of super-resolution on tornado velocity signature, spectral signature and debris signatures are investigated through simulation and analysis of real cases. Finally, the conclusions are given in section 3.4.

3.1 Tornado Spectral Signatures

3.1.1 Characterization of tornado spectral signatures

The shape of tornado Doppler spectrum influenced by the distribution of reflectivity and velocity, and by radar sampling. It has been shown in Chapter 2 that spectra from a tornadic region can significantly deviate from a well-defined Gaussian shape. These spectra are of primary interest and could have the potential to facilitate the detection of tornado vortices if TSS can be characterized and quantified with appropriate parameters. In this work, four feature parameters are defined and discussed now.

3.1.1.1 Spectrum width

An intuitive parameter to characterize TSS is the spectrum width (σ_v), which is the square root of the spectral second moment about the mean and is derived by considering the normalized Doppler spectrum as a probability density function (PDF) of the radial velocity v. The second moment quantifies the spread of the velocity

distribution. The spectrum width can be estimated using autocovariance method (Doviak and Zrnić 1993):

$$\hat{\sigma_v} = \frac{\lambda}{2\pi T_s \sqrt{2}} \left| \ln(\frac{\hat{S}}{|\hat{R}_1|}) \right|^{1/2} \text{sgn} \left[\ln \left(\frac{\hat{S}}{|\hat{R}_1|} \right) \right] \tag{3.1}$$

The signal power estimate is obtained by subtracting the known noise power from the average of the squares of the magnitudes.

$$\hat{S} = \frac{1}{M} \sum_{k=0}^{M-1} |V(k)|^2 - N \tag{3.2}$$

The autocorrelation estimate $\hat{R}_1$ at lag T_s is given by:

$$\hat{R}(T_s) = \frac{1}{M} \sum_{m=0}^{M-1} V^*(m) V(m+1) \tag{3.3}$$

However, spectrum width has inherent limitations in characterizing TSS. First of all, spectrum width does not provide sufficient information about the shape of the spectrum. In the covariance method, a Gaussian-shaped spectrum is assumed for the estimation of spectrum width. Moreover, spectrum width estimate can be significantly biased at large spectrum widths and should be used with caution. Additionally, the spectrum width estimate is also sensitive to the accuracy of the noise estimation (Doviak and Zrnić 1993). Three additional parameters that can characterize TSS are developed in the following sections.

3.1.1.2 Spectral flatness

It has been demonstrated in Fig. 2.3 that some tornado spectra are similar to white noise spectra when velocity aliasing occurs. The spectral flatness, σ_s, is defined in the following equation to quantify the flatness of the spectrum.

$$\sigma_s = \frac{1}{M-1} \sum_{k=1}^{M} [x(k) - \mu_x]^2 \tag{3.4}$$

where μ_x is the mean of $x(k)$. The Doppler spectrum in decibels can be calculated from $x(k) = 10 \log 10(S(k))$. Note that σ_s is different from the spectrum width. σ_s

is obtained by assuming that $x(k)$ is a set of independent random value while σ_v is estimated by considering the spectrum as a PDF. An example of tornado spectrum from a real tornado case on 10 May 2003 is shown in Fig. 3.1. The spectrum in the left panel is from a gate associated with a tornado, and the spectrum in the right panel is from a gate 2 km away from the tornado. Note that the tornado is 38.5 km away from the radar.

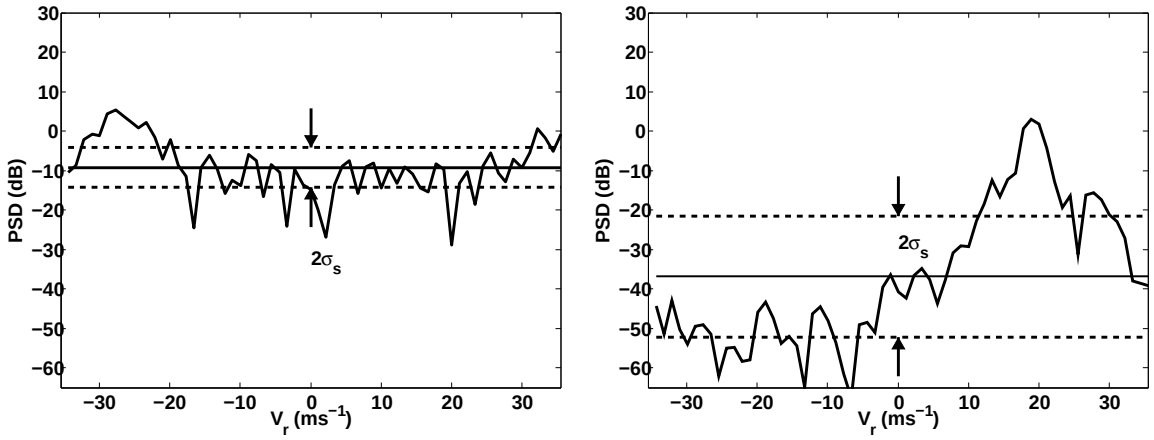

Figure 3.1: Characterization of TSS using the spectrum flatness. A tornado spectrum with signature of white spectrum is associated with a small value of σ_s as shown on the left panel, while a conventional Gaussian spectrum (2 km away from the tornado) exhibits high σ_s.

It is clear that σ_s is primarily determined by the statistical fluctuations for the case of flattened tornado spectrum. On the contrary, large σ_s is obtained by most contribution from the variation of the Gaussian shape itself for non-tornado cases. It should be pointed out that if the tornado is weak or the range to the tornado is short such that the tornado spectrum is no longer flat, σ_s will not help with the identification of a tornado vortex. Moreover, although in general a spectrum with large spectrum width will produce low σ_s, there are cases where σ_s can provide additional information to the spectrum width for the characterization of tornado spectra. Detailed statistical comparisons and the discussions of the limitation of σ_s are provided in section 3.1.2.

3.1.1.3 Higher-order spectral analysis

In this work, the third-order spectrum (bispectrum) analysis is proposed to quantify the tornado spectral signature by treating Doppler spectrum as 1D image. Bispectrum has been applied successfully to one-dimensional and two-dimensional pattern recognition (e.g., Chandran and Elgar 1993; Chandran et al. 1997). Let us first consider the Doppler spectrum of weather signals in decibels, $x(k)$, as the 1D image. The power spectrum of $x(k)$ is given by $S_x(f) = X(f)X^*(f)$, and the bispectrum is obtained using the following equation (Nikias and Raghuveer 1987):

$$B(f_1, f_2) = X(f_1)X(f_2)X^*(f_1 + f_2) \tag{3.5}$$

Where $X(f)$ is the N-point discrete Fourier transform of $x(k)$ (using an FFT routine). The bispectrum can be determined unambiguously within the region of $0 < f_2 < f_1 < f_1 + f_2 < 1$, where f_1 and f_2 are the normalized frequencies. Oppenheim and Lim (1981) have shown that the shape information is often contained in the phases of the Fourier transform of the pattern or image. This conclusion can be demonstrated using a "face off" example as shown in Fig. 3.2. In this example, the original image of "Lena" and "Johnny" are shown on the top of Fig. 3.2. A new image is created by the IFFT of a synthesized signal with the phase of "Lena" and magnitude of "Johnny" in the FFT domain. The result is shown on the bottom panel of Fig. 3.2. It is clear that the image of "Lena" can be somewhat recognized since the phase of the synthesized signal is from "Lena". Although the magnitude of the new image is from "Johnny", Johnny's picture can not be seen in the new image.

The application of bispectrum to identify TSS is motived by the following facts: (1) bispectrum can retain both the phase and amplitude of the Fourier coefficients, while the commonly used power spectrum suppresses the phases due to the multiplication of Fourier coefficients with their complex conjugates; (2) bispectrum is invariant to the shift of the pattern because the resultant phase shift in $X(f)$ is canceled in the triple product; (3) the bispectrum is also insensitive to additive Gaussian noise

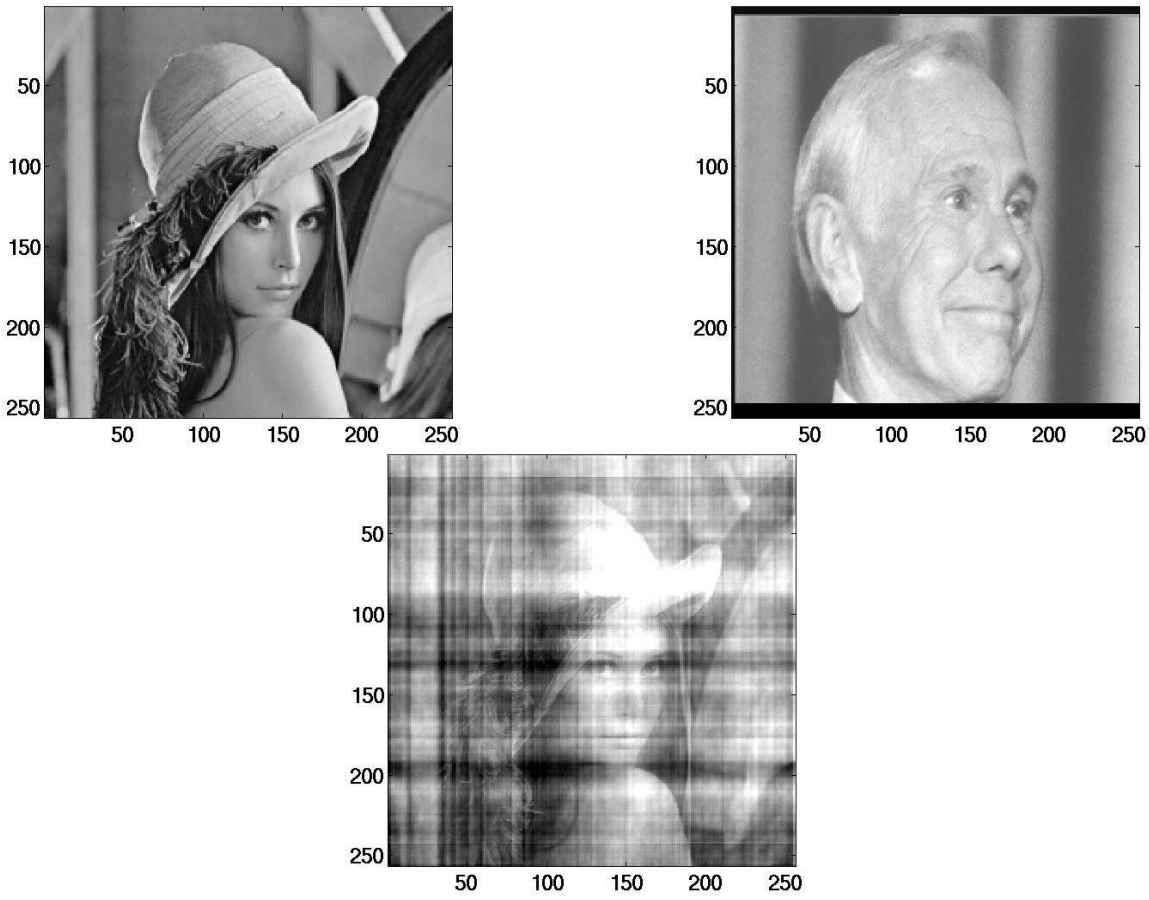

Figure 3.2: Original image of "Lena" (top left), original image of "Johnny" (top right). the synthesis image from the phase of "Lena" and the magnitude of "Johnny".

because theoretically the third-moment sequence of a stationary Gaussian process is zero (Papoulis and Pillai 2002) and the bispectrum is defined as its Fourier transform. (4) it also has been shown that bispectrum is useful in the identification of nonlinearity and non-Gaussian of the process (e.g., Nikias and Raghuveer 1987).

The bispectrum of a 1D image is a 2D complex function and is difficult to use directly for automated pattern recognition. Therefore, different integration methods have been proposed to extract the shape information. Axially integrated bispectrum (AIB) is one of the integrated bispectrum approach developed by Tugnait (1994). In this approach, the bispectrum is integrated along paths parallel to the f_1 or f_2 axes in bifrequency plane, therefore this method is called axially integrated bispectrum. The AIB is translation and scale invariant but will lose a great part of phase information (Zhang et al. 2001b). Circularly integrated bispectra (CIB) is another approach proposed by Liao and Bao (1998). A set of concentric circles with the origin as the center are the integrated paths. Although CIB is translation invariant and keeps the phase information of the signal, more computations are required. For the purpose of extracting spectra shape information, another integration method: radially integrated bispectra (RIB) is used in this work. In particular, the RIB is obtained along a radial line of slope a (Chandran and Elgar 1993). The integration path is presented in Fig. 3.3. The phase of RIB (PRIB), abbreviated by P, is proposed to effectively extract the shape information from a bispectrum, and is defined in the following forms (e.g., Chandran and Elgar 1993; Shao and Celenk 2001; Zhang et al. 2001b):

$$P(a) = \tan^{-1}\left[\frac{I_i(a)}{I_r(a)}\right] \tag{3.6}$$

where

$$I(a) = I_r(a) + jI_i(a) = \int_{0^+}^{\frac{1}{1+a}} B(f_1, af_1)df_1, \tag{3.7}$$

where I is the integration of bispectrum along the path of $f_2 = af_1$ in the bispectrum domain, $0 < a \leq 1$ is the slope of the path, and PRIB is the phase of the complex

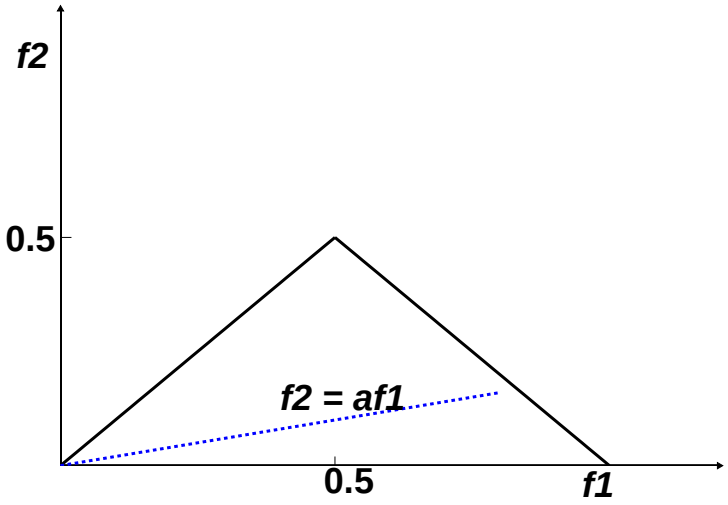

Figure 3.3: Region of computation of the bispectrum. Features are obtained integrating the complex bispectrum along a radial line with slope $= a$ (dashed line). $PRIB$ is the phase of the integrated bispectrum, which shows translation and scale invariance.

variable I. The integral of Eq. (3.7) is approximated by a sum, yielding in the following approach (Chandran and Elgar 1993).

$$I(a) = \sum_{k_1=1}^{\lfloor (M/2-1)/(1+a) \rfloor} B(k_1, ak_1) \tag{3.8}$$

where the $B(k_1, ak_1)$ is interpolated by:

$$B(k_1, ak_1) = pB(k_1, \lceil ak_1 \rceil) + (1-p)B(k_1, \lfloor ak_1 \rfloor) \tag{3.9}$$

and $p = ak_1 - \lfloor ak_1 \rfloor$, $\lfloor x \rfloor$ represents the largest integer contained in x, and $\lceil x \rceil$ represents the smallest integer containing x. The invariant parameter $P(a)$ is the principal component of the phase of $I(a)$, $-\pi < P(a) \leq +\pi$. Compared to AIB and CIB, PRIB shows few advantages. First of all, the PRIB is also translation and scale invariant and keeps the phase information of the signal. Second, PRIB is computationally efficiently (Zhang et al. 2001b). Third, PRIB has been successfully implemented in one (Chandran and Elgar 1993) and two dimensional (Chandran et al. 1997) pattern recognition. It is shown in Chandran and Elgar (1993) that

the phase of the Fourier transform of asymmetric pattern is a nonlinear function of frequency, and PRIB can isolate this nonlinearity to provide information about the shape. In addition, it has been proven that PRIB is invariant to amplification, scaling, and DC shifting of the input signals. The translation or shift invariant has a great advantage in our application because spectra with different mean Doppler velocities will produce the same value of PRIB. It should be noted that P does not provide any shape information if the input sequence has even or odd symmetry, because the resultant bispectrum is either real or purely imaginary, respectively. An alternative approach was developed by Chandran and Elgar (1993) to alleviate this problem. A new sequence is first generated that is the amplitude of the Fourier transform of the original signal $x(k)$ (i.e., $|X(f)|$). Consequently, the bispectrum is calculated using only the first half of the new sequence such that an asymmetry pattern is obtained. This approach can still maintain those invariant properties (Chandran and Elgar 1993; Shao and Celenk 2001).

The application of PRIB to the characterization of TSS is demonstrated in Fig. 3.4. The PRIB of a Gaussian and rectangular pattern as a function of spectrum width is shown for $a = 0.9$. These two patterns have the same spectrum width, which varies from 1 to 28 m s^{-1}. An example of Gaussian and rectangular pulse with the same spectrum width of 20 m s^{-1} is shown in the left panel. Distinct P values can be identified over the entire spectrum widths from these two patterns. This example suggests that the PRIB can be used to differentiate the two patterns for a wide range of spectrum widths, even though the two patterns have the same spectrum width.

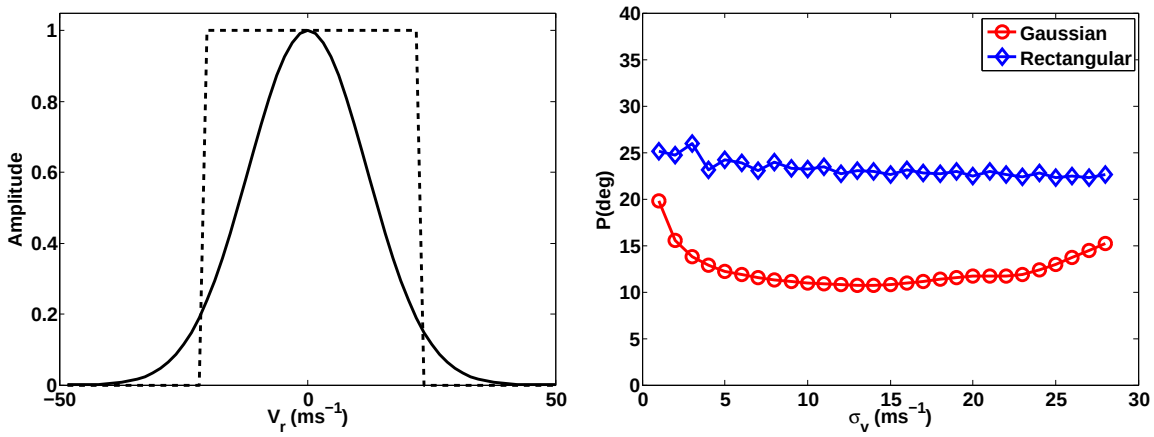

Figure 3.4: An example of a rectangular pulse and a Gaussian pulse (left). Both of them have spectrum width of $\sigma_v = 12$ m s $^{-1}$. The P value of rectangular pulse and Gaussian pulse (right) as a function of σ_v.

3.1.1.4 Eigen-ratio

In Yeary et al. (2007), it is shown that a white-noise like spectrum can be reflected on the distribution of eigenvalues of the correlation matrix. Let $V(n)$ be defined as $I\&Q$ data collected by research WSR-88D, in the following vector form.

$$U(n) = [V(n), V(n-1), ..., V(n-M+1)]^T \tag{3.10}$$

where M denotes the number of samples. The autocorrelation function of a WSS discrete-time process is defined to be: $R(l) = E[V(n)V^*(n-l)]$ for $l = 0, \pm 1, \pm 2, ...,$ etc. Consequently, the autocorrelation matrix, $\mathbf{R}$, of this discrete-time process is defined as:

$$\mathbf{R} = \begin{bmatrix} R(0) & R(1) & \cdots & R(M-1) \\ R^*(1) & R(0) & \cdots & R(M-2) \\ \cdots & \cdots & \cdots & \cdots \\ R^*(M-1) & R^*(M-2) & \cdots & R(0) \end{bmatrix}. \tag{3.11}$$

The correlation of a stationary discrete-time process is Hermitian and also Toeplitz. It is always nonnegative definite and almost always positive definite (Monson 1996).

This is important for proving the eigenvalues of $\mathbf{R}$, that describe $U(n)$, are positive and non-zero. Let λ_i and q_i denote the ith eigenvalue and eigenvector of $\mathbf{R}$, respectively.

$$\mathbf{R}q_i = \lambda_i q_i \quad i = 1, 2, ..., M \tag{3.12}$$

In order to get the eigenvalues of matrix $\mathbf{R}$, multiplying both sides of Eq. (3.12) by q_i^H gives: $q_i^H \mathbf{R} q_i = q_i^H \lambda_i q_i = \lambda_i q_i^H q_i$, for $i = 1, 2, ..., M$. Hence,

$$\lambda_i = \frac{q_i^H \mathbf{R} q_i}{q_i^H q_i} \quad i = 1, 2, ..., M \tag{3.13}$$

where $q_i^H q_i$ is the square Euclidean length of the eigenvector q_i and is always positive definite. Then we can conclude $\lambda_i > 0$ for $i = 1, 2, ..., M$. Moreover

$$\lambda_1 \geq \lambda_2 \geq ... \geq \lambda_i \geq ... \geq \lambda_M \geq 0 \tag{3.14}$$

It has also been shown that eigenvalues λ_i are bounded by the maximum and minimum values of the power spectrum of $V(n)$:

$$\min S_x(f) \geq \lambda_i \geq \max S_x(f) \tag{3.15}$$

where $S_x(f)$ is the power spectrum of the input sequence $V(n)$. In our analysis of tornadic time series data, we considered the ratio of the smallest over the largest eigenvalue for correlation matrix of time series data calculated for only five time lags: $\chi(R) = \lambda_M / \lambda_1$. It follows from Eq. 3.14 and Eq. 3.15 that:

$$0 < \chi(R) = \frac{\lambda_M}{\lambda_1} \leq \frac{\min S_{xx}(\omega)}{\max S_{xx}(\omega)} \leq 1 \tag{3.16}$$

Thus, $\chi(R)$ approaches identity (or unity) as the power spectrum becomes increasingly flat.

3.1.2 Analysis of tornado spectral signatures using numerical simulations

The shape of tornado spectra depends on several parameters such as the tornado's size relative to the resolution volume, its location within the radar volume, and the reflectivity structure. Four parameters of spectrum width, spectral flatness, PRIB and Eigen-ratio are proposed to characterize TSS. The dependence of these four parameters on range and relative location within the radar volume is studied statistically in this section using numerical simulation developed in chapter 2.

The radar resolution volume is located due north from the radar and its position is denoted by (r_0, ϕ_o) where $\phi_o = 0^o$. A tornado within a mesocyclone as shown in Fig. 2.3 is centered at ($r_0^{'}$, $\phi_o^{'}$). To study radar sampling of different portions of the tornado, 121 tornado locations within the radar resolution volume are simulated, where $r_0^{'}$ varies from $r_0 - 125$ m to $r_0 + 125$ every 25 m and $\phi_o^{'}$ varies from -0.5^o to 0.5^o at 0.1^o intervals. In this work, the maximum unambiguous velocity, effective beamwidth and range resolution are 35 m s^{-1}, 1.39 ^{o} and 250 m, respectively. A tornado with radius of 200 m is located on the southeast of a mesocyclone whose radius is 2 km. The center of the tornado and mesocyclone are separated by 1 km. The maximum tangential velocity for the tornado and mesocyclone is 50 and 15 m s^{-1}, respectively, and a maximum radial velocity of 5 m s^{-1} is used for both vortices. The details of simulation are provided in Section 2.2. It is obvious that in this work, the maximum wind in tornado exceeds the maximum unambiguous velocity of 35 m s^{-1}. Spectra from both uniform reflectivity and doughnut-shaped reflectivity (W_z = 60 m) are simulated and are defined as T_U and T_D, respectively. An example of spectra from 36 resolution volumes is shown in Fig. 3.5 for r_0 = 60 km and SNR = 40 dB.

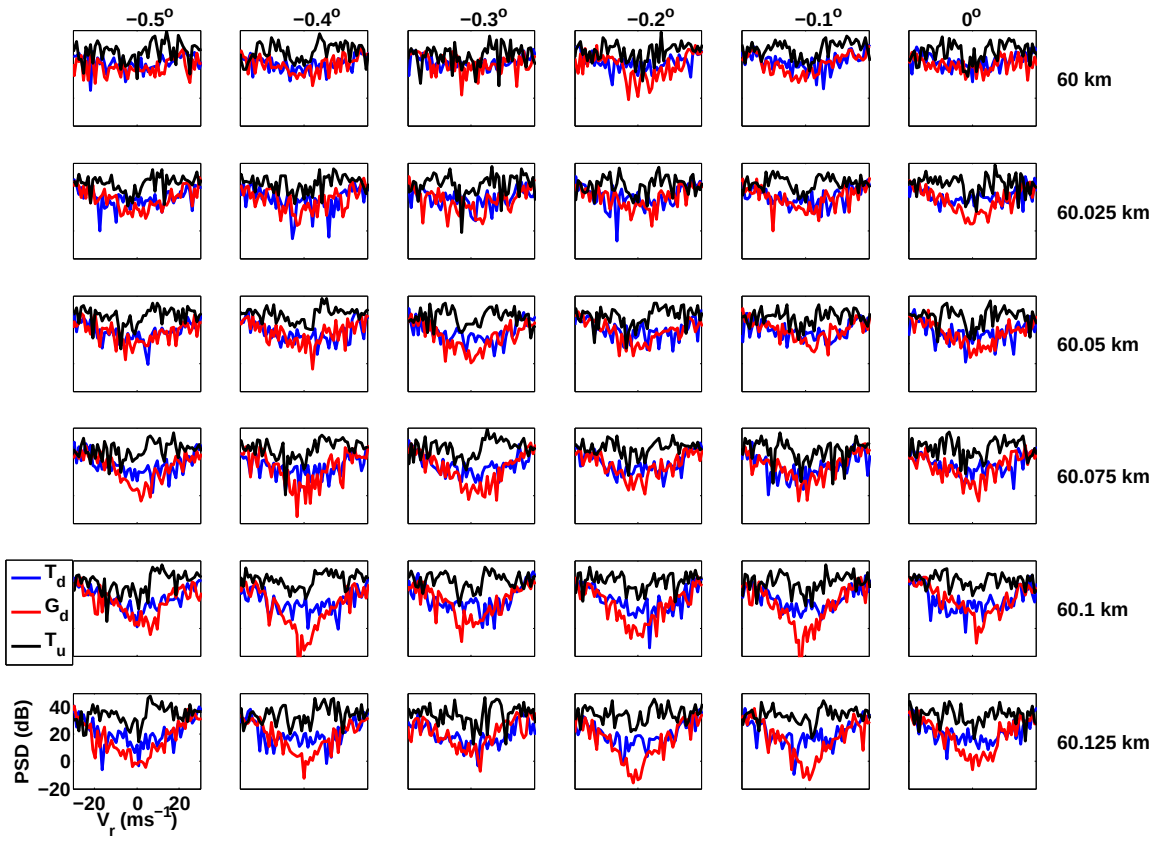

Figure 3.5: Simulated spectra for different portions of the tornado sampled by the radar. The radar resolution volume is centered at ($r_0 = 60$ km, $\phi_o = 0^o$). The tornadic vortex center is located at $\phi_o^{'}$ = -0.5^o, -0.4^o, -0.3^o, -0.2^o, -0.1^o, 0^o from the left to the right columns, and of $r_0^{'}$ = 60.125 km, 60.1 km, 60.075 km, 60.05 km, 60.025 km and 60 km from the bottom to the top rows,respectively. Spectra from doughnut-shaped reflectivity (T_D), uniform reflectivity (T_U), and reconstructed Gaussian spectra G_D are denoted by blue, black, and red lines, respectively.

In order to demonstrate that TSS can provide shape information in addition to spectrum width, Gaussian spectra with the same spectrum widths (termed as G_D and G_U) are reconstructed using following equations:

$$G_D(v) = \frac{S}{\sqrt{2\pi}\sigma_v}\exp(\frac{-(v-\bar{v}_r)^2}{2\sigma_v^2}) + \frac{S}{\sqrt{2\pi}\sigma_v}\exp(\frac{-(v-\bar{v}_r \pm 2V_a)^2}{2\sigma_v^2}) \qquad (3.17)$$

The simulation velocity range $v = [-V_a\ V_a]$ with the step $\delta v = 2V_a/\mathrm{N}$. S, $\bar{v}_r$ and σ_v^2 are the zero, first and the second moments estimated from the simulated tornado spectra. The second term on the right hand side of (3.17) is from the velocity aliasing, where $V_a = 35$ m s $^{-1}$ is the maximum ambiguous velocity. Slight difference in spectral shape can be observed if the tornado center locates at various places inside the radar sample volumes in both azimuth and range directions. Since the spectrum for G_U is similar to T_U, therefore it is not shown for clarity. The tornado spectrum from doughnut reflectivity (T_D) becomes flatter when the vortex center is closer to radar resolution volume center in azimuthal direction and farther in range direction. In general, most spectra from uniform reflectivity (T_U) is flatter than those from T_D. Since most weather signals exhibit Gaussian-shaped spectra (Janssen and Spek 1985), the reconstructed Gaussian spectra can be considered as the spectra from nontornadic regions with large spectrum widths. It is evident that the reconstructed Gaussian shaped spectra can not fully characterize the tornado spectra, which can be exemplified in the panel of $\phi_o^{'}$ = -0.2^o and $r_0^{'}$ = 60.125 km. Therefore, it is important to demonstrate that the spectral flatness, PRIB and eigen ratio can provide additional information in identifying tornado spectra from nontornadic spectra. In section 2.2, the variation of a Doppler spectrum as a function of range has been examined. Additionally, the strength of tornado vortex signature (TVS) in the velocity field has been shown to deteriorate with range due to the increasing size of radar resolution volume (Brown et al. 1978, 2002). The extreme Doppler velocity values of opposite sign is defined as tornado signature (TS) if the tornado's core diameter is larger than the radar's effective beamwidth or defined as tornadic vortex signature (TVS) otherwise.

Thus, the impact of range on the four TSS parameters of spectrum width, spectral flatness, PRIB and eigen ratio are now studied using numerical simulations. The same configuration of tornado and mesocyclone as shown in Fig. 3.5 is performed at various ranges. The normalized distance between the tornado and the radar is defined as $r_n = r_0^{'}\theta_b/r_t$, where $r_t = 200$ m and effective beamwidth $\theta_b = 1.39^0\pi/180$ (rad). The normalized distance varies from 0.12 to 18.1951, which corresponds the real distance from 1 km to 150 km. Results of spectrum width, spectral flatness, PRIB and eigen ratio are shown in Figs. 3.6, 3.7, 3.8 and 3.9, respectively. In order to make the figures large enough to be recognized, only the results from range of r_0, r_0-50m, and r_0-100m and $\phi_o^{'}$ of 0^o, 0.2^o and 0.4^o are shown.

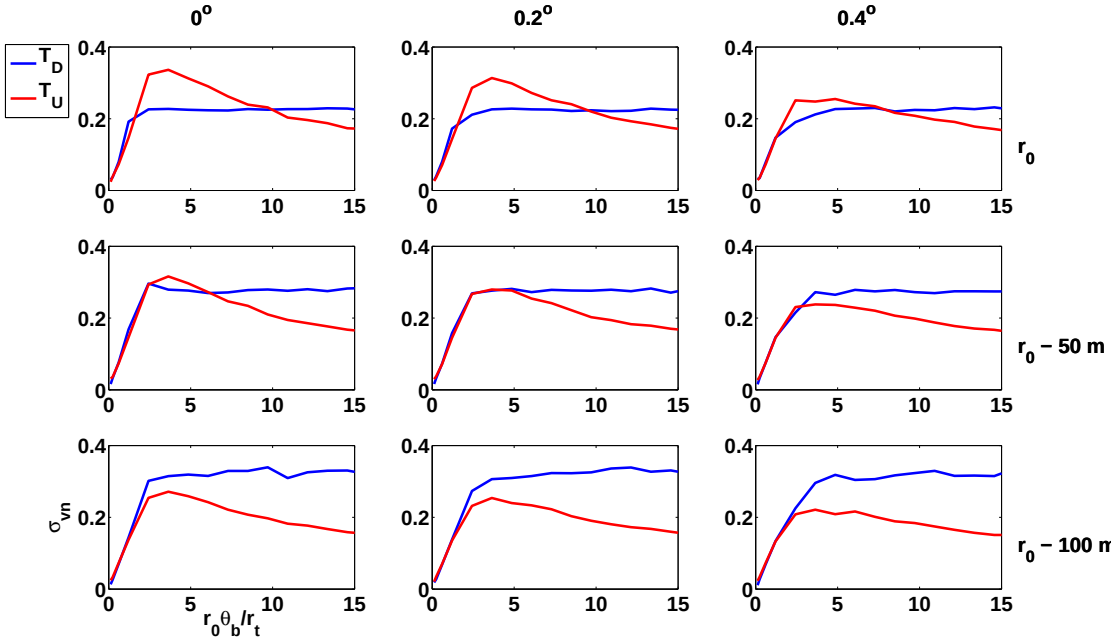

Figure 3.6: The variation of the normalized spectrum withs (σ_{vn}) as a function of normalized range. Spectrum widths estimated from the spectra generated using doughnut (T_D) and uniform (T_U) reflectivities. It is apparent that with the increase of the normalized range, the σ_{vn} increase, and can keep relative large value even at far normalized range.

The normalized spectrum width of $\sigma_{vn} = \sigma_v / 2V_a$ is presented in Fig. 3.6 as a function of normalized range. For both doughnut reflectivity T_D and uniform reflectivity T_U, the σ_{vn} increases rapidly with range for $r_n < 5$. After $r_n > 5$, T_U decreases with range while T_D is maintained at almost a constant value with range. It also indicates that at a given r_n the spectrum width from uniform reflectivity decrease if the tornado center is shifted farther from the radar resolution volume center in azimuth or range direction. When $r_0^{'} = r_0$, spectrum widths from uniform reflectivity (T_U) are larger than than those from doughnut-shaped reflectivity (T_U) at relative close range ($r_n < 10$) but become smaller at far range. However, the spectrum width from T_D is larger than from T_U when a relative small portion of the tornado is sampled. (e.g. $\phi_o^{'}$ = 0^o, and $r_0^{'}$ = -100 m, $\phi_o^{'}$ = 0.2^o, and $r_0^{'}$ = -100 m). The larger spectrum widths can result from velocity aliasing of a relatively flat spectra and suggest that additional parameters are needed to characterize TSS. The spectral shape as a function of range has been shown in section 2.2.2.2.

The variation of spectral flatness in range is presented in Fig. 3.7. The reconstructed Gaussian spectra using Eq. (3.17) from doughnut and uniform reflectivity are included for comparison. In general, tornado spectra show better spectral flatness (lower value) than the reconstructed Gaussian spectra for both reflectivity structures. Moreover, both the tornado and reconstructed Gaussian spectra from uniform reflectivity show lower spectra flatness than from doughnut shape reflectivity. When the tornadic center is far away from the radar resolution center, the spectral flatness difference between the doughnut shape and uniform reflectivity structure becomes smaller. Similar trend can also be observed between the tornado spectra and reconstructed Gaussian spectra. Statistical results of PRIB and eigen ratio are shown in Fig. 3.8 and 3.9. It is evident that these two variables have distinct values for tornado and non-tornado cases at various ranges, which can be used for tornado detection. Apparent increase with range for $0 < r_n < 5$ and relatively smooth decrease after

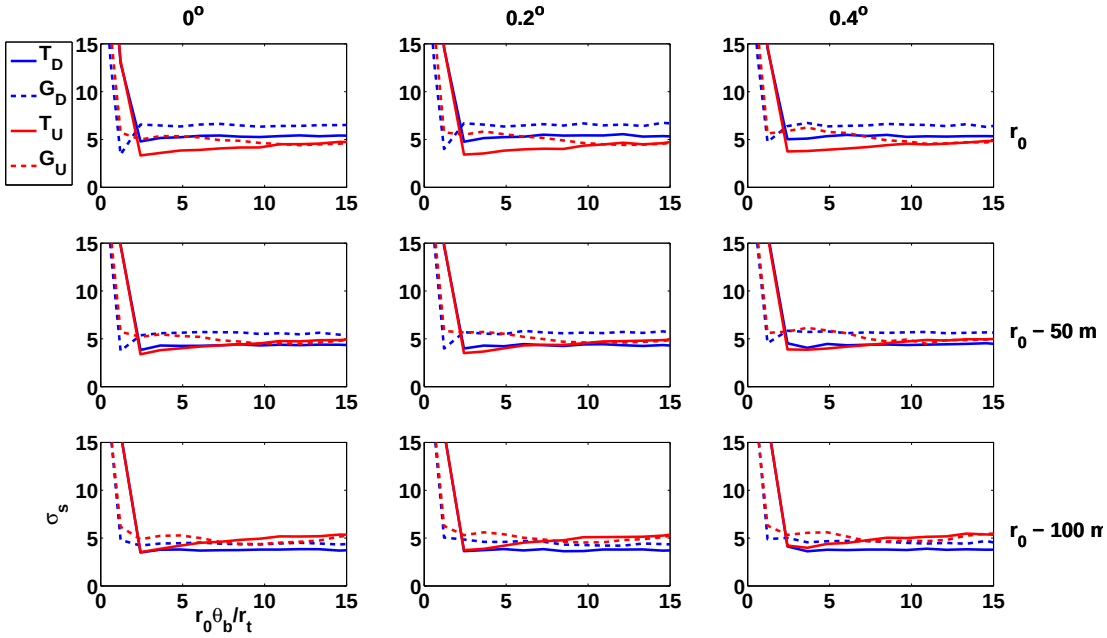

Figure 3.7: Similar to Fig. 3.6, but for the spectral flatness (σ_s). In addition, results from the reconstructed Gaussian spectra (G_D and G_U) are included for comparison.

$r_n > 5$ can be observed for both of them, which are consistent with the spectrum width. The tornado spectra from uniform reflectivity show larger P and χ_R for all ranges than those from donut shape reflectivity structure. This indicates the tornado spectra from uniform reflectivity have more "flat" and "wide" tornado spectral signatures, which is consistent with the results described in section 2.2.2

These results suggest that unlike tornado shear signature, the three parameters for tornado spectra are less sensitive to the increasing size of the radar volume except at close range. Among these four parameters (σ_v, σ_s, P and χ_R), it has been shown in Fig. 3.5 that spectrum width is not sufficient to distinguish the tornado spectrum from the reconstructed Gaussian spectrum even though the spectrum shape is different. On the other hand, Fig. 3.7, 3.8 and 3.9 show that σ_s, P and χ_R derived from tornado spectra for the case of doughnut reflectivity (T_D) are different from those from the reconstructed Gaussian spectra (G_D) for $r_n > 1$. Although such a difference becomes

small when the radar resolution volume is located farther from the tornado's center in range, high P and χ_R and small σ_s are still observed. For the case of uniform reflectivity, it is evident that P, σ_S and χ_R can assist with the identification of tornado spectrum since all these values from tornado spectra show apparent difference from reconstructed spectra. On the other hand, a false detection can occur if only the spectrum width is used and the spectra from nontornadic regions have large spectrum width. Moreover, spectrum width estimate can be significantly biased at large spectrum widths and should be used with caution.

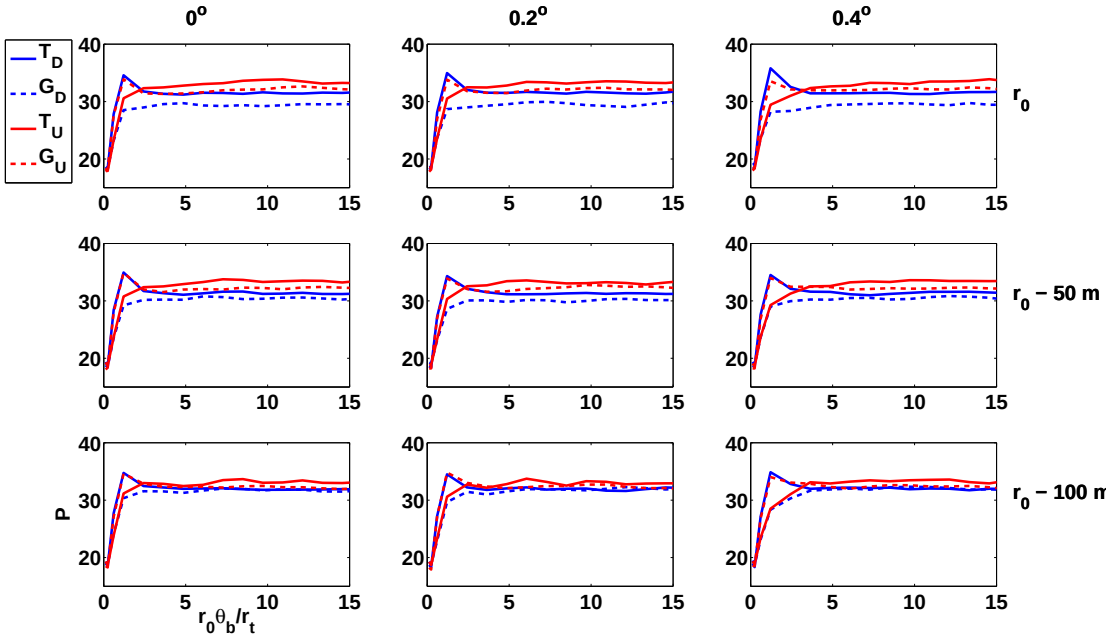

Figure 3.8: Similar to Fig. 3.7, but for PRIB P.

3.1.3 Analysis of tornado spectral signatures using radar observations

Two tornado outbreaks in central Oklahoma on 8 May and 10 May 2003 are of interest. Level I time series data were collected by the research WSR-88D (KOUN) operated by the NSSL in Norman, Oklahoma during the two tornado events. A more

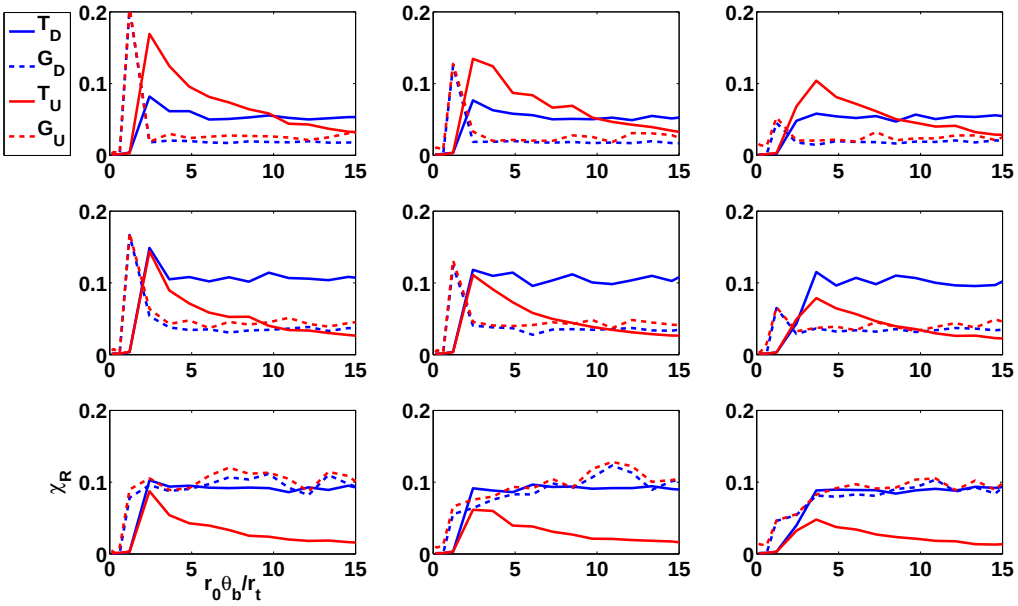

Figure 3.9: Similar to Fig. 3.7, but for eigen ratio χ_R.

detailed description of the two events is provided in next chapter. Doppler spectra were estimated by the periodogram method with 64 samples, which corresponds to the standard 1 ^{o} angular sampling. A von Hann window was used to produce a large dynamic range in the Doppler spectrum (Doviak and Zrnić 1993). The three spectral moments (reflectivity, Doppler velocity and spectrum width) were estimated using covariance method, and the three feature parameters of spectral flatness, PRIB and eigen ratio used to quantify the TSS were estimated using the method described in section 3.1.1. The reflectivity, mean Doppler velocity and spectrum width from the lowest elevation angles of 0.5 ^{o} at 0343 UTC are shown on the top of Fig. 3.10 from left to right, respectively. The bottom three panels from left to right are spectral flatness, PRIB and eigen ratio. Data associated with SNR smaller than 20 dB are not shown for clarity. In order to help identifying tornado location, tornado damage path from ground survey is superimposed using transparent blue shading area.

The region of hook echo signature, highlighted by a white box, is consistent with the tornado damage path and is well correlated with the region of strong azimuthal shear. Enhanced spectrum width, PRIB and eigen ratio as well as reduced spectral flatness can be observed in the region within the white box. Velocity aliasing can be observed at approximately 5 km northeast of the tornado region, and is denoted by a black box. False tornado detection is likely produced by current tornado vortex detection algorithm (TDA) if the velocity field is improperly dealiased. However, the spectrum width, PRIB, spectral flatness and eigen ratio exhibit values different from those in tornadic region denoted by the white box. In other words, these four TSS parameters are useful for accurate tornado detection.

Doppler spectra from the tornado region (white box) and velocity aliasing region (black box) are shown on the top and bottom of Fig. 3.11. The mean radial velocity is indicated by green downward and red triangles to represent negative and positive velocity, respectively. Artificial shear signature caused by velocity aliasing can be observed at gates (9.052^o, 43.875 km to 44.375 km) and (8.094^o, 43.375 km to 44.625 km) on the top of Fig. 3.11, which can lead to false detection in shear-based TDA if dealiasing is not performed correctly. However the spectra from those gates do not exhibit wide and flat tornado spectral signatures, they can be easily identified as nontornado if the information of spectral signature is used. Large velocity difference can also be observed at the gate (8.094^o to 9.052^o, 39.125 km to 39.625 km) on the bottom of Fig. 3.11. Additionally, wide and flat spectra in terms of enhanced σ_v, P and χ_R and low σ_s can be observed at those gates.

Another interesting example at 0349 UTC is presented in Fig. 3.12. Similar to Fig. 3.11, the tornado damage path, hook signature and azimuthal shear can help identify the tornado location. The region close to the tornado and a region located at 5 km away from tornado are indicated by white and black boxes, respectively. Within the tornado region (within the white box), hook signature, large azimuth

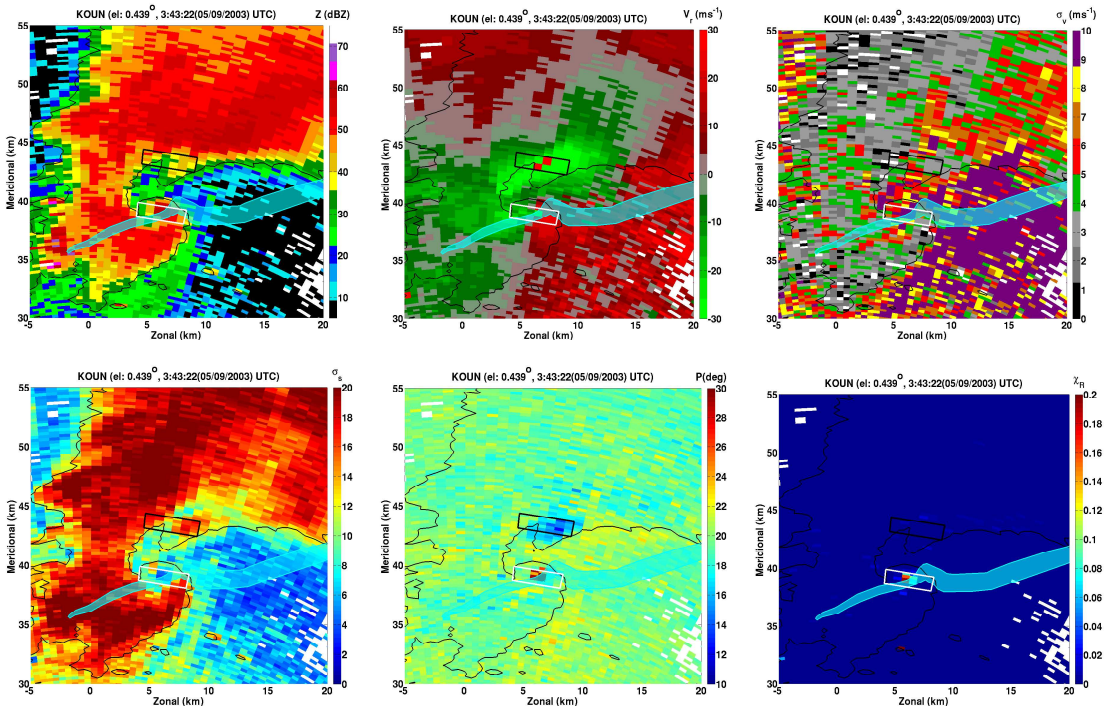

Figure 3.10: The reflectivity(top left), mean Doppler radial velocity(top middle), spectrum width(top right), spectra flatness(bottom left), PRIB(bottom middle), and eigen ratio(bottom right) at 0343 UTC. The tornado damage path is superimposed as a light shaded area. A contour of reflectivity with 30 dBZ is indicated by black lines in all the panels. Apparent large P, σ_v, χ_R and low σ_s can be observed within the white box at the tornado location.

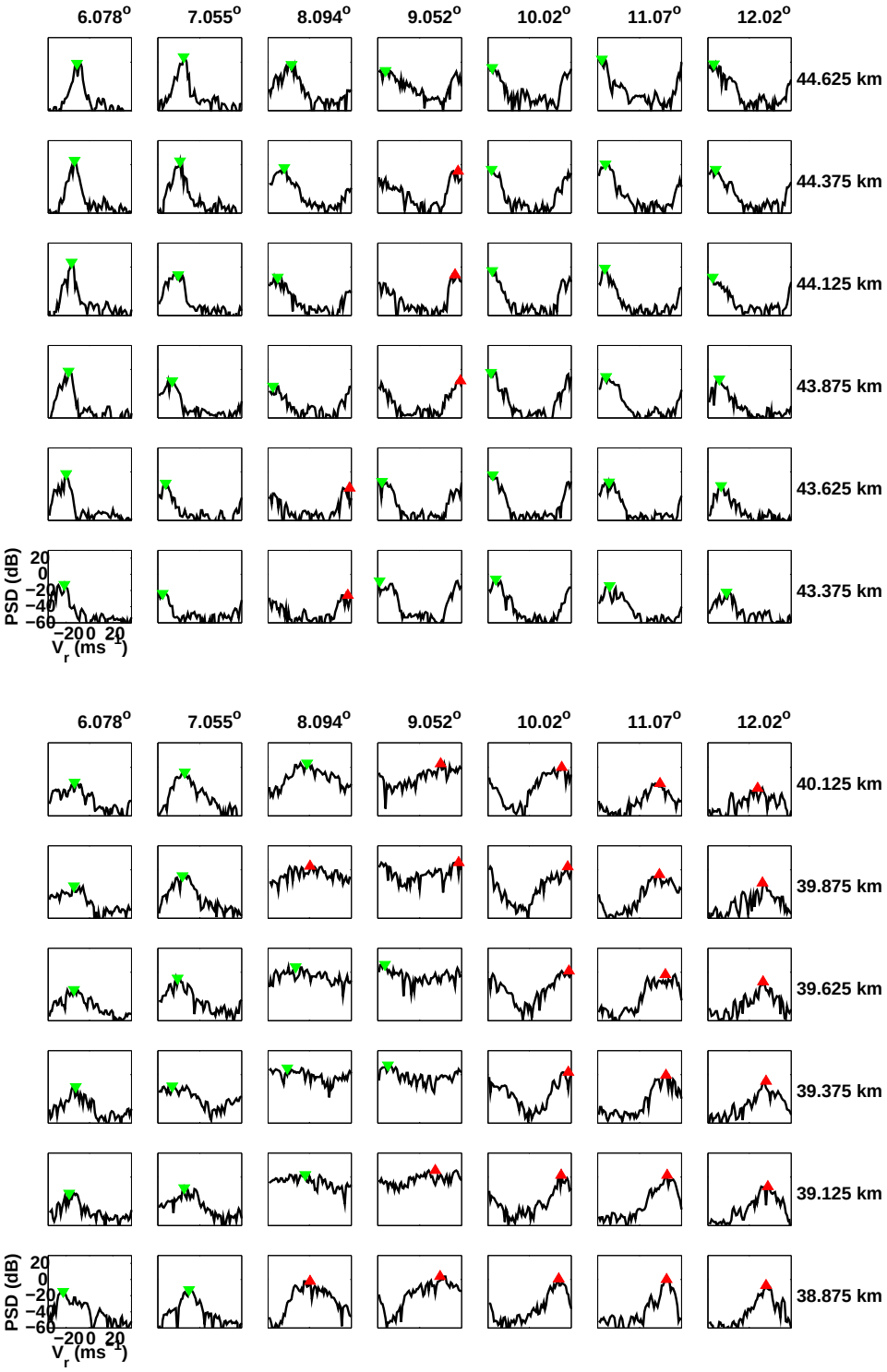

Figure 3.11: The spectra within the black box (region of velocity aliasing) and white box (tornado region) in Fig. 3.10 are presented on the top and bottom panels, respectively.

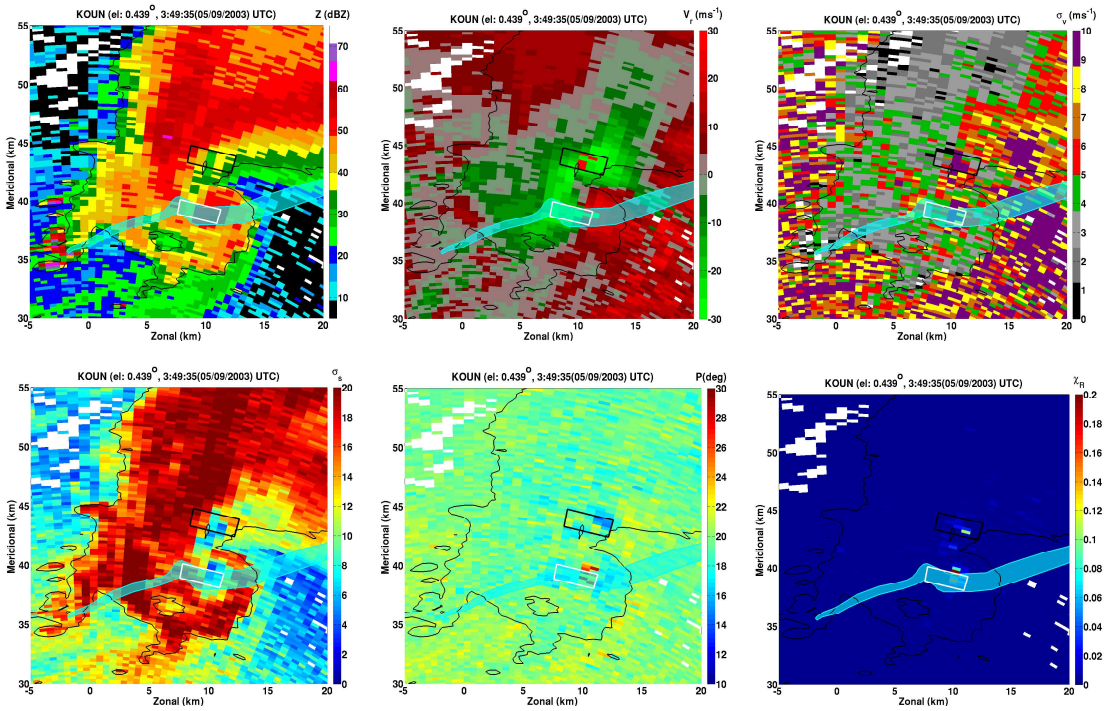

Figure 3.12: The reflectivity (top left), mean Doppler radial velocity (top middle), spectrum width (top right), spectra flatness (σ_s) (center left), PRIB P (center middle), and eigen ratio (χ_R) (center right) at 0349 UTC. The tornado damage path is superimposed as a light shaded area. A contour of reflectivity with 30 dBZ is indicated by black lines in all the panels.

shear as well as TSS are consistent with the tornado damage path. Similar velocity shear and enhanced spectrum width, which could be caused by the velocity aliasing can also be observed within the black box. Therefore, for this case, the conventional moment data of radial velocity and spectrum width are not sufficient to distinguish tornado spectra from nontornado spectra. However, the P and χ_R within the white box show apparently higher value than in the region within the black box, which can help tornado identification.

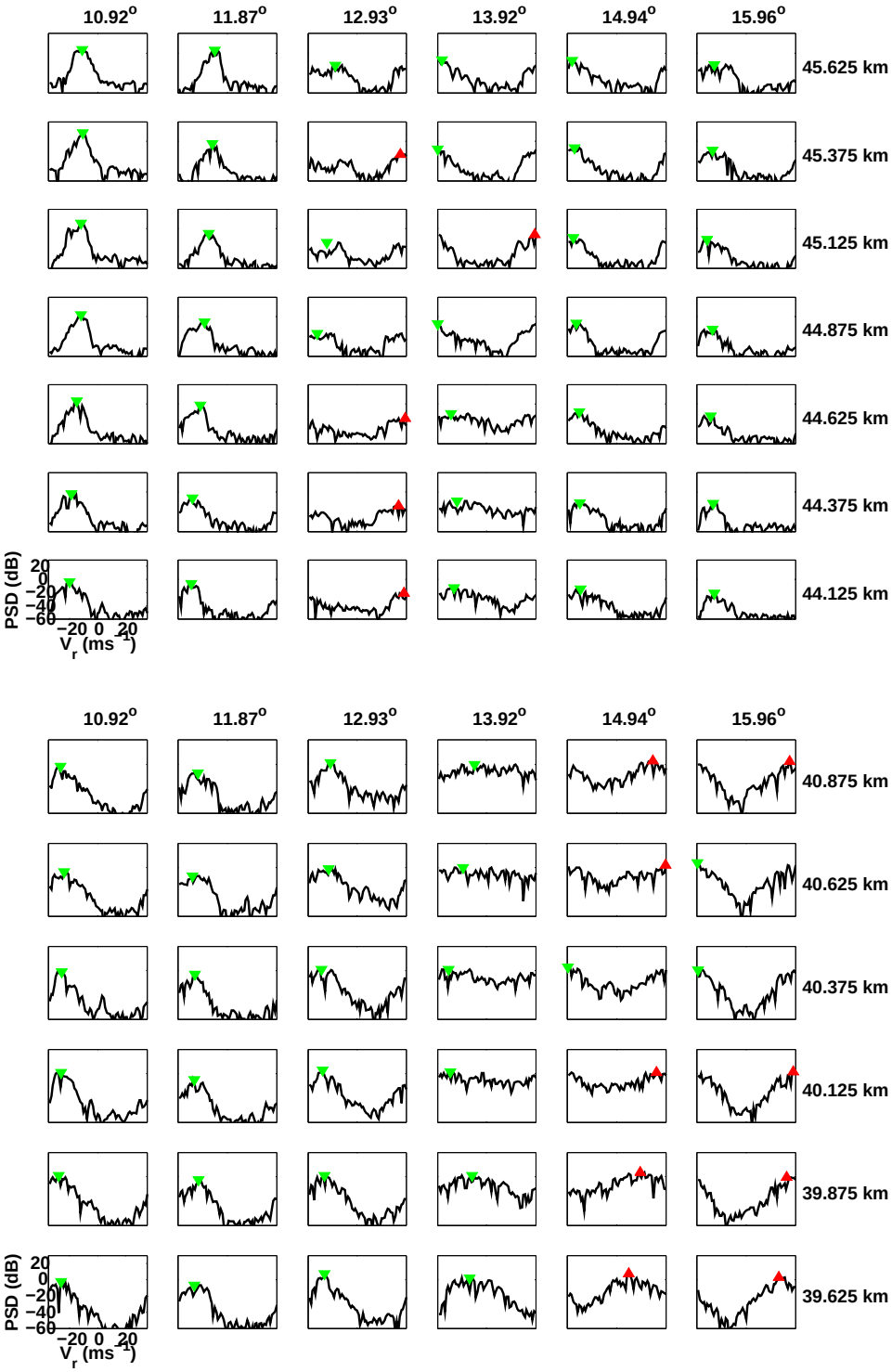

Figure 3.13: The spectra within the black box (region of velocity aliasing) and white box (tornado region) in Fig. 3.12 are presented on the top and bottom panels, respectively.

3.2 Tornado Debris Signatures

3.2.1 Tornado debris signature observation

The upgrade of WSR-88D to dual polarization is underway, and therefore incorporating polarimetric variables into NFTDA becomes more attractive. Polarimetric tornadic debris signatures, characterized by near-zero Z_{DR} and anomalously low values of ρ_{hv}, were first reported by Ryzhkov et al. (2002) based on the observation of a tornado event outbreak on 3 May 1999 in central Oklahoma. The TDS has been further demonstrated using two tornado events on May 2003 recorded with NSSL's KOUN (Ryzhkov et al. 2005). Randomly oriented scatterers with large size, irregular shapes and a low degree of common alignment are the reasons for tornadic debris signatures (Ryzhkov et al. 2005). Although it was reported that the TDS is visible for strong (above EF-3) tornadoes, tornadoes with EF-1 scale have been observed associated with these signatures (Kumjian and Ryzhkov 2008). Thus, the TDS has the potential to improve or facilitate tornado detection, especially when the velocity and/or the spectral signatures cannot provide sufficient discernibility, which will be discussed in next chapter.

In this dissertation, the analysis of TDS is performed using real data collected by the KOUN. Although the simulation used for TSS analysis is advantageous, such type of simulation cannot be easily extended for polarimetric signatures. One type of physical-based simulation has been discussed in Capsoni and D'Amico (1998) and Capsoni et al. (2001). In addition, the Z_{DR} arc signature has been simulated by Kumjian and Ryzhkov (2008). However, formulations related to the tornado debris's backscattering properties and motions are needed for this approach, which requires significant efforts on electric magnetic field and atmospheric dynamics. Therefore, in this work the analysis of TDS is focused on using real data.

3.2.2 Analysis of tornado debris signatures

In this work, the potential of TDS for tornado detection is demonstrated using one tornado case on 8 May 2007 which was recorded by the KOUN. According to the report from NWS Forecast Office in Norman OK, this tornado was formed at 0443 UTC and moved north through part of El Reno in central Oklahoma for approximately 7 minutes and traveled approximate 1.75 miles before it disappeared. The tornado is likely EF1 on the Enhanced Fujita scale. Details of this tornadic event can be referred at http://www.srh.noaa.gov/oun/wxevents/20070508/.

The fields of radial velocity, spectrum width, differential reflectivity, and correlation coefficient in the vicinity of the tornado are shown in Fig. 3.14. The tornado's starting and ending locations are indicated by two white asterisks. The white line connecting the two points provides a rough reference of the tornado damage path. From the radial velocity plot, apparent shear signature can be observed around (-46 km, 30 km) in the east-west (zonal) and north-south (meridional) directions. Enhanced σ_v, low Z_{DR} and ρ_{hv} can also be found at this location, which agree well with the tornado damage path. Within the 30 dBZ reflectivity contour, one more shear region can be found around (-37 km, 27 km). Since this region is approximately 10 km away from the tornado damage path, it is not likely caused by the tornado. In order to further investigate these two shear regions, V_r, σ_v, Z_{DR} and ρ_{hv} as a function of azimuthal angles for three consecutive ranges are shown in Fig. 3.15. Fig. 3.15 (a), velocity difference of above 20 ms $^{-1}$ can be found at 54.125 km in range and 304 ^{o} in azimuthal direction. σ_v of 7 ms $^{-1}$, Z_{DR} of 0.6 dB and ρ_{hv} of 0.75 can be observed as well. From the other two range gates, V_r, σ_v and ρ_{hv} show good consistency. All these indicate that the tornado is located at (54.125 km, 304^o) at this moment (0447 UTC). In Fig. 3.15 (b), large velocity difference of above 20 ms $^{-1}$ and enhanced spectrum width of above 6 ms $^{-1}$ can be found at 46.875 km and 309^o in range and azimuthal direction, respectively. The results from other two range gates also show

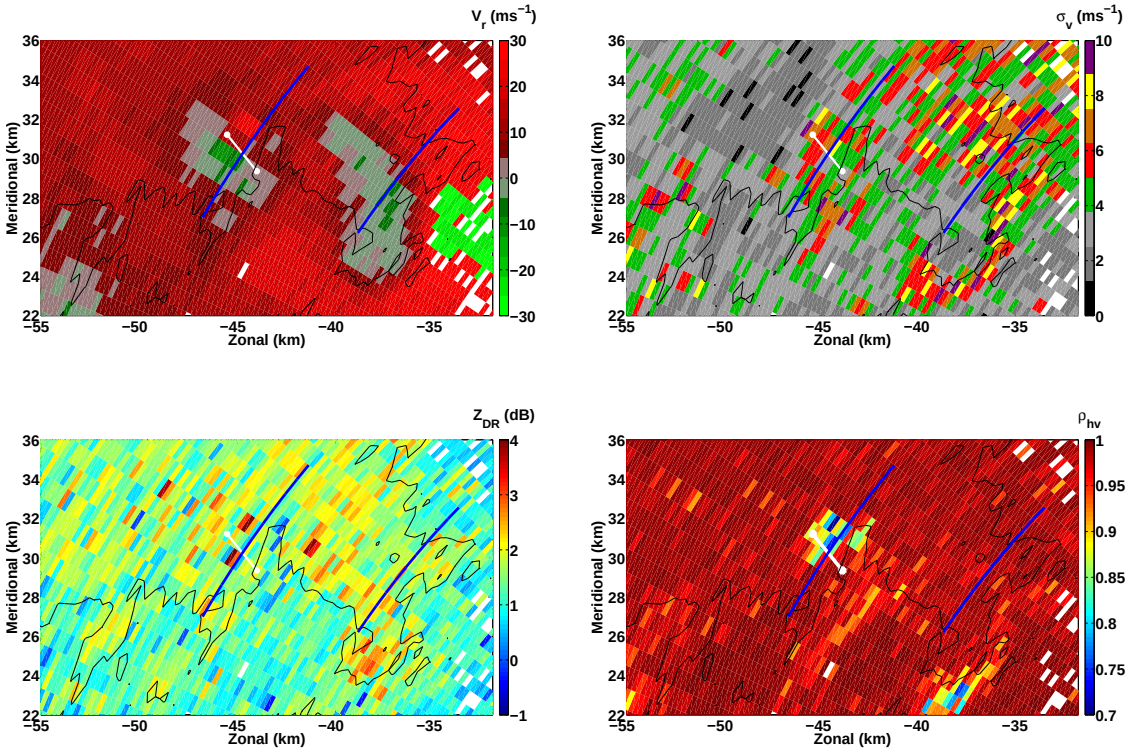

Figure 3.14: The Doppler velocity (V_r) (top left), spectrum width (σ_v) (top right), differential reflectivity (Z_{DR}) (bottom left), correlation coefficient ρ_{hv} (bottom right) from 0.5^o elevation angle at 0447 UTC 8 May 2007. The start and end locations of tornado damage path are indicated by two white stars and further connected by a white line. The V_r, σ_v, Z_{DR} and ρ_{hv} along azimuthal direction indicated by blue lines are shown in Fig. 3.15 A contour of reflectivity with 30 dBZ is indicated by black lines in all the panels.

tornado region

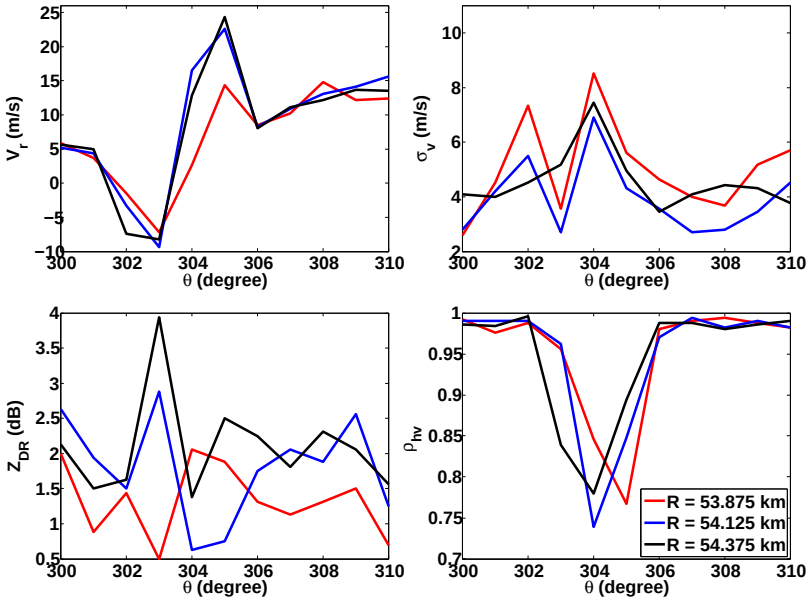

non-tornado region

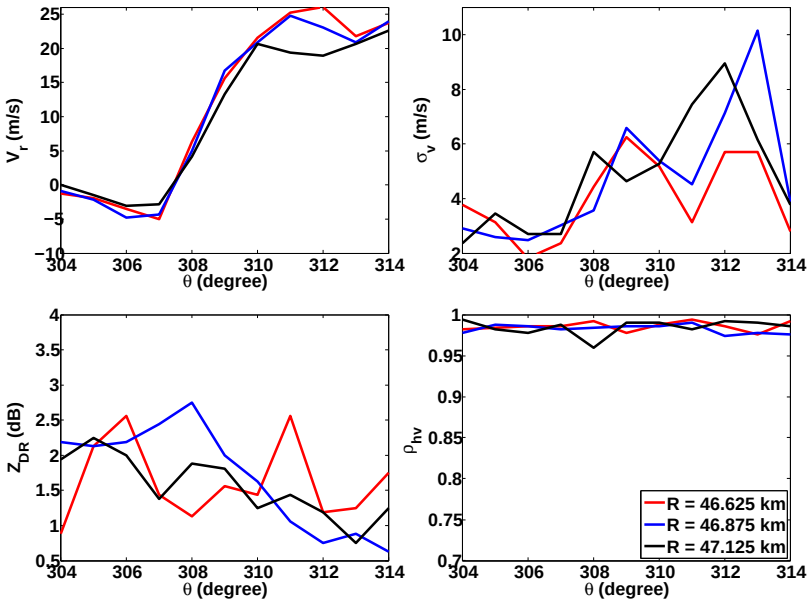

Figure 3.15: (tornado region) the variation of velocity (top left), spectrum width (top right), differential reflectivity (bottom left), correlation coefficient (bottom right) in azimuthal direction across the tornado as indicated by the blue line in each panel. (non-tornado region) similar to (tornado region), but from the nontornado region as indicated by the other blue line in each panel.

good consistency. Therefore, it is difficult to distinguish these two locations if only velocity and spectrum width are used for tornado detection. However, the signatures of Z_{DR} and ρ_{hv} are evident in the tornadic region. These results suggest that the TDS, characterized by low Z_{DR} and low ρ_{hv} has the potential for improving tornado detection especially when velocity and spectrum width cannot provide sufficient information. On the other hand, the TDS may become not resolvable if a tornado is at far range or is over open fields that can not loft debris to heights observable by a radar (Kumjian and Ryzhkov 2008).

The statistical results of TDS and TSS from two tornado events on 8 and 10 May 2003 are provided in chapter 4. For both cases, polarimetric moments were available, but only the time series data from H-channel were collected. Therefore, both TSS and TDS can be obtained to study their impact on the tornado detection developed in this work. However, it is not possible to re-produce polarimetric moments with super-resolution, which will be discussed in section 3.3.2. Additionally, tornado damage paths are available for these two events and can be used as one of the reference to quantify the performance of tornado detection algorithms.

3.3 The Impact of Super Resolution

3.3.1 The impact on tornado velocity and spectral signatures

More pronounced tornado vortex signatures with super-resolution data have been demonstrated using numerical simulation (Brown et al. 2002). Since enhanced TS/TVS can be provided by the super-resolution, it is expected that tornado detection can be improved using super-resolution. In this section, the impact of super-resolution on the tornado velocity signature and spectral signatures are assessed using numerical simulations. It should be note that in this simulation the super-resolution data were

generated using the approach proposed by Brown et al. (2002), where smaller effective beamwidth was obtained owing to the fact that only half of the samples were used. For example, an effective beamwidth of 1.02^o is resulted while the effective beamwidth of legacy resolution is 1.39^o. However, the operational super-resolution is achieved by using the same number of samples as the legacy resolution but with 0.5 ^{o} angular sampling (Torres and Curtis 2007). The operational oversampling scheme is used for the real data analysis in Chapter 4. The tornado velocity signature can be characterized by gate to gate velocity difference ΔV, or the maximum to minimum velocity difference δV, which is similar to TS (TVS) and can be calculated as:

$$\Delta V(i,j) = \max\{[V(i,j+1) - V(i,j)], [V(i,j) - V(i,j-1)]\} \tag{3.18}$$

$$\delta V(i,j) = \max[V(i,j), V(i,j+1)...V(i,j+n)] - \min[V(i,j), V(i,j-1)...V(i,j-n)] \tag{3.19}$$

where i and j represents the gate index in range and azimuthal directions. Since 99 % tornadoes in the northern hemisphere are cyclonic direction (Davies-Jones 1984), ΔV and δV are calculated using the radial velocity on higher azimuthal angle minus the lower one.

The azimuthal gate-to-gate velocity difference ΔV can be calculated easily and has been used in the current tornado detection algorithm (Mitchell et al. 1998). However, δV is more significant than ΔV especially when the tornado is at close range or the size of tornado is large, owing to the fact that the maximum to minimum velocity components can not be sampled from two adjacent azimuthal gates. The TSS characterized by spectrum width σ_v, spectral flatness σ_s, PRIB P and eigenratio χ_R have been discussed in section 3.1.1. The comparisons of the velocity signatures and TSS between legacy and super-resolution as a function of range are presented in Fig. 3.16 and Fig. 3.17, where the superscript of "s" and "l" represent the results from super-resolution and legacy resolution, respectively. In the simulation a tornado vortex was generated using a Rankine combined vortex model with a maximum

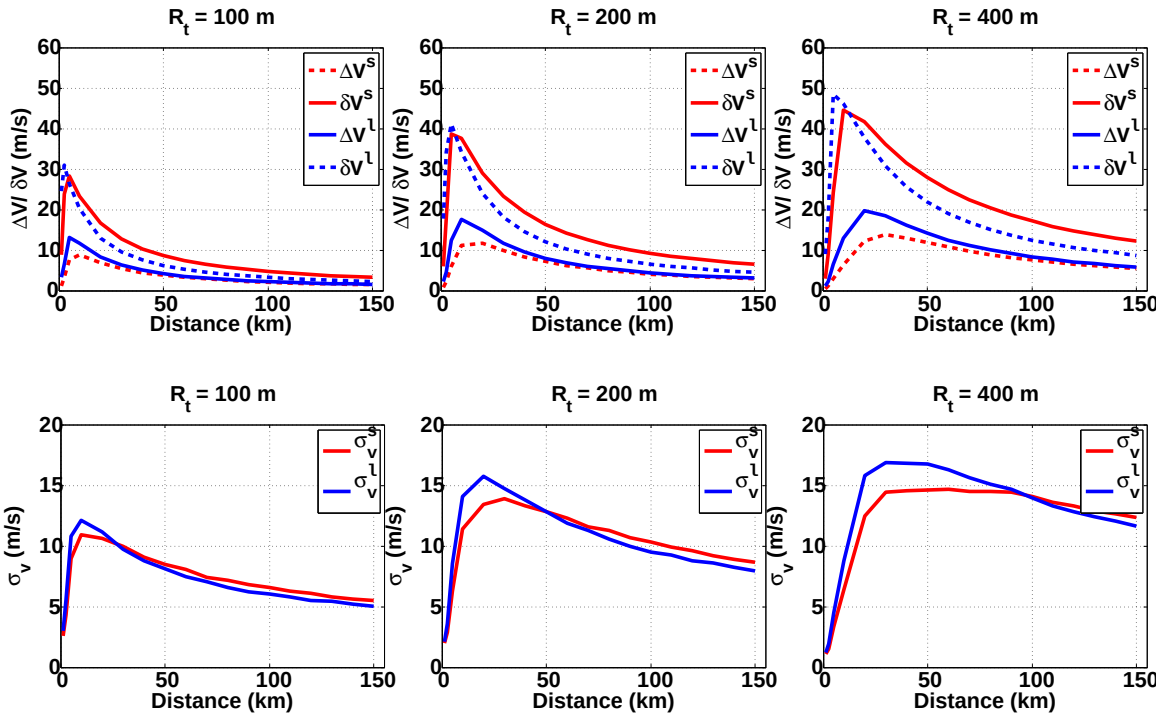

Figure 3.16: Statistical analysis of the ΔV, δV and σ_v as a function of the range for super-resolution and legacy resolution data. The abscissa is the distance from the radar to the center of the resolution volume. The superscript of "s" and "l" represent the results from super-resolution with effective beamwidth $\theta_b = 1.02^o$ and legacy resolution with $\theta_b = 1.39^o$, respectively. The radii of tornadoes are 100 m (left), 200 m (middle) and 400 m (right). The X axis is the normalized range as in Fig. 3.6

tangential and radial velocity of 30 m s^{-1} and 5 m s^{-1}, respectively. Same as WSR-88D radar, the range resolution (ΔR) is 250 m, and effective beamwidth (θ_b) is 1.02^o for super-resolution and 1.39^o for legacy resolution, respectively (Brown et al. 2002). Moreover, the azimuthal sampling for super-resolution and legacy resolution is 0.5^o and 1.0^o, respectively.

Several factors such as the range between the tornado and radar, the size of the tornado, and the relative location of a tornado within the radar's resolution volume determine tornado's shear and spectral signature (e.g., Zrnić et al. 1977; Brown et al.

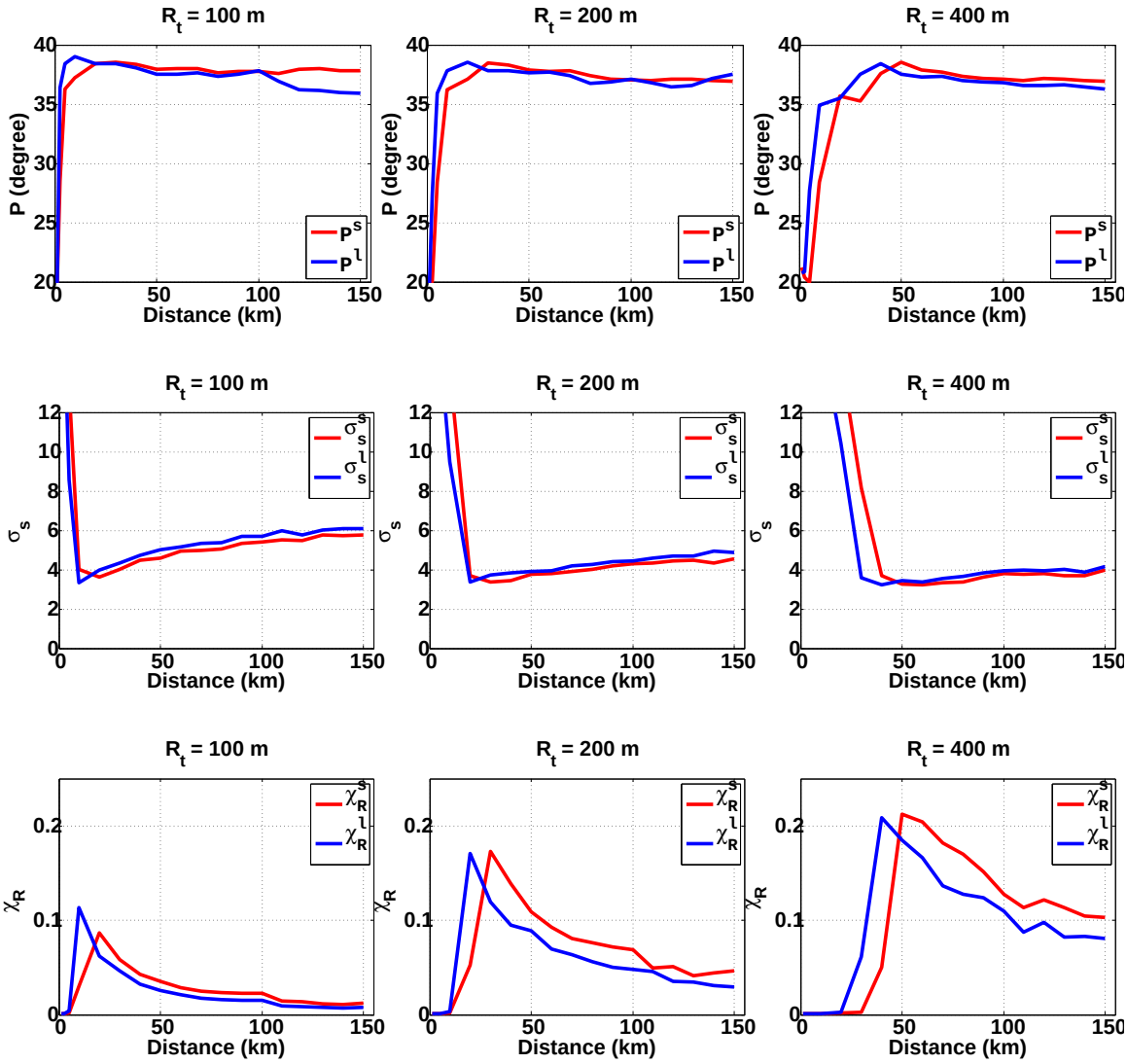

Figure 3.17: Similar as Fig. 3.16, but for P, σ_s, and χ_R.

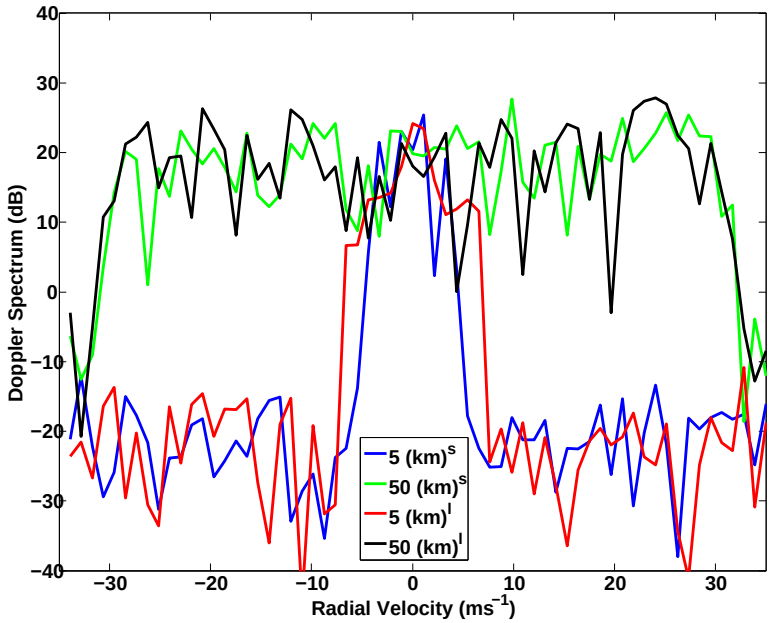

Figure 3.18: Simulated tornado spectra at 5 km and 50 km from super- and legacy resolutions.

2002; Yu et al. 2007). The relationship between the TS/TVS, the size of the tornado and range was studied by Brown et al. (2002). It should be noted that the spectral signatures are also effected by the reflectivity structure as discussed in section 3.1.2. In this section only the uniform reflectivity structure is used in order to simplify the problem and focus on the impact of super-resolution. Similar conclusions can be obtained if the doughnut shape reflectivity structure is used. In this work, the tornado core diameters are set as 200 m, 400 m and 800 m. The range between the tornado and the radar is set from 0 to 150 km. The normalized ranges $r_n = r_0\theta_b/r_t$ are for both legacy and super-resolutions. The tornado was centered on 121 different locations within the radar resolution volume, which was divided into an 11 $\times$ 11 uniform grids. Moreover, for each case 50 realizations were generated with independent noise sequences. The mean of the estimated ΔV, δV, σ_v, P, σ_s and χ_R as a function of range is shown in Fig. 3.16 and Fig. 3.17 for both legacy ans super-resolutions.

In general, the velocity difference (ΔV and δV) and σ_v increase with range at short distances, and then decrease after they reach the maximum values. The velocity difference shows more rapid decrease than the spectrum width. For small tornado (R_t = 100 m), the δV^l shows larger value than the ΔV^l within r_n = 4.8, and the two variables become comparable after that. For super-resolution data, although the difference between δV^s and ΔV^s becomes smaller with increasing distance, the difference is still more obvious than the difference from legacy resolution. This is because the effective beamwidth of super-resolution is three quarters of legacy resolution, which can mitigate the smoothing effect. Moreover, the angular sampling of super-resolution is 0.5 ^{o} which is only half of the legacy resolution, therefore more radial velocities close to the maximum value are likely to be sampled. The difference between ΔV^l and δV^l becomes negligible after 50 km and 90 km for the tornado with radius of 200 m and 400 m, respectively. However, the difference between ΔV^l and δV^l becomes even larger with the increase of tornado size.

The spectrum width estimated from legacy resolution is larger than from super-resolution at close range ($\leq$ 4.8 for R_t = 100 m; $\leq$ 6.0 for R_t = 200 m; $\leq$ 10.91 for R_t = 400 m), and smaller than from super-resolution after those ranges. Since the cross section of radar beam from super-resolution (with effective beamwidth of 1.02^o) is always smaller than from legacy resolution (with effective beamwidth of 1.39^o), if the diameter of tornado is larger than the radar beam cross section (at close range), only portion of the tornado is sampled by the radar. In other words, more velocity components can be included with larger effective beamwidth. This causes the spectrum width from legacy resolution at close range to be larger than from super-resolution. However at far range, since the radar beam cross section is larger than the diameter of tornado, all the velocity components can be sampled. As a result, smaller estimated spectrum width is obtained from legacy resolution because of the

smoothing effect. For the other three TSS parameters of σ_s, P and χ_R, consistent behaviors as σ_v can be observed .

Examples of spectra from tornadoes located at 5 km and 50 km are displayed in Fig. 3.18, where the tornadoes' radius is 400 m. At close range (5 km), since a portion of tornado is sampled by the radar beam, only the velocity components from -10 m s^{-1} to 10 m s^{-1} can be observed in the spectrum. Narrow and flat TSS can be obtained at close range, this is the reason that the σ_v, P and χ_R show such low values, and σ_s shows such high value. Moreover, spectrum obtained from legacy resolution is wider than from super-resolution due to effective beamwidth. At far range (50 km), since the dimension of radar beam in the cross beam direction is larger than the diameter of the tornado, all the velocity components from the tornado can be sampled. Wide and flat TSS can be observed from both legacy and super-resolutions, which is manifested by large σ_v, P and χ_R and low value σ_s.

It is evident that super-resolution data can provide more pronounced velocity and spectral signatures at far ranges, and have the potential for improving tornado detection. Moreover, the maximum to minimum velocity difference is larger than the gate-to-gate velocity difference for super-resolution even at far range. However, for legacy resolution, the difference between ΔV^l and δV^l is relatively small, especially for smaller tornado ($R_t = 100$ m). Therefore, for NFTDA in this work maximum to minimum velocity difference implemented for the super-resolution, and the azimuthal gate-to-gate velocity difference is adopted for the legacy resolution.

3.3.2 The impact on tornado debris signatures

An example of polarimetric TDS is presented in Fig. 3.20, and the radial velocity and spectrum width are presented in Fig. 3.19. Where mean radial velocity V_r, spectrum width σ_v, differential reflectivity Z_{DR} and cross correlation coefficient ρ_{hv} on the left columns are from legacy resolution of 250 m by 1 ^{o}, 250 m by 1 ^{o}, 1 km by 1 ^{o} and

250 m by 1 ^{o}, respectively; the V_r, σ_v, Z_{DR} and ρ_{hv} on the right column are from super-resolution of 250 m by 0.5 ^{o}. To help identifying the tornado location, the outer edge of tornado damage path is indicated by white lines. In the Z_{DR} plot, several consecutive gates in range with negative Z_{DR} ($<$ -1 dB) and exceptionally low value of ρ_{hv} (< 0.85) can be observed around [-70 km, 50 km] for super-resolution, which are located within the tornado damage path. However, positive (or close to zero) Z_{DR} can be observed at this location with legacy resolution. These high Z_{DR} hardly can be recognized as polarimetric TDS and can not be used in tornado detection. In the ρ_{hv} plot for legacy resolution data, there are two gates show low value (< 0.85) at this location. High values (> 0.9) of ρ_{hv} are observed in other locations around [-70 km, 50 km]. In order to examine the behavior of these four parameters, one dimensional plot along the azimuthal direction crossing the tornado location is presented in Fig. 3.21. The tornado is approximately located at azimuth angle of 306^o, where obvious larger σ_v and lower ρ_{hv} can be observed.

The results suggested that the polarimetric TDS is more clearly shown with super-resolution, which can lead to better tornado detection.

3.4 Conclusions

The distinct wide and flat spectral signatures generated by tornadic vortex have been studied by simulation and radar observations. Three parameters of σ_s, P and χ_R were developed to improve the characterization of the tornado spectral signatures (TSSs). Together with spectrum width σ_v, these four tornado spectral signatures have the potential to facilitate tornado detection even when the shear signature becomes difficult to identify. Based on the results of simulation and a real tornado case the value of σ_v, P, σ_s and χ_R obtained in tornado region can be significantly different from those obtained in nontornado regions. Moreover, the results also demonstrated

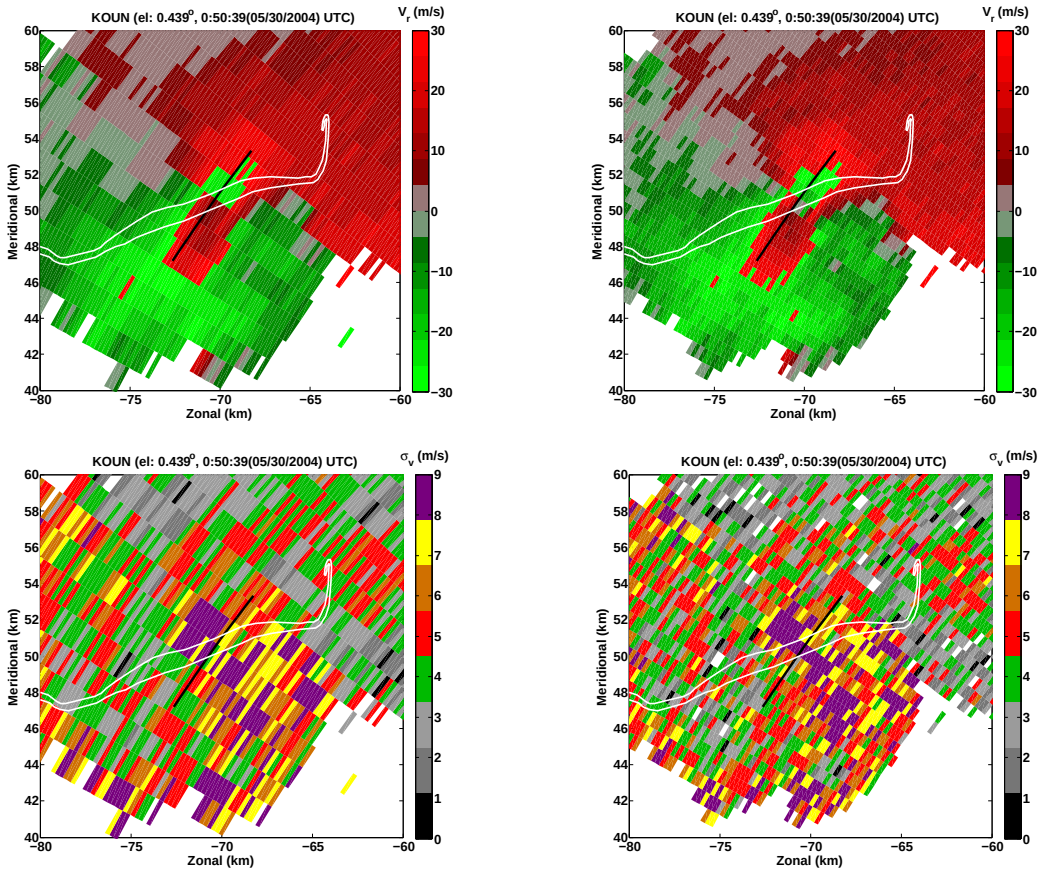

Figure 3.19: The Doppler velocity (V_r) (top), spectrum width(σ_v) (bottom), at 0447 UTC 8 May 2007. The panels on the left column are those with legacy resolution, and on the right column are the ones with super-resolution. The damage path is indicated by white lines, which is used to help identifying the tornado. The 1 dimensional plot indicated by a black line are provided in Fig. 3.21

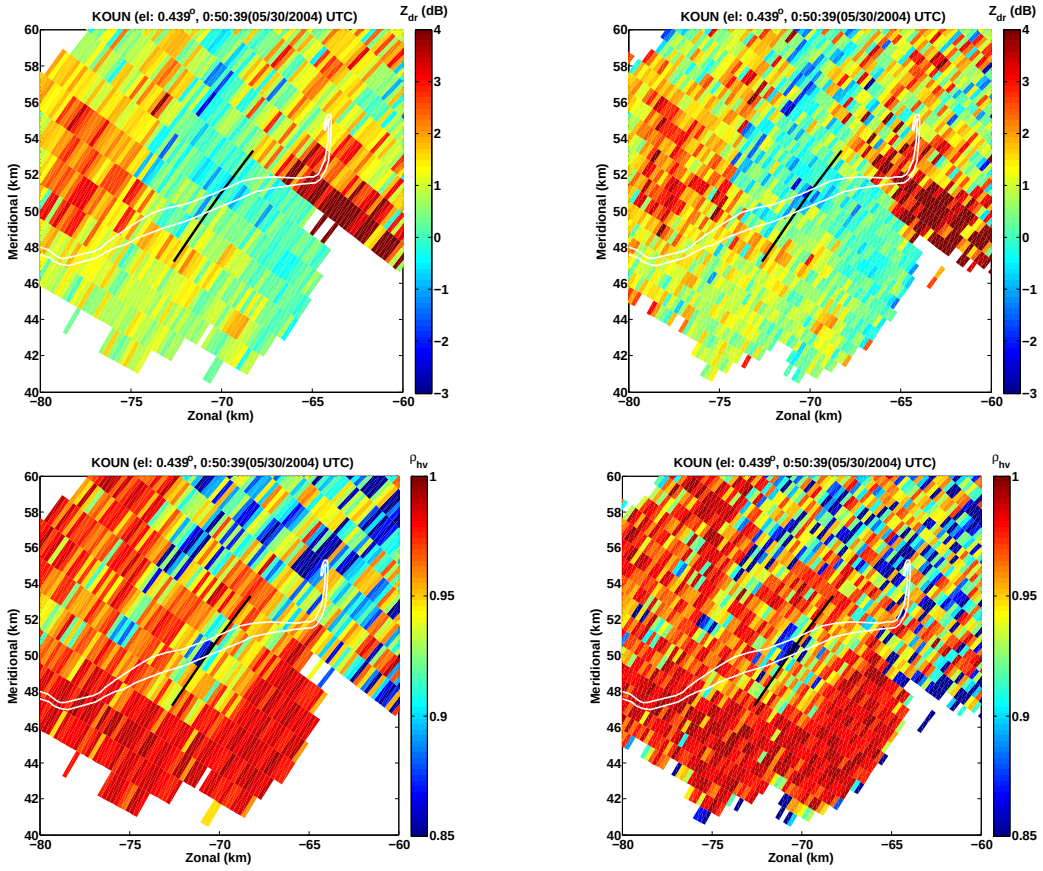

Figure 3.20: Similar as Fig. 3.19, but for Z_{DR} (top) and ρ_{hv} (bottom)

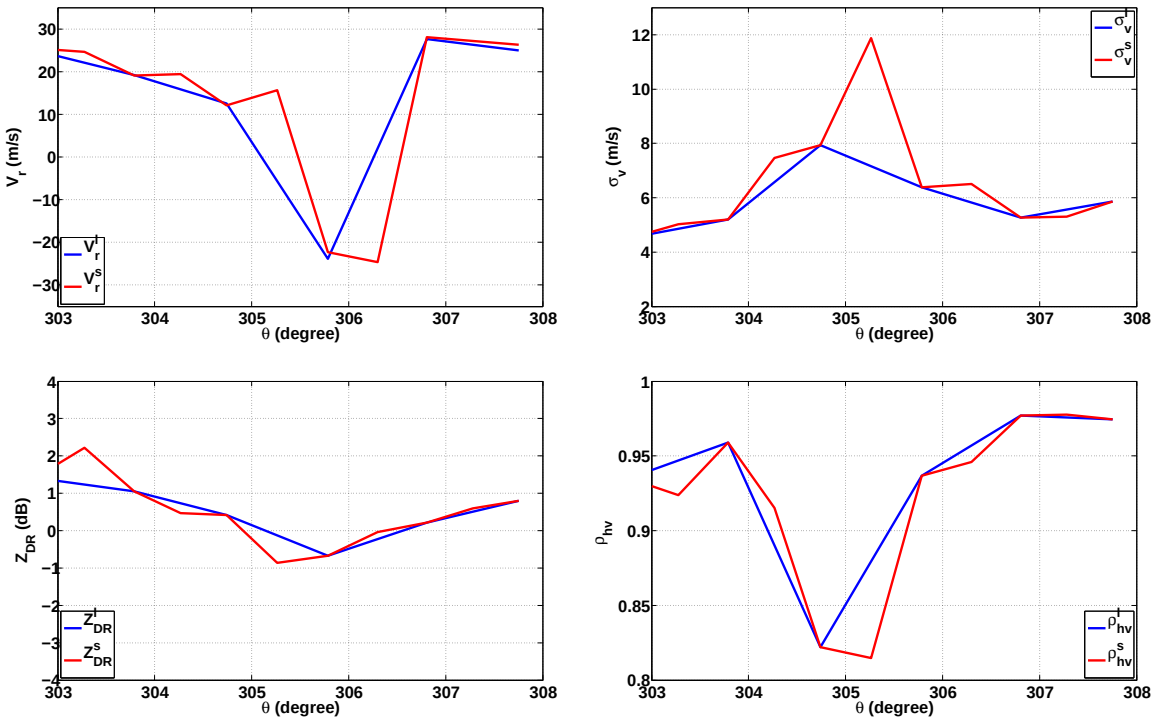

Figure 3.21: The one dimensional plot of Z_{DR} and ρ_{hv} along the black lines in Fig. 3.20. The Z_{DR} and ρ_{hv} from legacy and super-resolution are presented using red and blue lines, respectively.

that P, σ_s and χ_R can assist with the identification of tornado while the information of spectrum width is not sufficient.

Very low values of Z_{DR} and ρ_{hv} defined as tornado debris signatures have been continuously observed in tornadic events. The analysis performed in this chapter, similar to results of earlier work further confirms that TDS has the potential to help with tornado detection. Compared to conventional tornado detection algorithm which only relies on velocity signatures, a novel tornado detection algorithm that integrates these tornado spectral, shear and polarimetric signatures is desirable and will be developed in the next chapter.

Chapter 4

Neuro-fuzzy Tornado Detection Algorithm (NFTDA)

4.1 Motivation and Introduction

In Chapter 3, wide and flat tornado spectral signatures were characterized by four parameters: spectrum width σ_v, spectral flatness σ_s, PRIB P, and eigen ratio χ_R. Simulation results and real cases collected by KOUN indicate that the four variables can be used individually to distinguish tornado spectra from non-tornado spectra for some cases. Furthermore, tornado debris signatures manifested by anomalously low differential reflectivity Z_{DR} and cross-correlation coefficient ρ_{hv} were examined using two real tornado events. Since individual TSS or TDS described in previous chapter have the potential to facilitate tornado detection to some extent, it is desirable to integrate all available signatures with the goal of improving tornado detection compared to the conventional TDA. A novel neuro-fuzzy tornado detection algorithm (NFTDA) was developed by Wang et al. (2008), which integrates shear and spectral signatures with a neuro-fuzzy system. Enhanced detection capability, in terms of high POD, lower FAR and further detection range, using NFTDA was reported. A fuzzy logic methodology is ideal to address a complicated system which launches a decision based on multiple inputs simultaneously. Fuzzy logic systems have already

been applied to weather radar for hydrometer classification, cloud discrimination and AP return filtering (e.g., Vivekanandan et al. 1999; Liu and Chandrasekar 2000; Zrnić et al. 2001; Baum et al. 1997; Kessinger et al. 2003). In this work, a fuzzy logic system is developed to flexibly integrate tornadic signatures in the velocity, spectra and polarimetric measurements based on available parameters from radar observations. The system is further enhanced by a feedback process provided through a neural network and is termed the neuro-fuzzy tornado detection algorithm (NFTDA).

In this chapter, the architecture of the NFTDA is introduced in section 4.2. The performance of the NFTDA for different combinations of input parameters is evaluated in section 4.3. The summary and conclusions are given in section 4.4

4.2 Tornado Detection Using a Neuro-fuzzy Framework

4.2.1 Rationale for applying fuzzy logic to tornado detection

Before demonstrating the use of fuzzy logic in tornado detection, the TSS and TDS parameters are statistically analyzed using data collected from two tornadic events on 8 and 10 May 2003. The normalized histograms of (a) velocity difference, (b) spectrum width, (c) PRIB, (d) Eigen-ratio, (e) spectral flatness, (f) differential reflectivity and (g) cross-correlation coefficient for tornado and no-tornado cases are presented in Fig. 4.1. The time series data were collected by the KOUN radar continuously over the entire tornadic event for approximately one hour on 10 May but only two volume scans of data for the 8 May case. The data from the lowest two elevation angles (0.5^o and 1.5^o) were used to calculate the histograms (associated with 112 gates for tornado cases, and 135,600 gates for non-tornado cases), which were normalized by the total number of data used in the analysis.

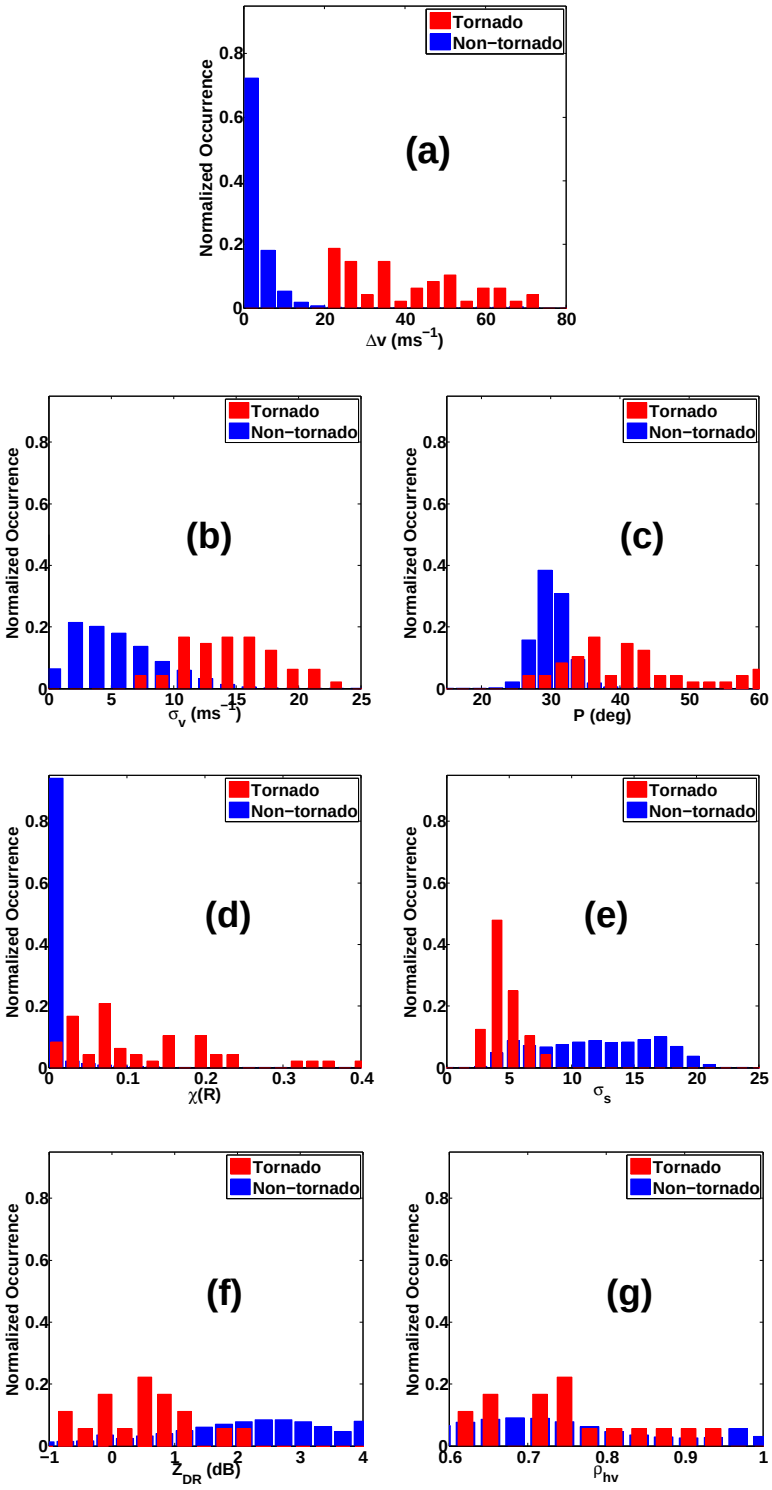

Figure 4.1: Normalized histograms of the parameters to characterize ΔV (a), TSS (b)-(e) and TDS (f)-(g) for tornado (red bars) and non-tornado (blue bars) cases.

A tornadic case is defined by the gate where the velocity difference (ΔV) of its adjacent azimuthal gates is larger than 20 m s^{-1} and within the tornado damage path. Regions outside the damage path with an SNR larger than 20 dB are defined as non-tornado cases. It is shown that the tornado cases are associated with large values of σ_v, ΔV, P, χ_R, but small values of σ_s, Z_{DR} and ρ_{hv}. It is interesting to point out that the distributions of tornadic and non-tornadic cases are overlapped for all the parameters. Thus, the values within the overlapping region cannot be used to represent either tornado or non-tornado cases (i.e., some degree of fuzziness is involved). As a result, a simple thresholding method based on any individual parameter is not sufficient and will produce a certain amount of false or miss detections depending on the threshold. Although the overlapping reign of ΔV is not obvious in Fig. 4.1, where only 1.5% of non-tornadic cases have ΔV larger than 20 m s^{-1}, the number of such cases is significantly larger than the tornadic cases, because the majority of the data are from non-tornadic cases. As a result many false/miss detections may be obtained. Moreover, Yu et al. (2007) have shown cases that PRIB and spectral flatness can help to characterize the TSS while the signatures of shear and spectrum width diminish. The significant low value of Z_{DR} and ρ_{hv} are indicators of tornado debris, which can be used in tornado detection (Ryzhkov and Zrnić 1996). It is important to consider these complementary tornadic features simultaneously in a detection algorithm, and a fuzzy logic is an ideal candidate.

The choice of fuzzy logic over other approaches such as thresholding, decision trees, and neural networks in their pure form is motivated by several considerations. First, as mentioned previously, strong shear, large spectrum width, significant Eigen-ratio, high PRIB, low value of spectral flatness and anomalously low differential reflectivity and cross-correlation coefficient may be associated with a tornado vortex. The description of the degree of significance for each parameter is actually fuzzy in context, since terms like "strong, weak, large, or low" are used to describe their significance.

On the other hand, "crisp" values are binary – these values either exceed or do not exceed a threshold. As such, the fuzzy parameters actually contain more information than the crisp ones, and the intent here is to leverage this additional information that is otherwise typically neglected. In retrospect, thresholding approaches would be ideal if the distributions of tornadic and non-tornadic cases for any of the parameters in Fig. 4.1 are disjointed; however, this is rarely the case for real scenarios. Secondly, a fuzzy logic system can use all the available features simultaneously to reach a conclusion, while a decision tree only uses a single parameter at each node and is exclusive for all other parameters. Moreover, a fuzzy logic architecture is more flexible than a decision tree for incorporating additional parameters without re-adjusting all the rules. Finally, a large amount of training data is typically required to build a robust neural network system in its pure form (Marzban and Stumpf 1996). In contrast, a fuzzy logic system can be developed based on a set of rules that are obtained from *a-priori* knowledge and/or defined by experts. Nevertheless, the self-learning capability provided by the neural network is still attractive and is included here in this hybrid approach to develop NFTDA. As such, the neural network is used to refine the rules to optimize system performance. A similar approach of a neuro-fuzzy combination was developed by Liu and Chandrasekar (2000) for hydrometeor classification with polarimetric products. A schematic diagram of the NFTDA is depicted in Fig. 4.2, and a detailed description of NFTDA is presented in the section 4.2.2 and 4.2.3.

4.2.2 Architecture of fuzzy logic system

A fuzzy logic system can be considered as a non-linear mapping of feature parameters (i.e., inputs) to crisp outputs. In NFTDA the output is a binary detection of the presence of a tornado. This fuzzy logic system consists of three subsystems: fuzzification, rule inference, and defuzzification (Mendel 1995). In fuzzification, the tornado feature parameters (or termed crisp input) of spectrum width, velocity difference, PRIB,

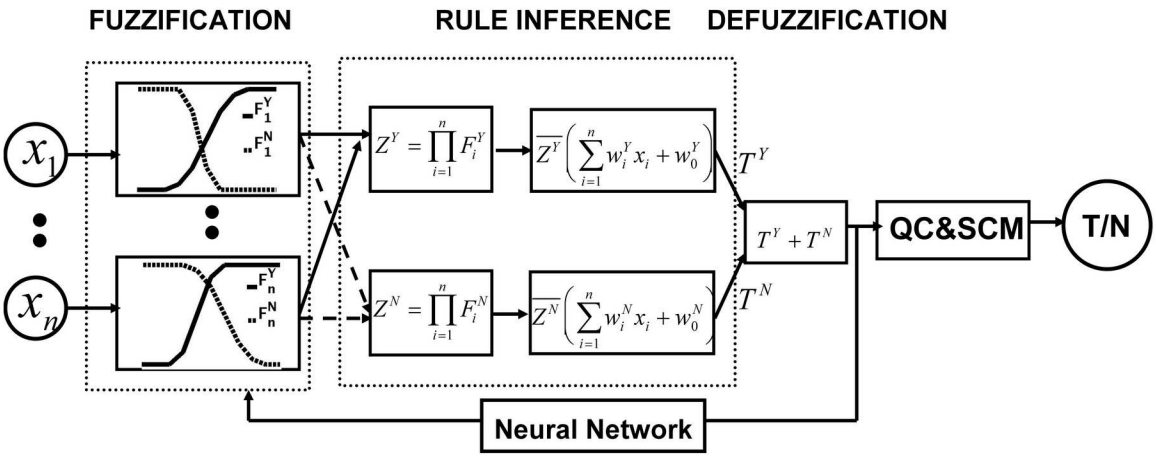

Figure 4.2: The schematic diagram of the NFTDA. A fuzzy logic system is designed to detect a tornado, while a neural network is incorporated to refine the membership functions through a self-learning process. The framework is flexible enough to take in different numbers of parameters. Weighted average is adopted in the rule inference instead of multiplication. A neural network is used to refine the membership functions through a self-learning process. The output of the neuro-fuzzy system is a cluster of radar gates. Those gates associated with non-vortex are eliminated by quality control (QC), and the tornado center is determined using a subtractive clustering method (SCM).

Eigen-ratio, spectral flatness, differential reflectivity and cross-correlation coefficient are converted to fuzzy variables, by either S-shaped curve or Z-shaped curve membership function. An S-shaped membership function of a crisp input x_i is defined by two breaking points (x_i^l and x_i^h) in the following equation.

$$F(x_i) = \begin{cases} 0 & x_i < x_i^l \\ 2(\frac{x_i - x_i^l}{x^h - x_i^l})^2 & x_i^l \leq x_i < \frac{x_i^l + x_i^h}{2} \\ 1 - 2(\frac{x_i^h - x_i}{x_i^h - x_i^l})^2 & \frac{x_i^l + x_i^h}{2} \leq x_i < x_i^h \\ 1 & x_i^h \leq x_i \end{cases} \tag{4.1}$$

where i =1, 2, ..., 7. corresponds to the input parameter. The fuzzy variables for tornadic and non-tornadic cases are denoted by F_i^Y and F_i^N, respectively. Note that a Z-shaped curve membership function is also determined by two breaking points as following equation:

$$F(x_i) = \begin{cases} 1 & x_i < x_i^l \\ 1 - 2(\frac{x_i - x_i^h}{x_i^h - x_i^l})^2 & x_i^l \leq x_i < \frac{x_i^l + x_i^h}{2} \\ 2(\frac{x_i^l - x_i}{x_i^h - x_i^l})^2 & \frac{x_i^l + x_i^h}{2} \leq x_i < x_i^h \\ 0 & x_i^h \leq x_i \end{cases} \tag{4.2}$$

An example of the membership functions for seven tornado signatures as input parameters is presented in Fig. 4.3, where the membership functions of velocity difference, spectrum width, PRIB, eigen-ratio, spectral flatness, differential reflectivity, and cross-correlation coefficient are depicted in a, b, c, d, e, f and g, respectively. It should be noted that the membership functions will be different for different combinations of the input parameters and the resolution of the data (legacy or super-resolution) after neural network training.

The fuzzy variables are the inputs to the subsystem of rule inference with an output of T^Y and T^N for tornadic and non-tornadic cases, respectively, as shown in Fig. 4.2. The number of input variables is denoted by n, and the input parameters can be in either legacy or super-resolution. The relationship between the input and

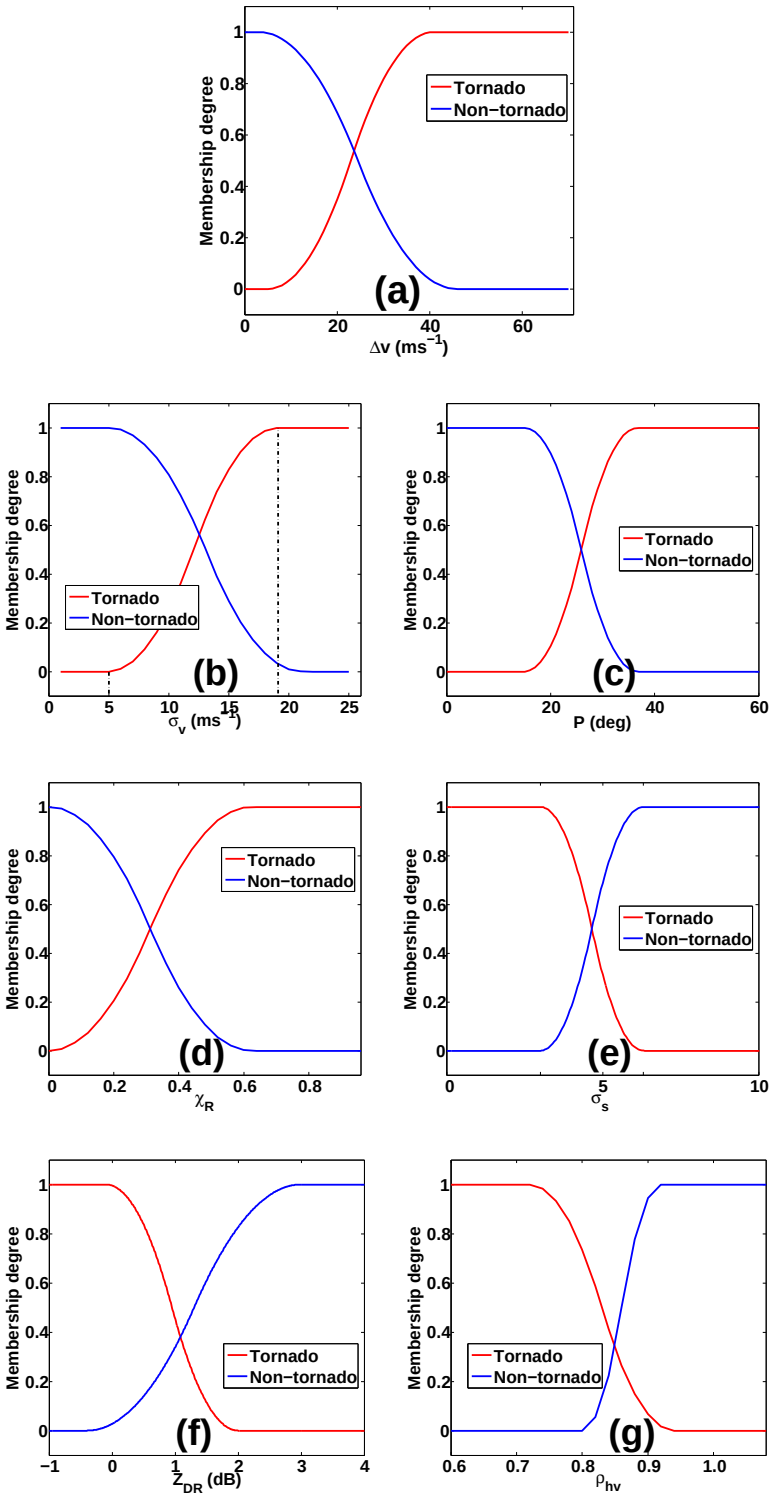

Figure 4.3: Membership functions of tornado signatures.

output of rule inference is described by fuzzy rules. The process of evaluating the strength of each rule is called rule inference. Different from Wang et al. (2008), where multiplication was used, in this dissertation, the Sugeno system of weighted average is selected for the rule inference (Ross 2005). When the tornado velocity and/or spectral and/or debris signatures are not present simultaneously, using weighted average rule inference can still facilitate the detection. On the other hand, the multiplication (i.e., logical AND) is likely to fail in this situation. The weight as well as the membership functions are obtained through the training process of a neural network, which will be introduced in section 4.2.3. There are two layers in rule inference as indicated in Fig. 4.2. In the first layer, the firing strengths of the rules Z^Y and Z^N are calculated as the multiplication of the fuzzy variables. In the second layer, the outputs of rule inference T^Y and T^N are calculated from the normalized firing strengths, weights, and the crisp inputs as indicated in Fig. 4.2. The normalized firing strengths are obtained as $\bar{Z}^Y = \frac{Z^Y}{Z^Y+Z^N}$ and $\bar{Z}^N = \frac{Z^N}{Z^Y+Z^N}$, respectively. Finally, the output of the rule inference, which is still a fuzzy variable, is converted to a crisp output of a precise quantity through the subsystem of defuzzification. In this work, the weighted average defuzzification method is chosen, which sums the T^Y and T^N together. If the output of the defuzzification is larger than a pre-defined threshold (0.5 from the training process in this work), a positive detection of the presence of a tornado is selected; otherwise, it is a non-tornadic case.

The output of NFTDA is a cluster of radar gates associated with portion or all the tornado features. Quality control (QC) procedure is implemented to eliminate those gates where the detections are not continuous in range and height. Only those gates having at least two adjacent neighbor(s) in range direction meet the range continuity and to form the horizontal (2 dimensional) detections. The horizontal detections are further examined at the three lowest elevation angles of 0.5^o (time cut 2), 1.5^o and 2.5^o in the volume coverage patterns (VCPs) of 11 for example. The vertical continuity is

defined by that horizontal detections from each elevation angle are within a restrictive region (2 km in range and azimuthal directions). Those remain gates associated with nonvortex azimuthal shears such as gust fronts can be eliminated by examining the aspect ratio. The aspect ratio, defined as the ratio of the cluster's radial extent to its azimuthal extent, exceeds a predefined threshold (4 in this work), this cluster is discarded. Similar approach was used in Mitchell et al. (1998).

The remaining clusters are assumed from tornadic vortex, and the center of cluster at the lowest elevation angle of 0.5^o is designated to be the tornado center. In this work, the subtractive clustering method (SCM), an extension of the mountain clustering method proposed by Yager and Filev (1994) was used to determine the center of the cluster. Unlike other clustering methods such as fuzzy c-means (FCM) technique, which finds the cluster center with predefined cluster number, SCM can estimate the number of clusters and determine their centers simultaneously. This advantage of SCM is especially important when more than one tornado is present in a given data set. In SCM, each data point is initially assumed to be a potential cluster center. Subsequently a measurement of the likelihood that each data point that would define the cluster center is calculated based on the density of surrounding data points. The data with highest potential is set as the first cluster center, and all the data points in the vicinity (as determined by a predefined radii) of the first cluster are removed. This process is iterated until all of the data is within radii of a cluster center.

In this work, the performances of the NFTDA using four combinations of input parameters are examined using real tornado cases. The combination of different input parameters and resolutions used in this work are listed in Table. 4.1. Where "Check" means this situation is examined in this work.

The reasons to examine only these four combinations are based on the availability of feature parameters, performance behavior, and the research values. First, currently

	NFTDA-D	NFTDA-P	NFTDA-S	NFTDA-A
	$\Delta V + \sigma_v$	$\Delta V + \sigma_v + Z_{DR} + \rho_{hv}$	$\Delta V + \sigma_v + \sigma_s + P + \chi_R$	$\Delta V + \sigma_v + \sigma_s + P + \chi_R + Z_{DR} + \rho_{hv}$
Legacy Resolution	Check	Check	Check	Check
Super Resolution	Check	No	Check	No

Table 4.1: The check list of different combinations of input parameters and resolutions in this work.

most operational WSR-88Ds provide Level II moment data of reflectivity, radial velocity and spectrum width but no Level I time series data are available. From the operational and commercial point of view, using radial velocity and spectrum width as the inputs of NFTDA is the most directly and reasonable option. Second, because the tornado velocity signature is the most important (general) feature to identify a tornado, velocity difference ΔV is adopted in all the combinations. Although TDS have potential in helping tornado detection, low Z_{DR} and ρ_{hv} can be found in plenty nontornado locations. Therefore, the combination of using only Z_{DR} and ρ_{hv} is not examined in this work because of too many false detections. Third, although the TSS is not currently available, its robustness in helping tornado detection is attractive. The combination of TSS and velocity signatures is also analyzed in this work due to its research value.

The NFTDA with only Doppler moments of ΔV and σ_v as inputs is termed NFTDA-D where n = 2; the NFTDA with polarimetric and Doppler moments of σ_v, ΔV, Z_{DR} and ρ_{hv} as inputs is termed NFTDA-P where n = 4; the NFTDA with Doppler moment data and TSS of σ_v, ΔV, P, σ_s and χ_R as inputs is termed as

NFTDA-S where n = 5; and NFTDA-A is represented by $n = 7$ with all the tornado signatures, respectively.

4.2.3 Neural network for system optimization

The membership function is one of the most important components in a fuzzy logic system. It can be obtained from intuition, inference, rank ordering, neural networks and/or inductive reasoning, for example (Ross 2005). In NFTDA, the shape of the membership functions were determined using prior knowledge of the relationship between the feature parameters and fuzzy variables for both tornadoes and non-tornadoes. For example, it is expected that a tornado is likely to have strong ΔV, large σ_v, P, and χ_R, but low σ_s, Z_{DR}, and ρ_{hv}. Therefore, only an S- or Z-shaped membership function is employed. The two breaking points of the S-shaped membership function of spectrum width for the tornadic case is exemplified in Fig. 4.3. The breaking points of each membership function are initialized based on the results of statistical analysis in Fig. 4.1, and same weights ($W_i = 1$, where $i = 1, 2, ..., 7$) are set to all the parameters. Subsequently, the breaking points and the weights W_i are adjusted through a training process using a neural network as depicted in Fig. 4.2. In the training process, the data from two radar volume scans (0341 UTC and 0353 UTC 10 May 2003) at the two lowest elevation angles (0.5^o and 1.5^o) are used as a training data set. Additional data generated from analytical simulations are used as supplemental training data. Each training data point will be assigned one input state: tornado or non-tornado. The tornado data is selected very carefully from those gates associated with large velocity difference, obvious TSS and/or TDS and consistent with the tornado damage path. Corresponding detection results of this fuzzy logic system will be obtained based on present membership functions. If the detection results do not match the input states, the breaking points and the weights will be modified. The training process is achieved by minimizing the root mean square

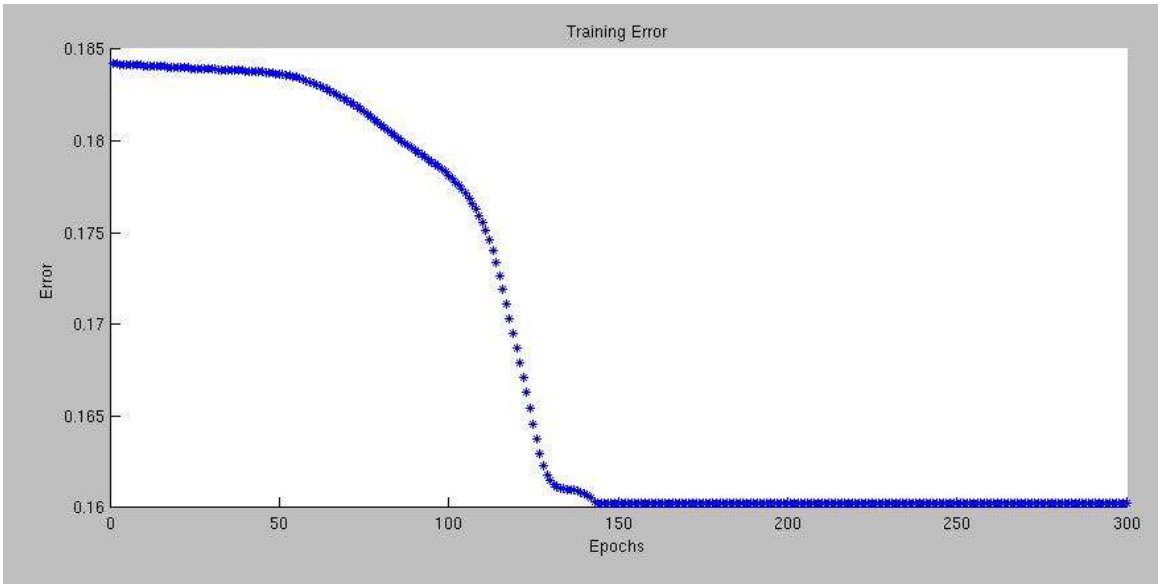

Figure 4.4: A example of the training process to show the variation of RMSE with epochs.

error (RMSE) between the known input states and the detection results through an iterative process (Liu and Chandrasekar 2000). The relation between the RMSE of the training data and the training epoch is presented in Fig. 4.4. The training process is accomplished when the RMSE reaches a pre-defined value (tolerance error). Otherwise, the training process is terminated after pre-defined (10000) iterations. Note that the membership functions shown in Fig. 4.3 were obtained after the training process was completed (RMSE = 0).

4.2.4 Sensitivity analysis of input variables

In this section, the importance of input variables in NFTDA will be studied for the four combination described in section 4.2.2. Heuristic methods have been developed to address this issue (e.g., Sugeno and Yasukawa 1993; Jang 1996; Chiu 1996), where the importance of input variables can be assessed by excluding them in a sequence and comparing the corresponding algorithm performance. However, the computational cost can hinder the feasibility of these methods (Gaweda and Zurada 2001). In

this work, a computational efficient method proposed by Gaweda and Zurada (2001) is used to determine the significance of each input variables by calculating the normalized sensitivity ϑ_i^k defined in the following.

$$\vartheta_i^k = \left|w_i^k\right| \left| \frac{x_i^{\max} - x_i^{\min}}{Y^{\max} - Y^{\min}} \right| \tag{4.3}$$

where "k" represents "Y" and "N", and $1 \leq i \leq n$. The w_i^k is the weight used in the rule inference as shown in Fig. 4.2 and is represented in the following form.

$$Y = T^Y + T^N = \frac{Z^Y \left(\sum_{i=1}^{n} w_i^Y x_i + w_0^Y \right) + Z^N \left(\sum_{i=1}^{n} w_i^N x_i + w_0^N \right)}{Z^Y + Z^N} \tag{4.4}$$

Moreover, the $\left|x_i^{\max} - x_i^{\min}\right|$ define the interval of the value of the i^{th} input variables and $\left|Y^{\max} - Y^{\min}\right|$ is the interval for the output of the rule inference. The ratio can be thought of as a normalization factor for input variables with significantly different values. The significance of a variable is defined by the maximum sensitivity as shown in the following equation (Gaweda and Zurada 2001).

$$\vartheta_i^{\max} = \max\left\{\vartheta_i^Y, \vartheta_i^N\right\} \tag{4.5}$$

The input variable with the smallest ϑ is the least important variable. The weights w_i^k, and the resulted ϑ for each input variable and for the four combinations are listed and discussed in section 4.3.

4.3 Performance Evaluations

In this work, the performance of NFTDA is assessed using four combinations of input parameters for legacy and/or super-resolutions. The list of these combinations is provided in Table 4.1. The performance of NFTDA is statistically analyzed and compared to the conventional TDA. To achieve this goal, a tornado library was established, which includes as many as possible tornado events that are available for this work. Then the tornado detection scores in terms of POD and FAR are calculated and exhibited.

4.3.1 Tornado library and evaluation scheme

In order to evaluate the performance of NFTDA, a library of tornado events with both radar data and tornado locations was established. Currently, the tornado library consists of 49 tornado events occurred during 1993 to 1999 with legacy resolution Doppler moment data, 24 events between March 11^{th} 2008 and September 30^{th} 2008 with super-resolution Doppler moment data, 2 events in 2003 with Doppler moments and Level I time series data for H-channel polarization, 5 events between 2003 to 2008 with Doppler and polarimetric moments. Details of these tornadoes are described in Table 4.4, Table 4.5 and Table 4.8. The selected cases in this work show representativeness of the tornado events from various seasons, different geographical positions, and diverse tornado types. The locations of the WSR-88Ds that recorded these tornado events are indicated in Fig. 4.5. The number and the time period of tornadoes were obtained from the National Climate Data Center (NCDC) record (http://www4.ncdc.noaa.gov/cgi-win/wwcgi.dll?wwEvent Storms). All these tornado events satisfy the following 3 conditions. (1) the tornado's life time is more than 3 minutes, (2) the quality of radar data is good, therefore no missing detections caused by blockage, missing data or corrupted data, and (3) all the tornadoes are located within 150 km from the radar as suggested by Mitchell et al. (1998). The WSR-88D Level II data for these events were acquired from the NCDC website (http://www.ncdc.noaa.gov/nexradinv/), and from the collection of KOUN. Some of these cases were also used for the evaluation of the operational WSR-88D NSSL TDA (Mitchell et al. 1998).

The location of a tornado associated with each radar volume scan was determined from the ground damage path if it was available. Otherwise, the tornado's starting and ending locations and the width of ground damage in the storm report were used to assist the determination of the locations. These locations were further adjusted by carefully examining the location of hook-signature, strong azimuthal shear, and large

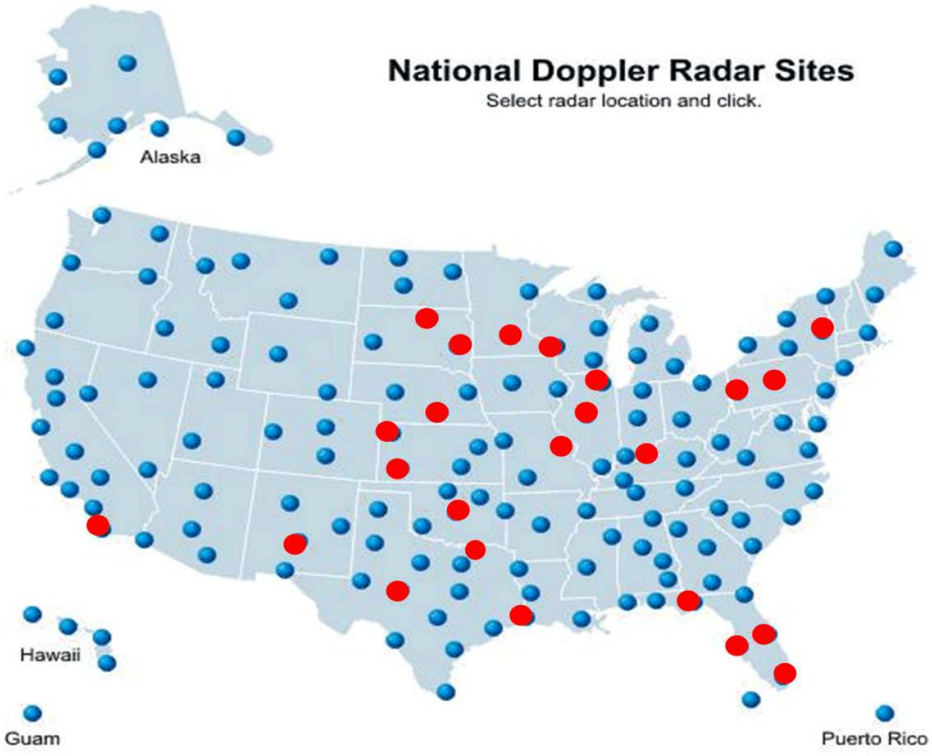

Figure 4.5: The locations of the WSR-88Ds in U.S.. The radar data used in this dissertation were collected by the radars highlighted in red color. (From website:http://www.ncdc.noaa.gov/nexradinv)

spectrum width. Note that the damage path could be different from the location of radar detection, which can be caused by the tilt of the tornado, the width of the radar beam, and the limitation of the mechanical accuracy of the radar for determining the azimuth (Speheger 2006). Similar methodology of adjustment in time and/or location is also implemented by Mitchell et al. (1998) and Witt et al. (1998). For each volume scan, a right detection defined as "hit" is obtained when the detection is within the close vicinity ($<$ 1 km) of the tornado location. Other detections are defined as "false". In addition, a missed detection is obtained if the tornado is present but the algorithm produces no detection. To quantify the performance, the time window scoring method described in Witt et al. (1998) was applied. Algorithms run within the time windows which starts from 15 minutes prior to the beginning time of the tornado to 5 minutes after the ending time (Witt et al. 1998). The POD, FAR, are defined by POD $= a/(a+c)$, FAR $= b/(a+b)$, , where a, b and c represent hit, false and miss, respectively.

4.3.2 NFTDA-D

Since currently the Level II data from WSR-88D are available to the public, implementing NFTDA using features directly from Doppler moments as input parameters shows the most attractive operational and commercial benefit. Therefore, the NFTDA with inputs of spectrum width and velocity difference derived from Level II data is evaluated for both legacy and super-resolution in this section. For the comparison purpose, the NSSL's Warning Decision Support System- Integrated Information (WDSSII) is used to produce TDA results. Since the TDA is only valid for legacy resolution, it is termed as TDA-L (Lakshmanan et al. 2007).

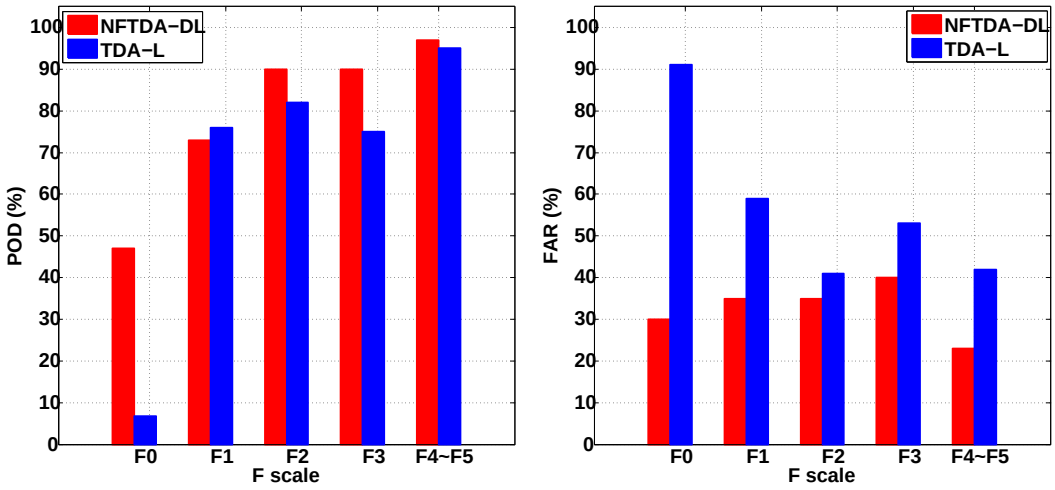

Figure 4.6: Statistical performance of POD (left) and FAR (right). The results are from 49 tornado events. The detection results of NFTDA-DL are indicated by red bars, and the results of TDA-L generated by WDSSII are indicated by blue bars. The abscissa is the intensity of tornado in Fujita Scale.

4.3.2.1 NFTDA-D with legacy resolution data (NFTDA-DL)

The NFTDA-D for legacy resolution data is abbreviated as NFTDA-DL and was trained and tested using 49 tornado events. The membership functions were initialized by results from statistical analysis, and were further tuned by a neural network. Level II moments from 9 tornado events associated with 21 volume scans were used to train the membership functions. The details of the training data set are listed in Table 4.2, where tornado events associated with various Fujita scales (F0 $\sim$ F3) and different ranges (0 $\sim$ 150 km) are included. The training data set are categorized into "close", "median" and "far" according to the ranges of less than 50 km, between 50 km to 100 km and between 100 km to 150 km, respectively. The weights for ΔV and σ_v at each range are listed in Table 4.3. No strong tornado cases (F4 and F5) were included in the training data, but were included in the testing data set. It is apparent that if the well trained algorithm can detect weak tornadoes, it must work for strong tornadoes which are associated with larger velocity differences and spectrum widths.

Date	Radar	County, State	#Volume	Range (km)	Maximum EF-Scale
04/15/94	KLSX	St.Louis, MO	2	0–50	F0
10/07/96	KTBW	Tampa Bay Area, FL	2	50–100	F0
03/24/98	KHNX	Hanford, CA	5	100–150	F0
01/21/90	KLZK	Little Rock, AR	4	0–50	F2
07/03/90	KAPX	Gaylord, MI	1	50–100	F2
02/23/98	KMLB	Melbourne, FL	1	100–150	F2
05/31/96	KABR	Aberdeen, SD	1	0–50	F3
05/17/95	KDDC	Dodge City, KS	2	50–100	F3
02/23/98	KMLB	Melbourne, FL	3	100-150	F3

Table 4.2: Tornado events used for the training of membership functions and weights in NFTDA-DL.

49 tornado cases listed in Table 4.4 were used in the test. The POD and FAR for NFTDA-DL and the TDA-L are shown on the left and right panels of Fig. 4.6, respectively, for different Fujita scales. It is evident that for weak tornadoes of F0-scale the NFTDA-DL provides significant improvement from conventional TDA manifested by much higher POD (from 6.7% to 47%) and lower FAR (from 91% to 30%). Moreover, for this testing data set the maximum detection range of F0 tornadoes using TDA-L is 36 km and the NFTDA-DL can extend the detection to 60 km. For stronger tornadoes (F1-F5), the NFTDA-DL offers comparable or slightly higher PODs compared to TDA-L. It is worth of noting that NFTDA-DL can have significantly lower FAR than TDA-L. For example, for F4 and F5 tornadoes, both algorithms produce comparable PODs of higher than 95%, but the NFTDA-DL can more effectively suppress false detection to produce of FAR 23%, while the FAR of TDA-L is 42%. The performance of NFTDA-DL and TDA-L as a function of ranges is presented in Fig. 4.7.

	$W_{\Delta V}$	W_{σ_v}	W_0
Range $<$ 50 km			
Yes	-0.2325e-03	0.2512e-03	-0.0311e-03
No	0.0268	0.0603	-0.7861
Sensitivity	$\vartheta_{\Delta V} = 1.87 > \vartheta_{\sigma_v} = 0.90$		
50 km $<$ Range $<$ 100 km			
Yes	-0.0972e-05	-0.180e-05	0.7423e-05
No	0.00012	0.00003	1.0007
Sensitivity	$\vartheta_{\Delta V} = 0.61 > \vartheta_{\sigma_v} = 0.33$		
100 km $<$ Range $<$ 150 km			
Yes	-0.0916e-04	-0.1288e-04	0.7280e-04
No	-0.0004	-0.0077	1.0819
Sensitivity	$\vartheta_{\sigma_v} = 0.83 > \vartheta_{\Delta V} = 0.12$		

Table 4.3: The trained weights and the significance sequence for each input parameter in NFTDA-DL.

			Number		(NFTDA/TDA)		
Date	Radar	County, State	#Tornado	#Volume	Hit	Miss	False
05/31/96	KABR	Aberdeen, SD	1	29	7/5	3/5	4/7
05/22/95	KAMA	Amarillo, TX	1	10	1/2	0/1	0/1
07/03/99	KAPX	Gaylord, MI	1	13	4/4	0/0	0/0
05/21/98	KCYS	Cheyenne,WY	1	85	0/0	5/5	0/0
05/16/95	KDDC	Dodge City, KS	1	71	3/3	0/0	3/3
05/27/97	KEWX	Austin, TX	9	81	17/11	9/15	3/1
03/29/98	KFSD	Sioux Falls, SD	2	87	25/9	0/16	1/4
05/07/95	KFWS	Dallas/Fort, TX	2	41	12/8	5/9	3/1
05/12/95	KGLD	Goodland, KS	3	72	12/12	0/0	1/2
11/16/93	KHGX	Houston, TX	5	67	4/2	6/8	2/2
04/07/98	KILX	Lincoln, IL	4	137	6/6	5/5	2/3
01/02/99	KLCH	Lake Charles, LA	9	74	12/12	5/5	17/22
04/15/94	KLSX	St. Louis, MO	2	49	3/2	6/7	3/9
05/28/96	KLVX	Louisville, KY	2	33	13/13	1/1	4/10
03/29/98	KMPX	Minneapolis, MN	2	36	15/15	3/3	9/20
01/29/98	KNKX	San Diego, CA	1	12	0/0	5/5	0/0
04/03/99	KSHV	Shreveport, LA	1	32	12/11	9/10	7/17
09/02/98	KTBW	Tampa Bay, FL	2	45	5/4	8/9	1/0

Table 4.4: Tornado events used in the testing of NFTDA-DL parameters for legacy-resolution data.

			Number		NFTDA/TDA		
Date	Radar	County, State	#Tornado	#Volume	Hit	Miss	False
07/02/08	KDMX	Des Moines, IA	1	25	3/3	6/6	3/3
07/10/08	KDVN	Davenport, IA	2	14	7/0	7/14	8/2
08/24/08	KFTG	Denver, CO	1	9	0/0	6/6	0/0
06/04/08	KIND	Indianapolis, IN	2	14	8/6	2/4	6/10
07/14/08	KLNX	North Platte, NE	2	14	4/0	8/12	0/0
08/02/08	KLWX	Sterling, VA	2	14	4/0	8/12	0/0
05/08/03	KOUN	Norman, OK	1	6	2/0	0/2	2/3
05/10/03	KOUN	Norman, OK	3	12	9/5	0/4	2/3

Table 4.5: Tornado events used in the testing of NFTDA-DS parameters for super-resolution data.

The main idea of TDA is searching for 3D shear feature based on multiple thresholds. If the tornado is weak, such as F0 cases, the shear signature becomes too weak to meet the thresholds, and the miss detections can occur. Additionally, if a tornado is strong but is located at far range, the increased radar beam cross-section will also smooth velocity shear so it becomes undetectable. On the other hand, large velocity difference can also be caused from non-tornado events, such as gust front, squall lines, velocity aliasing and second-trip echo. False detections are likely generated if these situations are not dealt with caution in current TDA. However, because a tornado can generate large spectrum width (above 6 m s^{-1}) and this large spectrum width can be better maintained at far ranges, miss detections generated by TDA that associated with small velocity difference but large spectrum width can be detected by NFTDA-DL. Moreover, since the training process was accomplished with plentiful of real tornado cases, with the obtained membership functions, the optimal combination

	$W_{\Delta V}$	W_{σ_v}	W_0
Yes	-0.1866e-06	-0.1108e-06	0.5035e-06
No	0.00001	0.00002	1.0020
Sensitivity	$\vartheta_{\Delta V} = 0.54 > \vartheta_{\sigma_v} = 0.38$		

Table 4.6: The trained wights and the significance sequence for each input parameters in NFTDA-DS.

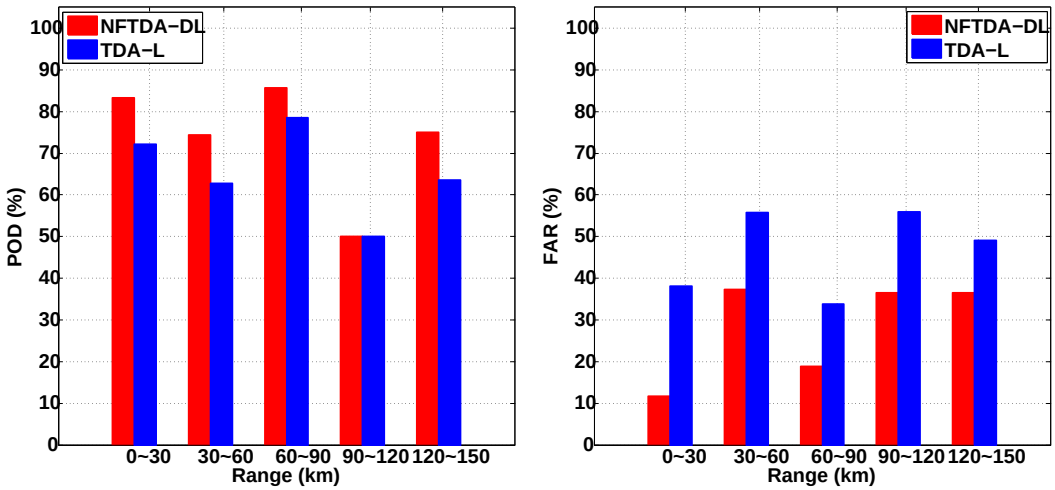

Figure 4.7: Similar to Fig. 4.6, but the abscissa is the distance from tornado to radar in very close range (0 $\sim$ 30 km), close range (30 $\sim$ 60 km), median range (60 $\sim$ 90 km), far range (90 $\sim$ 120 km) and very far range (120 $\sim$ 150 km).

of velocity difference and spectrum width are implemented in NFTDA-DL. Some false detections generated by TDA that associated with large velocity difference but small spectrum width can be eliminated.

The importance of input variables at the three different range intervals is obtained using Eqs. (4.3 and 4.5) and is listed in Table 4.3. It is interesting to point out that for "close" and "median" ranges, ΔV is more important than σ_v ($\vartheta_{\Delta V} > \vartheta_{\sigma_v}$). Moreover, for "far" range, the algorithm depends more on σ_v than ΔV. It is expected that at far ranges the shear signature become degraded and the spectrum width still maintains tornado spectral signature to some extent.

4.3.2.2 NFTDA-D with super-resolution data (NFTDA-DS)

Enhanced velocity difference and comparable tornado spectral signatures (worse than legacy resolution at close range but better at far range) using super-resolution can be observed from the simulation results demonstrated in Fig. 3.16 and Fig. 3.17. For super-resolution, NFTDA-D was re-trained and is termed NFTDA-DS. 13 tornado cases of Fujita scale from F0 to F3 with super-resolution moment data were initially identified out of 1470 tornado cases archived in the NCDC from March 11 2008 to September 30 2008. Radar data from two volume scans of a F0 tornado case recorded by KFTG, and three volume scans of a F1 tornado case recorded by KDVN were used for training, and the trained weights and the sequence of significance of each parameters are listed in Table 4.6. Tornado cases used for testing are listed in Table 4.5.

Due to the limitation of available events with super-resolution, tornadoes are only classified into weak case with Fujita scale of F0 and F1 and strong case with F2-F5. Moreover, in order to compare with detection results with legacy resolution, the NSSL's WDSSII was used to simulate/convert Doppler moments from super-resolution to the legacy resolution, which were subsequently fed to the NFTDA-DL

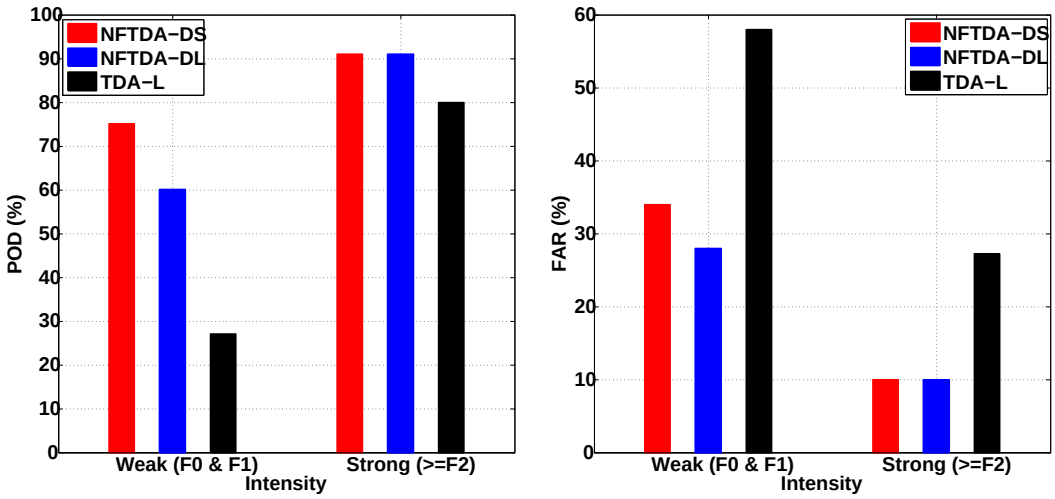

Figure 4.8: Similar to Fig. 4.6, but for super-resolution data.

and TDA-L. The POD and FAR from the three approaches are presented in Fig. 4.8. For the legacy resolution, the NFTDA-DL exhibits higher POD and lower FAR than TDA-L, which is consistent with previous results as shown in Fig. 4.6. It is interesting to note that for weak tornadoes the super-resolution NFTDA-DS has enhanced POD of 75% and slightly worse FAR of 33%, compared to the legacy NFTDA-DL with POD of 60% and FAR of 28.3%. Note that, the POD and FAR for NFTDA-DS were obtained using δV, which shows apparent improvement compared to the one using ΔV. However for the NFTDA-DL, the POD and FAR from δV are identical to ΔV, so that the ΔV is implemented due to the computation efficiency. It has been demonstrated in section 3.3 that δV provides better velocity difference signature than ΔV, and likely produce higher POD in NFTDA. However, the difference between the δV and ΔV is also related to the tornado size, distance, and relative location of tornado inside the radar resolution volume. Therefore, the negligible difference between the results from δV and ΔV for legacy resolution in this work are likely from the tornado events used.

4.3.3 NFTDA-S

4.3.3.1 Performance evaluations with real cases

The performance of NFTDA using Doppler moments and TSS for legacy resolution data (NFTDA-SL) is assessed using two tornadic events in central Oklahoma on 8 and 10 May 2003. The tornado outbreaks on 10 May are of primary interest because continuous time series data were collected by KOUN for the entire event. The NCDC reported that three tornadoes from the same supercell thunderstorm occurred in central Oklahoma from 0329 UTC to 0425 UTC on 10 May 2003 (http://www.ncdc.noaa.gov). The first tornado touched down at 0329 UTC and had traveled 18 miles for approximately 37 minutes before dissipating. The maximum intensity of this tornado was reported at F3 on the Fujita scale. The second tornado, which was estimated to be of F1 maximum intensity touched down approximately 4 miles south of Luther, Oklahoma at 0406 UTC and had lasted for approximately 9 minutes with 3 miles of track. The final tornado occurred between 0415 and 0424 UTC with a maximum intensity of F0. These tornadoes showed discontinuous tracks and collectively lasted approximately 56 minutes, which is similar to the multiple cores mesocyclone described by Burgess et al. (1982) and Adlerman et al. (1999). The tornado damage path with Fujita scale from the ground survey is presented in the upper portion of Fig. 4.9. The damage path of the 8 May tornado is also included in the lower portion of the figure. The NCDC has reported that this tornado had a maximum intensity of F4 and had traveled approximately 18 miles from 2210 UTC to 2238 UTC. However, the collection of time series data by KOUN did not start until approximately 2230 UTC and therefore, only two volume scans of the data are associated with the tornado.

All the feature parameters were calculated from the raw time series data collected by KOUN in Norman, OK. The membership functions were trained using the data from two radar volume scans (0341 UTC and 0353 UTC 10 May 2003) at the elevation

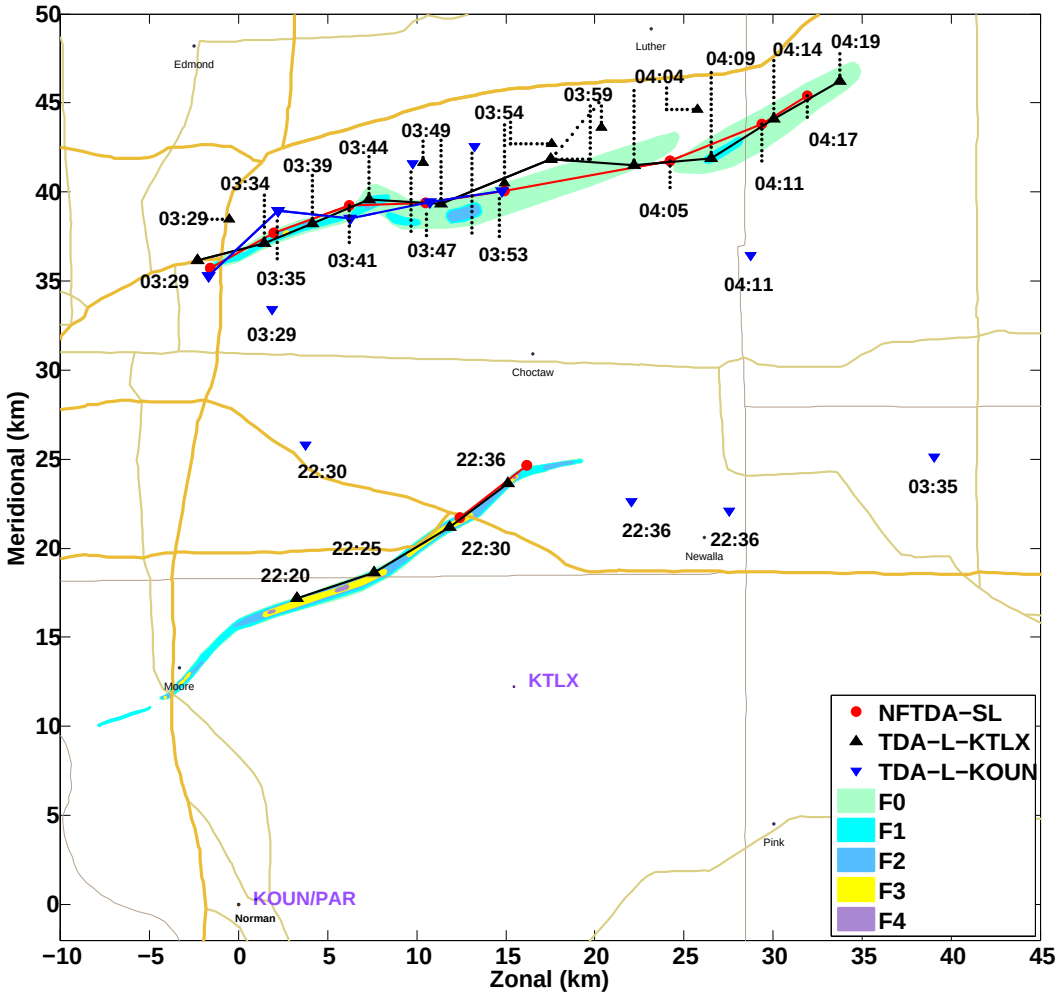

Figure 4.9: Comparisons of the detection results from TDA-L-KOUN and NFTDA-SL, which are denoted by blue triangles and red circles respectively, for both tornadoes on 8 and 10 May 2003. Moreover, the TDA results from the operational WSR-88D at Twin Lakes, OK (TDA-L-KTLX) are depicted by black upward triangles. The location of both KOUN and KTLX is indicated. The detection of "hit" from each approach is connected by a solid line to show the time continuity. Ground damage paths with Fujita scales are depicted by color-shaded contours.

angles of 0.5^o and 1.5^o. The trained weights for each parameters are listed in Table 4.7. Subsequently NFTDA-SL was applied to the data with SNR larger than 20 dB. More details related to the implementation of NFTDA can be referred to section 4.2.2. The NSSL's TDA was also applied to the KOUN Level II data and the detection results are abbreviated by TDA-L-KOUN. For the verification of NFTDA-SL and TDA-L-KOUN, tornado damage path from ground survey is used as an objective reference. However, the damage path may not be available in suburb areas and can be different from the real tornado location. The limitation of using damage path to verify the performance of the detection algorithm is discussed by Witt et al. (1998). Moreover, TDA results from the KTLX radar (denoted by TDA-L-KTLX) is used as another reference. The maximum distance between the KTLX and the 10 May tornadoes is approximately 32 km and it is expected that the TDA-L-KTLX will provide accurate and reliable detections for most cases at such relatively short ranges (Mitchell et al. 1998). In addition to both objective references we carefully examined both spectral and shear signatures for each detection and consequently classify the result to "hit", "miss", or "false" detection.

Comparisons of the detections from NFTDA-SL, TDA-L-KOUN, and TDA-L-KTLX for both 8 and 10 May tornadoes are summarized in Table 4.8. Note that only these TDA-L-KTLX detections with time index close to KOUN detections are included in the table. The scoring statistics shown in Table 4.8 were calculated from all the detections shown in Fig. 4.9. For these two tornadic events, it is evident that NFTDA-SL can improve the shear-based TDA-L-KOUN to provide high POD, low FAR, and high CSI. In addition, TDA-L-KTLX has perfect POD of 100% with maximum detection of approximately 32 km, while NFTDA-SL has comparable POD of 91% with maximum detection of approximately 55 km. Moreover, NFTDA-SL has the lowest FAR among the three approaches. Note that NFTDA-SL has one miss

	$W_{\Delta V}$	W_{σ_v}	W_P	W_{σ_s}	W_{χ_R}	W_0
Yes	1.7861	-12.1282	-3.5112	5.6723	20.9741	-37.9901
No	-0.0051	0.0432	-0.0280	0.37135	-0.3301	0.4962
Sensitivity	$\vartheta_{\sigma_v} = 0.67 > \vartheta_{\Delta V} = 0.51 > \vartheta_{\sigma_s} = 0.48 > \vartheta_P = 0.11 > \vartheta_{\chi_R} = 0.09$					

Table 4.7: The trained wights and the significance sequence for each input parameters in NFTDA-SL.

detection at 0359 UTC where no obvious tornado velocity and spectral signatures can be observed. The velocity deference and TSS plots are provided in Appendix A.

The NFTDA-S using super-resolution (NFTDA-SS) shows same performance as the legacy resolution for the cases in this work. Therefore no separate figures are provided for the results from NFTDA-SS. The relative close range and obvious velocity and spectral signatures are the key reasons causing the detection results from NFTDA-SL and NFTDA-SS same. Although enhanced velocity and spectral signatures can be observed for super-resolution through simulation in section 3.3, the detection results from more real tornado cases are needed to further verify this conclusion.

4.3.3.2 Simulation results

Since only very limited cases are available for the examination of the NFTDA-S, in order to further understand the behavior of the NFTDA-S (including NFTDA-SL and NFTDA-SS), simulated Level I time series data of an idealized vortex (Rankine vortex) generated from a radar simulator developed by Yu et al. (2007) were used. It should be note that the simulated super-resolution data is generated following the approach proposed by Brown et al. (2002), which is different from the operational one as mentioned in Chapter 3. Here, a tornado located at 1 km southwest of the center of a mesocyclone is simulated. Both tornado and mesocyclone are modeled by a Rankine

Time (UTC) KOUN/KTLX	TDA-L-KOUN		NFTDA-SL		TDA-L-KTLX	
	Detection Result	Range (km)	Detection Result	Range (km)	Detection Result	Range (km)
10 May 2003						
0329/0329	hit	35.188	hit	35.625	hit	27.358
	false	33.336			false	28.968
0335/0334	hit	38.892	hit	37.625	hit	27.358
	false	46.352				
0341/0339	hit	38.892	hit	39.625	hit	25.749
0347/0349	hit	40.744	hit	40.625	hit	25.749
	false	42.596			false	27.358
0353/0354	hit	42.596	hit	42.625	hit	25.749
	false	33.336			false	27.358
0359/0359	miss	N/A	miss	N/A	hit	27.358
					false	28.968
0405/0404	miss	N/A	hit	48.125	hit	27.358
					false	30.577
0411/0409	false	46.30	hit	52.625	hit	28.968
0417/0419	miss	N/A	hit	55.375	hit	32.165
8 May 2003						
2230/2230	miss	N/A	hit	24.875	hit	9.656
2236/2235	false	25.928	hit	29.375	hit	11.265
	false	31.484				
	false	35.188				
POD	55.6 %		90.9%		100%	
FAR	61.5 %		0%		33.3%	
CSI	29.4 %		90.9%		75%	

Table 4.8: Comparison of NFTDA-SL, TDA-L-KOUN, and TDA-L-KTLX for 8 and 10 May 2003 tornadoes. The time index of each volume scan for both KOUN and KTLX is given in the first column. The detection result and the range of detection are presented for the three methods.

combined vortex model with a maximum tangential velocity of 50 m s^{-1} and 15 m s^{-1}, respectively. The radius of the mesocyclone is 2 km and three different tornado's radius (r_t) are used in the simulation. Moreover, uniform reflectivity (Wood and Brown 1997; Brown 1998; Brown et al. 2002), is applied to the tornado and a broad Gaussian-shape reflectivity is used for the mesocyclone. The Level I time series data are simulated for a WSR-88D radar with a 1.39^o degree beamwidth (θ_b) for NFTDA-SL and 1.02^o for NFTDA-SS, and a 250 m range resolution (ΔR). The maximum unambiguous velocity is 35 m s^{-1}. The mean Doppler velocities and spectrum widths are estimated by the autocovariance method (Doviak and Zrnić 1993). The spectral flatness, PRIB, and Eigen-ratio are estimated by the methods described in Yu et al. (2007) and Yeary et al. (2007).

It has been shown that tornado's shear and spectral signatures depend on several factors such as the range between the tornado and radar, the size of the tornado, and the relative location of a tornado in the radar's resolution volume. In this work, the ratio of detection, defined as $ROD = N_d/N_t$, is introduced to quantify the performance of NFTDA-S in the simulation, where N_t is the total number of tornadic cases generated for the test and N_d is the number of cases detected. For each realization 121 tornado locations in the radar resolution volume are simulated with 11×11 uniform grids in azimuthal and range directions at a given range (i.e., $N_t = 121$). The radar resolution volume of interest is centered at an azimuth of 0^o. For each tornado location, the five feature parameters (velocity difference, spectrum width, spectral flatness, PRIB, and Eigen-ratio) are obtained as the inputs of NFTDA-S. The ratio of detection can be thought of as the POD for different tornado's locations within the radar resolution volume. The ROD as a function of the normalized range is presented in Fig. 4.10 for the three tornado sizes that are defined by $\Delta R/r_t$, where $r_t = 50$, 100, and 200 m. The normalized range is defined as $r_0\theta_b/r_t$, where r_0 is the range from the radar to the center of resolution volume. Each data point represents the mean of ROD

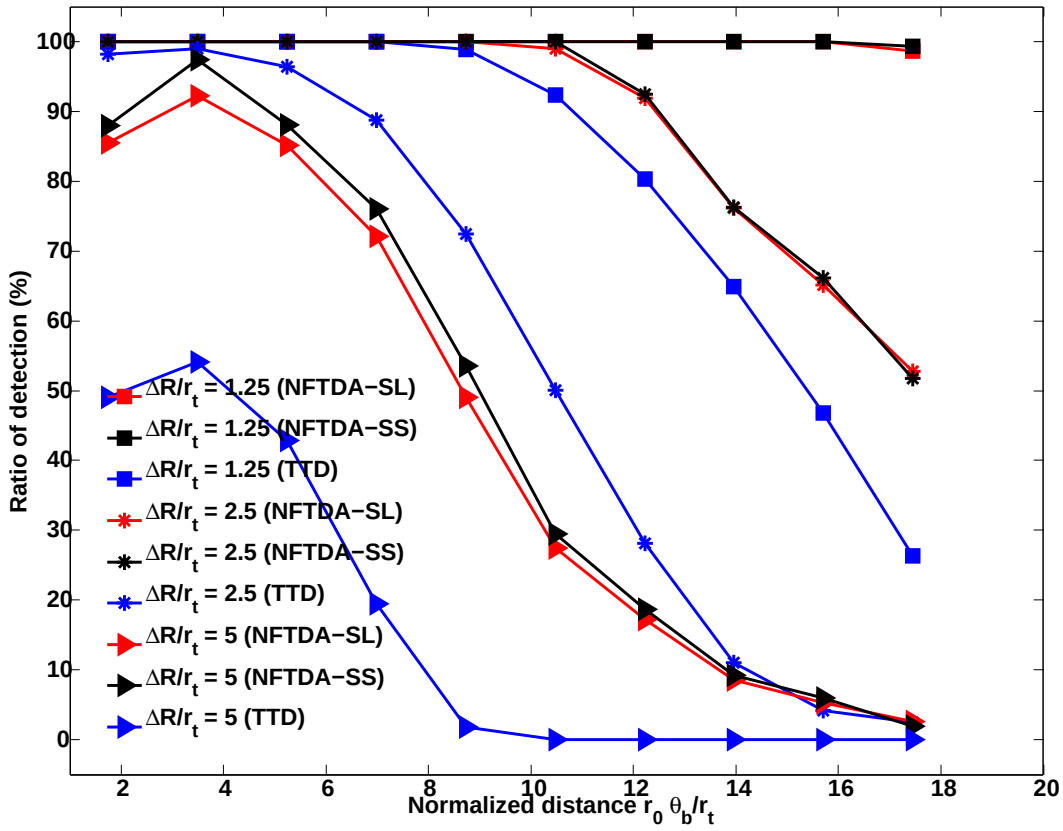

Figure 4.10: Statistical analysis of the performance of NFTDA-SL and NFTDA-SS as a function of normalized range for $\Delta R/r_t = 1.25$, 2.5, and 5.0, where $\Delta R = 250$ m is the range resolution. The abscissa is the normalized range with r_0 is the distance from the radar to the center of the resolution volume, θ_b is the beamwidth (1.39^o for legacy and 1.02^o for super-resolution), and r_t is the radius of the tornado. The results from NFTDA-SL, NFTDA-SS and the detection based on a threshold of velocity difference of 20 m s^{-1} (TTD) are denoted by red, black and blue lines, respectively.

from 50 realizations, and each one has a different noise sequence added to the time series data. For the purposes of comparison, a tornado detection solely based on the thresholding of velocity difference is also implemented and is termed "thresholding tornado detection" (TTD). Since the operational TDA is only for legacy resolution data, the TTD which is used to simulate the performance of TDA only uses legacy resolution data. The ROD from the TTD using a threshold of 20 m s^{-1}, one of the thresholds used in the NSSL's TDA (Mitchell et al. 1998), is provided in Fig. 4.10. Note that both the range and range resolution are normalized by the tornado's radius so that the detection result is scalable for radar with different beamwidth and range resolution.

In this section, the membership functions implemented in NFTDA-SL and NFTDA-SS were obtained from the training process of the same data set as mentioned in section 4.3.3.1. It is evident that NFTDA-SL and NFTDA-SS provide higher RODs than TTD especially at far ranges for the three tornado sizes. For example, NFTDA-SL, NFTDA-SS and TTD have RODs of approximately 100% when the normalized distance is smaller than 8.7 and $\Delta R/r_t = 1.25$ (i.e., a relatively large tornado). As the range increases, ROD from TTD declines because of the diminishing shear signatures. However, NFTDA-SL and NFTDA-SS still have high RODs because spectral signatures are still evident enough to facilitate the detection. Although the performance of TTD can be improved by lowering the threshold, false detections will likely increase. The NFTDA-SS shows similar or better performance than the NFTDA-SL, which consistent with the simulation results in section 3.3. For the large size tornado $\Delta R/r_t = 1.25$, 2.5, the improvement of using super-resolution at close range ($r_o\theta_b/r_t$) is not obvious. Apparent enhancement can be observed for tornado with $\Delta R/r_t = 5$ especially at close range, which is consistent with the simulation results in section 3.3.

To better understand the strengths and weaknesses of NFTDA-S (NFTDA-SL and NFTDA-SS), it is advantageous to investigate the regions where NFTDA-SL,

NFTDA-SS and TTD detect and miss. One realization of the velocity difference for 121 tornado's locations with the resolution volume, defined by 1.39^o beamwidth and 250 m resolution, and at a normalized range of 7 is exemplified in the upper panel of Fig. 4.11 for $\Delta R/r_t = 5$. Note that the tornado is present for all 121 cases. TTD has 20 positive detections which results in a ROD of 16.5%. It is interesting to point out that large velocity differences occur if a tornado is located closer to the boundaries of a radar resolution volume in azimuth and toward the center of the radar resolution volume in range. If an ideal tornado with a size smaller than the radar resolution volume is centered at azimuth angle of -0.5^o (i.e., the boundary of the radar beam) and the center of the gate, then the mean Doppler velocities from the two adjacent radar volumes in azimuth (the one centered at 0^o and the other one centered at -1^o) have the same magnitude but with opposite signs because of the symmetry of the vortex and radar weighting functions. Thus the maximum velocity difference is obtained. If the tornado is located toward the center of the radar beam or the boundaries of a range gate, the velocity difference decreases. For example, if a small tornado is located at the center of the resolution volume, the mean Doppler velocity is ideally zero because of the symmetry of the spectrum. Additionally, the magnitude of the mean Doppler velocity from either of the adjacent volumes centered at -1 ^{o} or 1 ^{o} should be relatively small due to the range dependence of the vortex velocities from a small tornado. For a relatively large tornado ($r_t = 200$ m), velocity difference larger than 20 m s^{-1} is observed for all 121 tornado's locations at the normalized distance of 7. Therefore, a ROD of 100% is obtained as shown in Fig. 4.10.

In contrast, the region of positive NFTDA-SL detections is denoted by white lines with a ROD of 73.5% in Fig 4.11. One more detection can be provided by NFTDA-SS which show ROD of 74.3%. For the clarity of the figure this addition detection is not shown on the velocity plot (top), but the spectrum and velocity difference and TSS are provided (bottom left). NFTDA-S (NFTDA-SL and NFTDA-SS) misses the

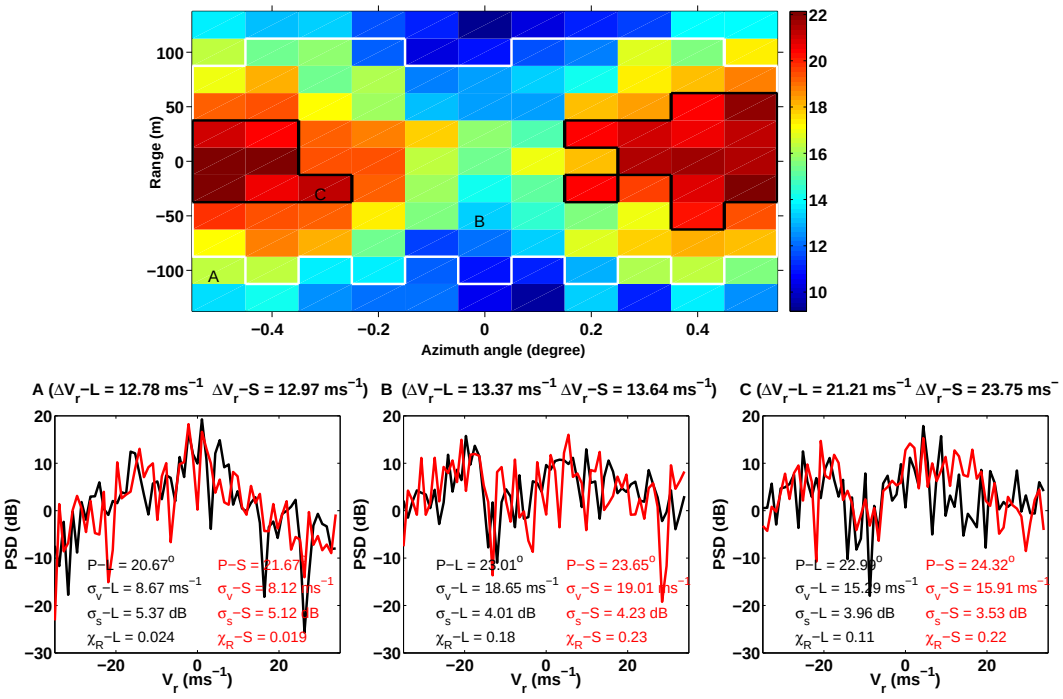

Figure 4.11: A contour plot of the values of velocity difference for 121 tornado locations is shown on the upper panel for $\Delta R/r_t = 5$ and $r_0\theta_b/r_t = 7$. The regions where NFTDA-SL and TTD have positive detections are depicted by white and black lines, respectively. Spectra from three sample locations (A, B, and C) and the five parameters are shown from left to right on the lower panel. The spectra for super-resolution data are indicated by red lines, and for legacy resolution are indicated by black lines. In location A, NFTDA-SL and TTD have miss detections, but NFTDA-SS has accurate detection; in location B, NFTDA-SL and NFTDA-SS have accurate detections but TTD misses; in location C, NFTDA-SL, NFTDA-SS and TTD have good detections

detection when the tornado is located at the boundaries of a radar resolution volume in range. Spectra from the three locations, denoted by A, B and C in the upper panel of Fig. 4.11, are depicted from left to right in the lower panels, respectively. At location A, both NFTDA-SL and TTD miss the detection of the tornado because neither the spectral nor the shear signature is significant enough. However NFTDA-SS can provide one more detection than NFTDA-SL. It is interesting to point out that although the velocity difference at locations A and B is similar and small, the spectrum from location B is wider and more flattened than the one from location A. As a result, prominent spectral features assist the NFTDA-S to produce a positive detection at B while TTD misses. Both NFTDA-S and TTD have positive detections at location C, where the characteristic spectral and shear features are evident.

4.3.4 NFTDA-P

In the section 4.3.2 and section 4.3.3, the performance of NFTDA using Doppler moments and TSS with both legacy and super-resolutions was demonstrated. In this section, the polarimetric neuro-fuzzy tornado detection algorithm with legacy resolution data (NFTDA-PL) was trained using two volumes scans from 10 May 2003 tornado, and tested using five tornado events (8 May 2003, 10 May 2003, 8 May 2007, 8 May 2008 and 19 August 2007). The scales of these tornadoes vary from EF-1 to EF-4, and ranges are between 30 km to 105 km. All the radar data associated with these tornadoes were collected by KOUN. The tornado outbreaks on 8 and 10 May 2003 are of primary interest because continuous polarimetric moments were collected, and damage paths are available for both of them.

The detection results from NFTDA-PL are presented in Fig. 4.12, where results from NFTDA-DL are also included for comparisons. In general, the detections from NFTDA-DL and NFTDA-PL are consistent with the damage path, except that NFTDA-DL produces two false detections at 0341 UTC and 0347 UTC on the

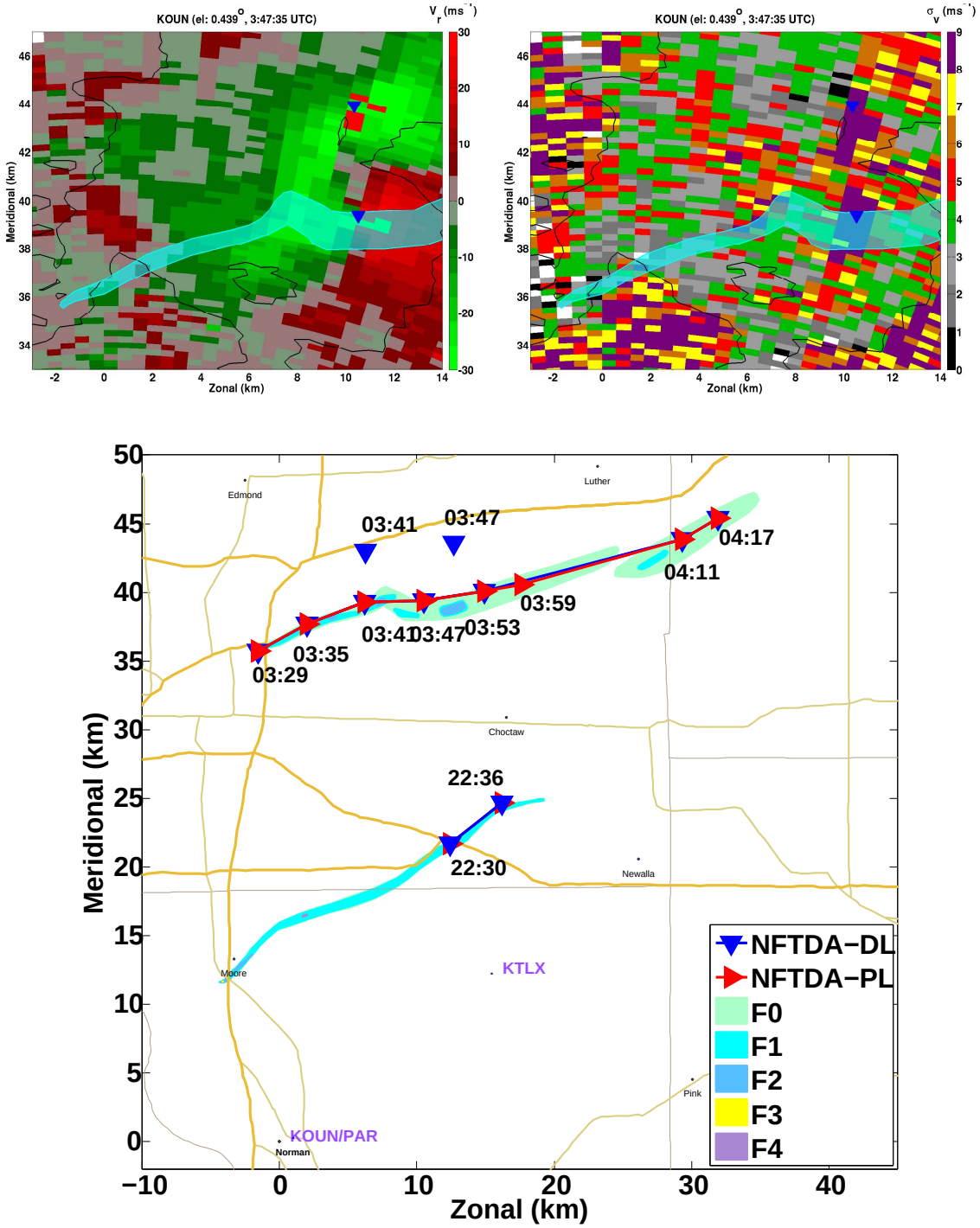

Figure 4.12: The radial velocity (top left) and spectrum width (top right) at 0347 UTC. The contour of reflectivity at 30 dBZ is indicated by black lines on both plots. Ground damage path with Fujita scales is depicted at the bottom of the figure. Comparisons of the detection results from NFTDA-DL and NFTDA-PL (bottom), which are denoted by blue triangles and red triangles, respectively.

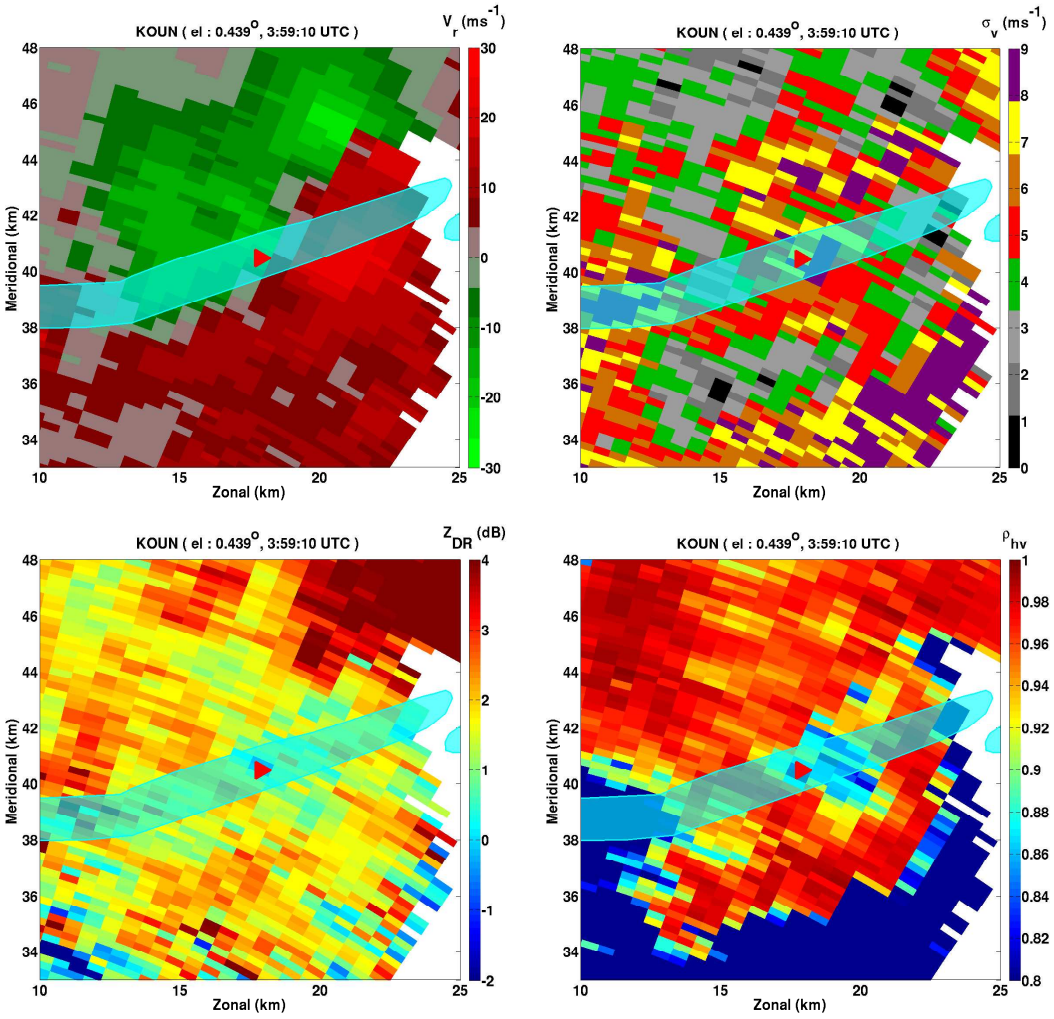

Figure 4.13: The radial velocity (top left), spectrum width (top right), differential reflectivity (bottom left) and cross correlation coefficient (bottom right) at 0359 UTC, respectively. Ground damage path is depicted by transparent contours. The tornado location associated with low Z_{DR} and ρ_{hv} is indicated by a red triangle

	$W_{\Delta V}$	W_{σ_v}	$W_{Z_{DR}}$	$W_{\rho_{hv}}$	W_0
Yes	-0.0010	0.0116	-0.0128	-0.0504	0.1057
No	0.7796	5.736	-0.2582	0.97135	-57.5092
Sensitivity	$\vartheta_{\sigma_v} = 0.72 > \vartheta_{\Delta V} = 0.51 > \vartheta_{\rho_{hv}} = 0.25 > \vartheta_{Z_{DR}} = 0.14$				

Table 4.9: The trained wights and the weight significance sequence of each input parameters in NFTDA-PL.

north side of the damage path. The fields of velocity and spectrum width at 0347 UTC UTC are presented in Fig. 4.12, from where obvious velocity aliasing can be observed. False detections were resulted. However, NFTDA-PL can suppress both false detections because no TDS was observed at the two locations of velocity aliasing. One more detection from NFTDA-PL at 0359 UTC is also within the damage path, which was missed by NFTDA-DL and NFTDA-SL. For this case, apparent TDS but relatively weak velocity difference and spectrum width were observed as shown in Fig. 4.13. Therefore, NFTDA-PL can still successfully detect the tornado while NFTDA-DL misses. Note that if the multiplication was used for the rule inference instead of weighted summation as discussed in section 4.2, the NFTDA-PL would have produced a miss detection as well. This case demonstrates the advantage of using weight summation in the NFTDA-PL. NFTDA-PL has one miss detection at 0405 where no obvious TDS can be observed. The velocity, TDS and TSS fields at this time are provided in Appendix A. For 8 May 2003 tornado case, only data from two volume scans (2230 and 2236 UTC) are available, and the tornado was located 25 km from KOUN. The detections from NFTDA-DL and NFTDA-PL agree with the damage path very well due to the apparent velocity, spectral and polarimetric signatures. Since only limited polarimetric observations of tornadoes are available, no statistical analysis is performed for NFTDA-PL. For the tornado cases on 8 May

Time (UTC)	NFTDA-DL		NFTDA-PL	
	Detection Result	Range (km)	Detection Result	Range (km)
10 May 2003				
0329	hit	35.625	hit	35.625
0335	hit	37.625	hit	37.625
0341	hit false	39.625 43.375	hit	39.625
0347	hit false	40.625 45.125	hit	40.625
0353	hit	42.625	hit	42.625
0359	miss	N/A	hit	48.125
0405	miss	N/A	miss	N/A
0411	hit	52.625	hit	52.625
0417	hit	55.375	hit	55.375
8 May 2003				
2230	hit	24.875	hit	24.875
2236	hit	29.375	hit	29.375
POD	72.7 %		90.9%	
FAR	18.2 %		0%	
CSI	69.2 %		90.9%	

Table 4.10: Comparison of NFTDA-DL and NFTDA-PL for 8 and 10 May 2003 tornadoes. The time index of each volume scan is given in the first column. The detection result and the range of detection are presented for the two methods.

2007, 8 May 2008 and 19 August 2007, only few volume scans data are available. Therefore, no statistical results can be generated.

There is one tornado case (29 May 2004) with time series data from both horizontal and vertical polarization, which allow us to test the performance of NFTDA-P for super-resolution data (NFTDA-PS). However, this tornado is far from the radar (above 90 km), embedded within a mesocyclone and behind high precipitation (HP), which vitiates the tornado's velocity, spectral and polarimetric signatures. Therefore, even both NFTDA-PL and NFTDA-PS can provide detections using this case, there is occasionality inside the results and does not really reflect the true performance and the comparisons between these two. The performance of NFTDA-PL is not statistically analyzed in this study, future works will focus on this.

4.3.5 NFTDA-A

The performance of NFTDA using all the tornado signature parameters (n = 7) with legacy resolution termed as NFTDA-AL is demonstrated using the tornado cases of 8 and 10 May 2003. The membership functions were trained using the the data from two radar volume scans (0341 UTC and 0353 UTC 10 May 2003) at the elevation angles of 0.5^o and 1.5^o. The scoring statistics is provided in Table 4.11, and the comparison among the detection results from NFTDA-DL, NFTDA-PL, NFTDA-SL and NFTDA-AL is presented in Fig. 4.14. Moreover for the clarity purpose, the PODs and FARs of these four methods are shown in Fig. 4.15.

It is apparent, the NFTDA-AL provides the best results with all the hits and no false detections. The miss detection of NFTDA-PL at 0405 UTC can be detected by NFTDA-AL under the assistance of TSS, and the miss detection of NFTDA-SL at 0359 can be detected by NFTDA-AL under the help of TDS. It indicates that the tornado velocity, spectral and debris signatures can work as compensation for each other, and the best performance can be achieved when they are combined together.

Time (UTC)	NFTDA-AL	
	Detection Result	Range (km)
10 May 2003		
0329	hit	35.625
0335	hit	37.625
0341	hit	39.625
0347	hit	40.625
0353	hit	42.625
0359	hit	44.125
0405	hit	48.125
0411	hit	52.625
0417	hit	55.375
8 May 2003		
2230	hit	24.875
2236	hit	29.375
POD	100%	
FAR	0%	
CSI	100%	

Table 4.11: Similar to Table 4.10, but for NFTDA-AL

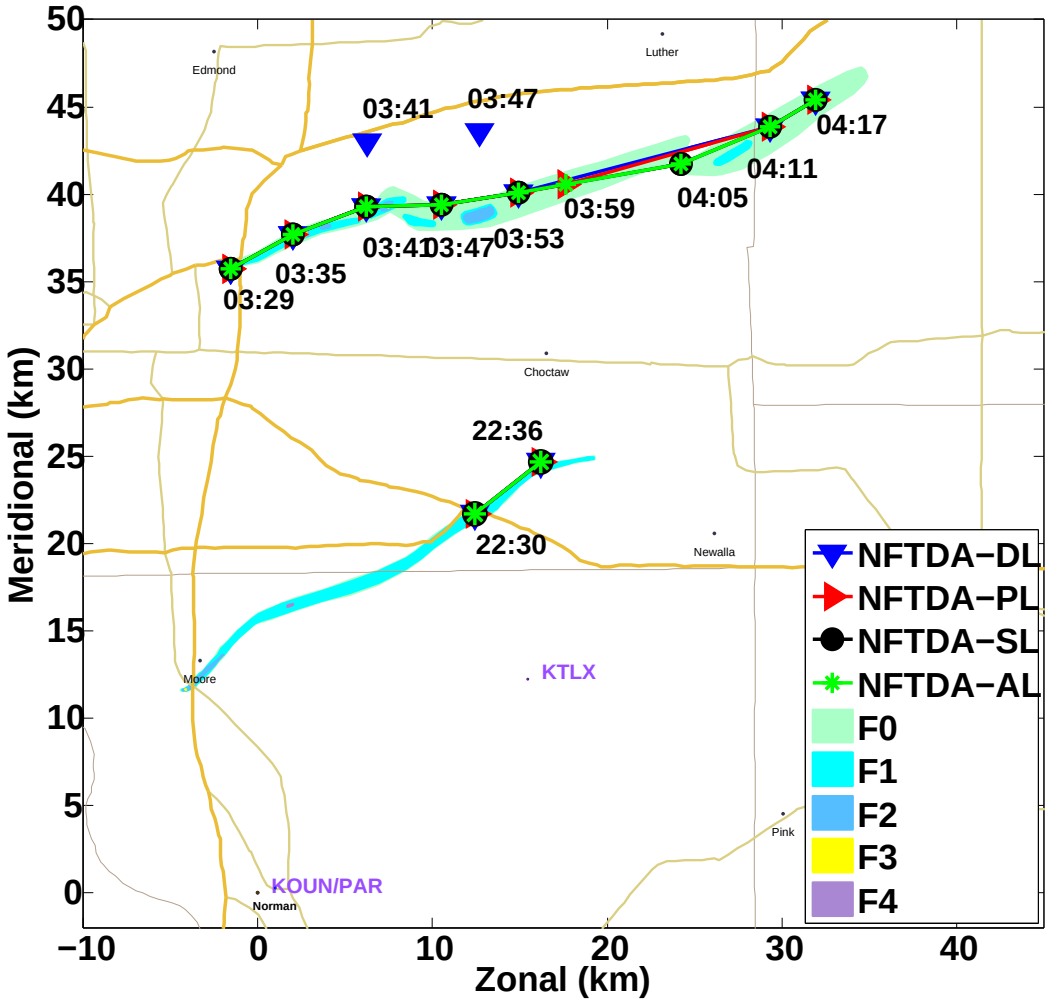

Figure 4.14: Comparisons of the detection results from NFTDA-DL (indicated as blue downward triangles, NFTDA-PL (indicated as red upward triangles), NFTDA-SL (indicated as black dots), and NFTDA-AL (indicated as green stars). The detection of "hit" from each approach is connected by a solid line to show the time continuity. Ground damage paths with Fujita scales are depicted by color-shaded contours.

	$W_{\Delta V}$	W_{σ_v}	W_P	W_{σ_s}	$W_{\chi R}$	$W_{Z_{DR}}$	$W_{\rho_{hv}}$	W_0
Yes	0.0004	-0.021	0.0004	0.0028	0.00291	-0.0039	-0.0087	0.00134
No	-0.0080	0.0996	-0.009	-0.0175	-0.0131	-0.0118	0.01747	2.9890
Sensitivity	$\vartheta_{\sigma_v} > \vartheta_{\Delta V} > \vartheta_{\sigma_s} > \vartheta_{\rho_{hv}} > \vartheta_{Z_{DR}} > \vartheta_P > \vartheta_{\chi R}$							

Table 4.12: The trained wights and the significance sequence of each input parameters in NFTDA-AL.

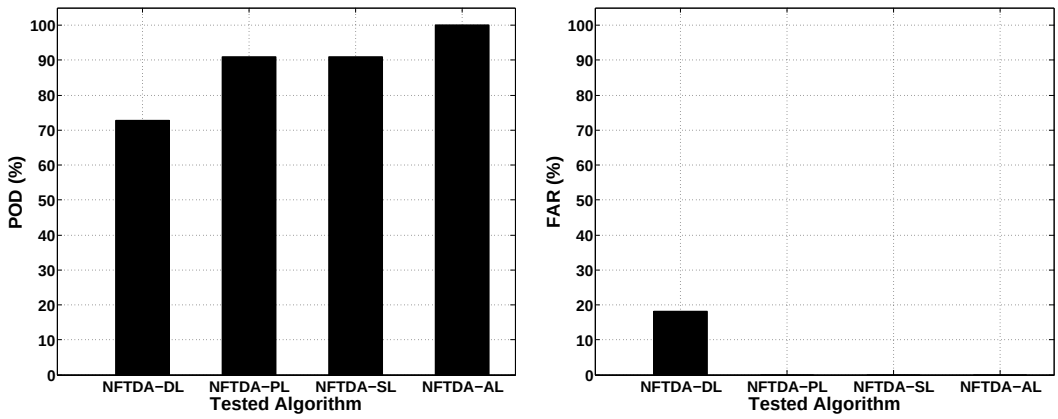

Figure 4.15: The POD (left) and FAR (right) of the NFTDA using different input parameters discussed in this section. The POD and FAR are calculated using the tornado cases on 8 and 10 May 2003.

Note that if the multiplication was used for the rule inference instead of weighted average as discussed in section 4.2, the NFTDA-PL would have produced a miss detection as well. It should be note that the rule inference with weighted summation shows its advantage in this case. When the tornado is not associated with TSS and TDS simultaneously, the rule inference with multiplication would produce miss detection. In this work, since no dual polarization time series data are available for these two cases, so no NFTDA-A for super-resolution data (NFTDA-AL) is performed.

4.4 Summary and Conclusion

It has been shown that strong azimuthal shears can be observed in a tornadic region and are the primary feature for the operational tornado detection algorithm of the WSR-88D. However, the shear signature deteriorates with range because of the smoothing effect by the increasing radar resolution volume. Recently, tornado spectral signatures (TSS) were characterized using spectrum width, bispectrum analysis, and signal statistics. Moreover, large eigen-ratios derived from Level I time series signals were also found to be associated with signals from the vicinity of a tornado. Tornado debris signatures in terms of low differential reflectivity and cross correlation coefficient have been observed in a number of tornadic events. In this work a novel algorithm based on fuzzy logic was developed to integrate spectral, velocity, and debris signatures with the goal of improving tornado detection. A fuzzy logic system is able to launch a decision based on simultaneous inputs with fuzzy descriptions. The system was further enhanced by a training process of a neural network. This hybrid approach is termed Neuro-Fuzzy Tornado Detection Algorithm (NFTDA).

In the dissertation, the architecture of NFTDA was first presented and discussed. The feasibility of NFTDA was tested with different combinations of the input parameters depending on the availability of feature parameters, performance behavior and

the research values. The results indicate that the inclusion of spectral and polarimetric signatures, in addition to shear information, is effective in improving tornado detection. The best performance can be obtained when the velocity, spectral and polarimetric signatures are integrated within the fuzzy logic framework. Moreover, the impact of the super-resolution on the performance is also included in this work. Noticeable improvement from super-resolution data can be obtained if the Doppler moments of radial velocity and spectrum width were used for inputs parameters. In practice, several factors can limit the performance of NFTDA such as the degraded quality of the parameters caused by low SNRs and the fact that the radar actually samples the storms aloft due to the earth curvature.

Chapter 5

Retrieval of the Microphysical Properties for the Mixture of Rain and Hail Using Doppler Spectral Analysis and Genetic Algorithm

5.1 Introduction

In previous three chapters, the application of Doppler spectra and neuro-fuzzy to tornado detection has been studied systematically. In this chapter, spectral analysis and another artificial intelligence approach of GA are combined to retrieve the DSD of both raindrops and melting hailstones, the melting ratio, environmental conditions of ambient wind and turbulence. The mixed-phase precipitation that comprises either rain and hail or graupel and hail are commonly observed below or above the melting level, respectively (Pruppacher and Pitter 1971). This mixture can be frequently observed in convective storms, where water can exist at temperatures below 0^oC and ice can be found at temperature above 0^oC (Balakrishnan and Zrnić 1990). For melting hailstones, their scattering properties become close to pure ice (if the percentage of ice is very high) or pure water (if the percentage of water is high). It was demonstrated that even for the same mixture of rain and hail (same rainrate and hail rate), after the hailstones start to melt, the reflectivity, the differential reflectivity Z_{DR} and the differential propagation constant K_{DP} show different values with different water

percentages in the hailstones (Balakrishnan and Zrnić 1990). Overestimation of hailrate will be generated if the melting is not considered. Therefore, it is valuable to accurately estimate the water fraction of the melting hailstones.

The DSD is one of the most important parameters to be determined in weather radar, since the relation between the received power from precipitation and the rainfall and/or the hailrate are largely affected by the size of drops. Usually, disdrometers are used to measure the natural DSD on surface. Typical error sources for distrometer include undersampling, physical variations, instrument limitations and environmental factors, for example (e.g., Wong and Chidambaram 1985; Ulbrich 1983; Nespor et al. 2000). It was reported that radar retrieved rainfall rate agrees with the rainfall rate derived from disdrometer when the raindrops are smaller than 3 mm (Goddard et al. 1982). Several DSD retrieval methods for radar have been developed in the past 20 years.

The DSDs of both raindrops and melting hailstones and the melting ratio are proposed to be retrieved simultaneously based on the measurements of Doppler spectra and Z_{DR} spectra. In this work, the model of Doppler and polarimetric spectra and the retrieval algorithm are developed for C-band radars. This chapter is organized as follows. An overview of the microphysical properties of raindrops and hailstones is presented in section 5.2. The retrieval of DSD and melting ratio using dual-polarization spectra is developed in section 5.3. The sensitivity analysis and the retrieval procedure are presented in section 5.4 and section 5.5. The retrieval algorithm is evaluated in section 5.6. Finally, the conclusions and future work are given in section 5.7

5.2 Microphysical Properties of Raindrop and Hailstone

5.2.1 The size, shape and orientation

It was shown from observations that smaller raindrops (< 1 mm in diameter) are typically spherical, but larger raindrops (> 1 mm in diameter) normally exhibit the shape of oblate spheroids (Green 1975). The axis ratio (r), representing the ratio between minor to major axis, is related to the equivalent diameters (D) in an equilibrium model (Green 1975). A polynomial function which describes the relationship between the D and r was developed by Zhang et al. (2001a), it is

$$r = 1.0148 - 2.0465\times10^{-2}D - 2.0048\times10^{-2}D^2 + 3.095\times10^{-3}D^3 - 1.453\times10^{-4}D^4 \quad (5.1)$$

where D is in millimeters.

The hailstone size has been reported to be as large as 50 mm in diameter (Battan and Theiss 1973). However, most of the hailstones have been observed within the range of 5 - 25 mm (e.g., Matson and Huggins 1980; Mitchell 1996), which is the hailstone size used in this study. The majority of hailstones have been reported with an axis ratio of between 0.6 and 0.8 based on the ground observations (Matson and Huggins 1980; Knight 1982), and the value of 0.75 was used in Jung et al. (2007). In this work, the axis ratio of hailstones is set to be 0.75 and the axis ratio for raindrops is estimated using Eq. (5.1) (Zhang et al. 2001a; Jung et al. 2007). Furthermore, it is assumed that the major axis of a falling particles is aligned in the horizontal direction (Jung et al. 2007).

5.2.2 The terminal velocity

The terminal velocity of raindrop used in this work is provided in the following equation (Atlas et al. 1973).

$$v_t(D) = \left(\frac{\rho_0}{\rho}\right)^{0.4} [9.65 - 10.3\exp(-0.6D)] \tag{5.2}$$

where ρ_0 and ρ are the air densities at the sea level and the altitude of interest, respectively.

The terminal velocity of hailstones derived by Mitchell (1996) is as follows.

$$v_t(D) = 1.086 \left(\frac{2\alpha g}{\rho\xi}\right)^{0.5} D^{0.5(\beta+2-\sigma)-1} \tag{5.3}$$

where g is the gravitational constant. The value of α, β, ξ and σ are suggested as 0.466, 3.0, 0.625 and 2.0, respectively (Matson and Huggins 1980). In the work of Matson and Huggins (1980), 621 hailstone samples from summer seasons in Wyoming, Nebraska and Colorado were used to evaluate the relationship between hailstones' terminal velocities and sizes and Eq. (5.3) is the best fitting result. The comparison between the terminal velocities between raindrops and hailstones is presented in Fig. 5.1, where the diameter of raindrops is from 0.08 to 8 mm, and diameter of hailstones is from 5 to 25 mm. It is clear that the terminal velocity of hailstone is larger than the raindrop for D >10 mm. Additionally, smaller hailstones can have the same terminal velocity as those from larger raindrops. In other words, the contribution of raindrops and hailstones to the Doppler spectrum cannot be distinguished in the region where their velocities overlap. The radial velocity observed by a weather radar with elevation angle of γ can be written as follows.

$$v(D) = V_t(D) \times \sin(\gamma) + v_0 \tag{5.4}$$

where v_t is particle's terminal velocity and v_0 is the ambient air radial velocity (m s^{-1}).

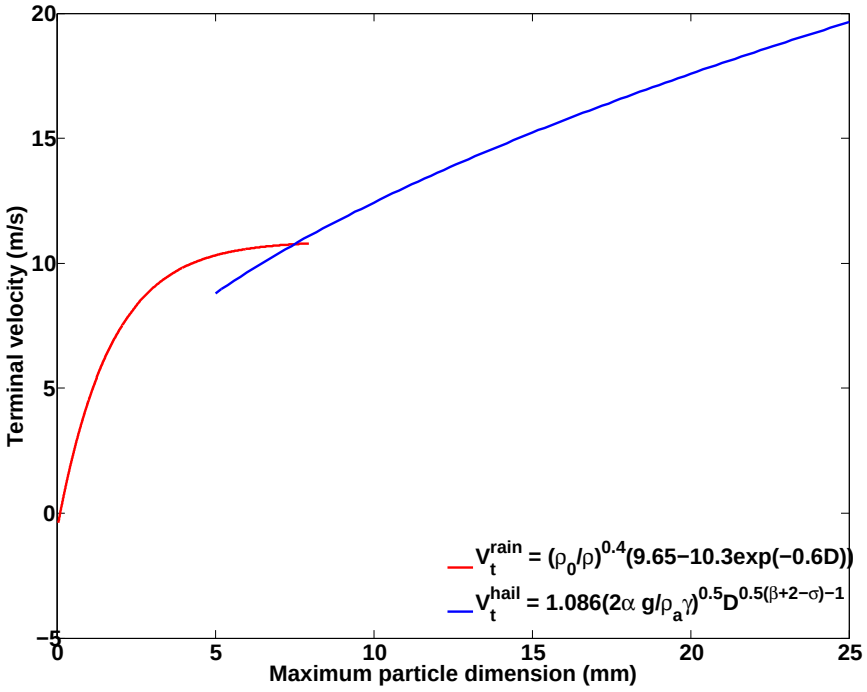

Figure 5.1: Comparison of the terminal velocities of raindrops and hailstones. The red line represents the terminal velocity from raindrops and blue line represents the terminal velocity from hailstones. The X-axis is equivalent diameters D, and Y-axis is the terminal velocity.

5.2.3 The drop size distribution (DSD)

Based on earlier observations (e.g., Marshall and Palmer 1948; Law and Parson 1943), the exponential DSD was derived in the following equation.

$$N(D) = N_w \exp(-\Lambda D) \tag{5.5}$$

Ulbrich (1983) suggested the use of the Gamma distribution for representing raindrop DSD.

$$N(D) = N_w D^{\mu} \exp(-\Lambda D) \tag{5.6}$$

The Gamma DSD with three parameters (N_w, μ and Λ) is capable of describing a broader variation in rain DSD than an exponential distribution. It should be noted that the exponential distribution is a special case of Gamma distribution with $\mu = 0$. More accurate and complicated expression of Gamma distribution was suggested by Bringi and Chandrasekar (2001) as:

$$N(D) = N_w \frac{6}{3.67^4} \frac{(3.67+\mu)^{\mu+4}}{\Gamma(\mu+4)} (\frac{D}{D_0})^{\mu} \exp[-(3.67+\mu)\frac{D}{D_0}] \tag{5.7}$$

where N_w, D_0 and μ are the intercept parameter of the distribution, median volume diameter of a raindrop, and the shape parameter, respectively. Note that for hailstones, the exponential DSD of Eq. (5.5) is often used (e.g., Cheng and English 1983; Balakrishnan and Zrnić 1990; Spek et al. 2007), where Λ and D are in mm^{-1} and mm, respectively.

5.2.4 Melting process of hailstone

The melting process of ice particles is closely related to the latent heat transfer and the redistribution of liquid water in cloud, and have been studies in plentiful work (e.g., Rasmussen et al. 1984a,b; Rasmussen and Heymsfield 1987). It was reported that smaller size hailstone can carry more water on surface to reach its equilibrium mass, but for larger size hailstone, this water fraction becomes smaller (Rasmussen

et al. 1984b; Rasmussen and Heymsfield 1987). If the water on the surface of a melting hailstone excesses the the equilibrium mass, shedding will occur. As a result, the mass of water-coated hailstone decreases and consequently the terminal velocity will decrease. In this work, the shedding process is not considered for the simplification purpose. In other words, if the water on the surface of a hailstone reaches its equilibrium mass, the melting process stops and the melting ratio reaches its maximum value. The melting ratio (f_w) of hailstones is defined by Rasmussen et al. (1984b); Jung et al. (2007) as presented in the following equation.

$$f_w = \frac{m_w}{m_w + m_i} \tag{5.8}$$

where the m_w is the mass of the melted water on the surface of the hailstones, and m_i are the mass of the ice core. Moreover, no shedding occurs if the equivalent diameter of the melting hailstone is less than 9 mm, which means the f_w of small size hailstone (< 9 mm) can be up to 100% (Rasmussen et al. 1984b). The water mass growth rate for small (5 mm $< D <$ 9 mm) and large (9 mm $< D <$ 25 mm) hailstones suggested by Rasmussen et al. (1984b) are

$$\frac{dm_w}{dt} = -\frac{4\pi a_d}{L_m}[\bar{f}_h k_a(T_\infty - T_0) + \bar{f}_v L_e D_v(\rho_{v,\infty} - \rho_{v,0})] \quad (5\text{mm} \leq D < 9\text{mm}) \tag{5.9}$$

$$\frac{dm_w}{dt} = -\frac{\chi A N_{Re}^{1/2}}{2a_d L_m}[N_{Pr}^{1/3} k_a(T_\infty - T_0) + N_{Sc}^{1/3} L_e D_v(\rho_{v,\infty} - \rho_{v,0})] \quad (9\text{mm} \leq D \leq 25\text{mm}) \tag{5.10}$$

$$\bar{f}_h = (0.78 + 0.308 N_{Pr}^{1/3} N_{Re}^{1/2}) \tag{5.11}$$

$$\bar{f}_v = (0.78 + 0.308 N_{Sc}^{1/3} N_{Re}^{1/2}) \tag{5.12}$$

where a_d is the overall radius of particle, and a_i is the radius of ice core, L_m is the latent heat of melting, k_a is the thermal conductivity of air, T_∞ is the temperature

(K) in the environment far from particle's surface, T_0 is the constant equal to 273.16 K, L_e is the latent heat of evaporation, D_v is the diffusivity of water vapor in air, $\rho_{v,\infty}$ is the water vapor density at temperature T_∞, $\rho_{v,0}$ is the water vapor density at temperature T_0, A is the surface area of the ice spheroid, and χ a heat transfer coefficient experimentally determined by Macklin as a function of the axis ratio of the spheroid, and $\chi = 0.76$ as suggested by Rasmussen et al. (1984b) for the entire melting period. Moreover, the Schmidt number is defined by $N_{Sc} = \nu/D_v$, where ν is the kinematic viscosity of air; the Prandtl number is defined by $N_{Pr} = \nu/\kappa_a$, where κ_a is the thermal diffusivity of air; the Reynolds number is defined by $N_{Re} = 2a_i U_\infty/\nu$, where a_i is the semi-major axis of the melting particles, U_∞ is the terminal velocity of the particle.

From Eq. (5.9) and Eq. (5.10), the melting ratio for different sizes of hailstones can be derived if the melting ratio of the smallest size is known. It is assumed that all the hailstones start to melt at the same moment and the mass of hailstones is conserved during the melting process (i.e., no shedding, collision and condensation are considered). The mass of the hailstone with the smallest diameter of 5 mm is denoted by m_t^{5mm} at initial time. Assuming after t seconds, the water mass on the melting hail is m_w^{5mm}. The melting ratio of the smallest hail at time t can be calculated using the following equation.

$$f_w^{5\text{mm}} = \frac{m_w^{5\text{mm}}}{m_t^{5\text{mm}}} \tag{5.13}$$

The water mass growth rate can be approximated by the following equation if the period t is not too large.

$$R_m^{5\text{mm}} = m_w^{5\text{mm}}/t. \tag{5.14}$$

where $R_m^{5\text{mm}}$ is the estimated water mass growth rate. From Eq. (5.9) and Eq. (5.10), it is apparent that water mass growth rate is a function of the hailstone's size (mass), therefore the water growth rate and the water mass for other sizes of hailstones can

be calculated as $m_w = R_m t$. Furthermore, the melting ratio of other sizes hailstones can be estimated using Eq. (5.14).

Given the melting ratio of the smallest hailstone with diameter of 5 mm ($f_w^{5\text{mm}}$), the distribution of melting ratio as a function of the hailstones size is presented in Fig. 5.2. For small particles (with size less than 9 mm), the melting ratio can be as high as 100%. In other words, it can melt into raindrop. However, for large drop with diameter of 20 mm for example, the maximum melting ratio is below 20%. This result is consistent with the early observations by Rasmussen et al. (1984b). Note hereafter the melting ratio is used to represent the melting ratio of the smallest hailstone ($F_w = f_w^{5\text{mm}}$), if not specified.

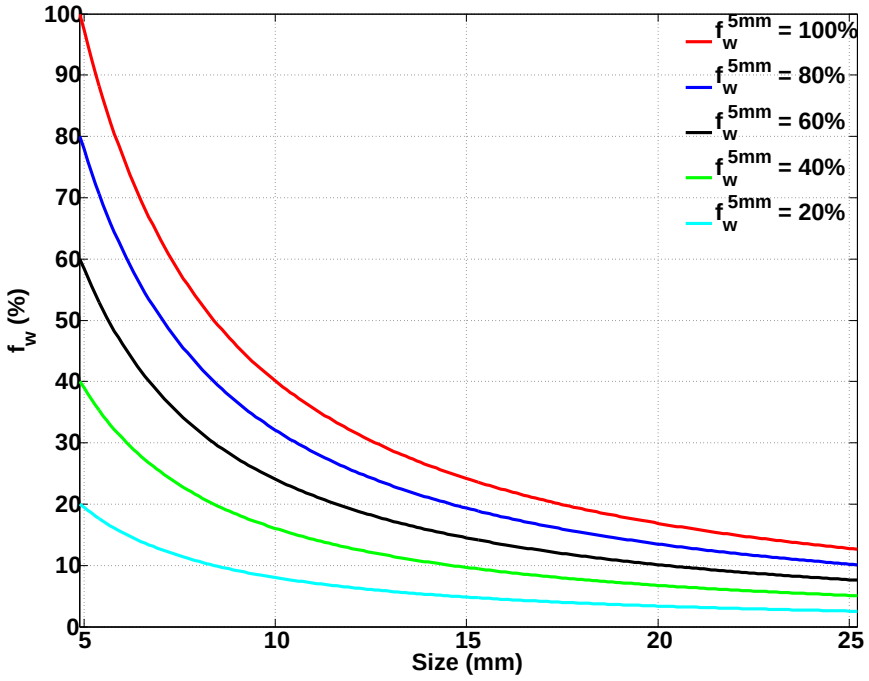

Figure 5.2: The melting ratio of hailstone as function of hailstones' size. The melting ratio of the smallest hailstone with diameter of 5 mm f_w^{mm} is given and the melting ratio of other size can be estimated. The X axis is the equivalent diameter of hailstone, and Y axis is melting ratio (f_w). Different color lines indicate different melting ratios of the smallest hail.

5.2.5 Canting angle of raindrop and hailstone

The canting of hydrometeor can be caused by different sources such as ambient wind and turbulence (Spek et al. 2007). The backscattering matrix for an arbitrarily canted Rayleigh scatterer can be expressed as a function of the principal scattering amplitude (f_a, f_b) (Zhang et al. 2001a):

$$\begin{aligned}\begin{bmatrix} f_{hh} & f_{hv} \\ f_{vh} & f_{vv} \end{bmatrix} &= \begin{bmatrix} \cos\phi & -\sin\phi \\ -\sin\phi & \cos\phi \end{bmatrix} \begin{bmatrix} f'_h & 0 \\ 0 & f'_v \end{bmatrix} \begin{bmatrix} \cos\phi & \sin\phi \\ -\sin\phi & \cos\phi \end{bmatrix} \\ &= \begin{bmatrix} Af_a + Bf_b & (f_a - f_b)\sqrt{BC} \\ (f_a - f_b)\sqrt{BC} & Cf_b + Df_a \end{bmatrix}\end{aligned} \tag{5.15}$$

where

$$\begin{aligned} A &= \cos^2\phi + \sin^2\gamma\sin^2\phi \\ B &= \cos^2\gamma\sin^2\phi \\ C &= \cos^2\gamma\cos^2\phi \\ D &= \sin^2\phi + \sin^2\gamma\cos^2\phi \end{aligned} \tag{5.16}$$

and ϕ and γ are canting angle components in polarization and transverse, respectively. Note that γ can be viewed as the elevation angle of an incident wave (Zhang et al. 2001a). The f_a and f_b are the scattering amplitude at horizontal and vertical direction of raindrop and hailstone. In this work, the f_a and f_b are calculated using the T-matrix method following Zhang et al. (2001a). Although Eq. (5.15) was derived for Rayleigh scatterers, the canting angle distribution is assumed to be independent of the hydrometeor size or shape (e.g., Holt 1984; Metcalf 1988; Balakrishnan and Zrnic 1990). The scattering matrix for large hailstones, which are in Mie region are also calculated using Eq. (5.15). The same assumption was also made in Balakrishnan and Zrnic (1990).

The backscattering cross section can be estimated using the following equations (Zhang et al. 2001a; Jung et al. 2007):

$$\begin{aligned} \sigma_{hh} &= 4\pi < |F_{hh}|^2 > \\ &= 4\pi(\bar{A^2}|f_a|^2 + \bar{B^2}|f_b|^2 + 2\bar{AB}|f_a||f_b|) \end{aligned} \tag{5.17}$$

$$\begin{aligned} \sigma_{vv} &= 4\pi < |F_{vv}|^2 > \\ &= 4\pi(\bar{D^2}|f_a|^2 + \bar{C^2}|f_b|^2 + 2\bar{CD}|f_a||f_b|) \end{aligned} \tag{5.18}$$

where:

$$\bar{A^2} = < (\cos^2\phi + \sin^2\gamma\sin^2\phi)^2 > = A_0 + \sin^4\gamma B_0 + 2\sin^2\gamma C_0 \tag{5.19}$$

$$\bar{B^2} = < (\cos^2\gamma\sin^2\phi)^2 > = \cos^4\gamma B_0 \tag{5.20}$$

$$\bar{C^2} = < (\cos^2\gamma\cos^2\phi)^2 > = \cos^4\gamma A_0 \tag{5.21}$$

$$\bar{D^2} = < (\sin^2\phi + \sin^2\gamma\cos^2\phi)^2 > = B_0 + \sin^4\gamma A_0 + 2\sin^2\gamma C_0 \tag{5.22}$$

where

$$A_0 = < \cos^4\phi > = \frac{1}{8}(3 + 4\cos 2\bar{\phi}e^{-2\sigma^2} + \cos 4\bar{\phi}e^{-8\sigma^2}) \tag{5.23}$$

$$B_0 = < \sin^4\phi > = \frac{1}{8}(3 - 4\cos 2\bar{\phi}e^{-2\sigma^2} + \cos 4\bar{\phi}e^{-8\sigma^2}) \tag{5.24}$$

$$C_0 = < \sin^2\phi\cos^2\phi > = \frac{1}{8}(1 - \cos 4\bar{\phi}e^{-8\sigma^2}) \tag{5.25}$$

And the $\bar{\phi}$ and σ are the mean and standard deviation (SD) of the canting angles. In this work the mean and standard deviation of the canting angle for raindrop are 0^o, which was suggested based on observations (Hendry and McCormick 1976), and further implemented by Jung et al. (2007). For hailstones, the mean of canting angle is also assumed to be 0^o, but the SD is a function of the melting ratio as $\sigma = 60^o(1-cf_w)$, where c is a coefficient of 0.8 (Jung et al. 2007).

5.3 Retrieval of Drop Size Distribution and Melting Ratio Using Dual-polarimetric Spectra

Assume that there is no spectral broadening, the Doppler spectrum, $S_{hh}(v)dv$ for the horizontal polarization and $S_{vv}(v)dv$ for the vertical polarization and the differential reflectivity spectrum $Z_{DR}(v)dv$ can be written as (Doviak and Zrnić 1993; Moisseev et al. 2006; Spek et al. 2007):

$$S_{hh}(v)dv = \frac{\lambda^4}{\pi^5|k_w|^2} N[D(v)]\sigma_{hh}[D(v)]\frac{dD(v)}{dv}dv \qquad (\mathrm{mm^6 m^{-3}}) \tag{5.26}$$

$$S_{vv}(v)dv = \frac{\lambda^4}{\pi^5|k_w|^2} N[D(v)]\sigma_{vv}[D(v)]\frac{dD(v)}{dv}dv \qquad (\mathrm{mm^6 m^{-3}}) \tag{5.27}$$

$$Z_{DR}(v)dv = \frac{S_{hh}(v)}{S_{vv}(v)}dv \tag{5.28}$$

where the dielectric factor $k_w = (\epsilon_r - 1)/(\epsilon_r + 2)$, ϵ_r is the complex dielectric constant calculated using the Maxwell-Garnett mixing formula (Maxwell-Garnett 1904), $N[D(v)]$ is the DSD ($\#\ \mathrm{m^{-3}mm^{-1}}$). It is apparent that the Doppler spectrum and differential reflectivity spectrum are determined by $N(D)$ and the backscattering cross section of σ_{hh} and σ_{vv}, where D can be determined from the radial component of the terminal velocity if the elevation angle is sufficiently high. Moreover, the σ_{hh} and σ_{vv} can be calculated using the backscattering amplitude f_a and f_b. An example of backscattering amplitudes of raindrops (D from 0.08 mm to 8 mm with step of 0.08 mm) at C-band was calculated using the T-matrix method, and is shown as a function of equivolume diameter D in Fig. 5.3. The left and right panels are the real and imaginary values of the backscattering amplitude for polarization along major (f_a) and minor (f_b) axes, respectively. Moreover, the ratio of backscattering cross section of a single rain drop (in dB) from horizontal and vertical polarizations as a function of raindrop size is presented in Fig. 5.4.

If the hailstones start to melt, the hailstones become water coated. Since the relative dielectric constant of water is much higher than ice, $68.2317 + j35.4776$ for water

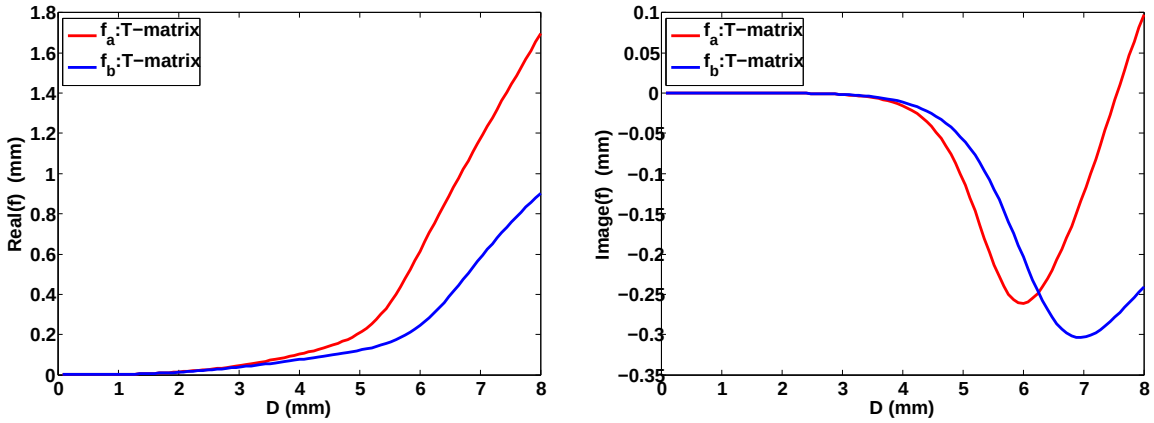

Figure 5.3: Backscattering amplitudes as a function of equivolume diameter for raindrop. Real part for major and minor axis (left), imaginary part for major and minor axis (right).

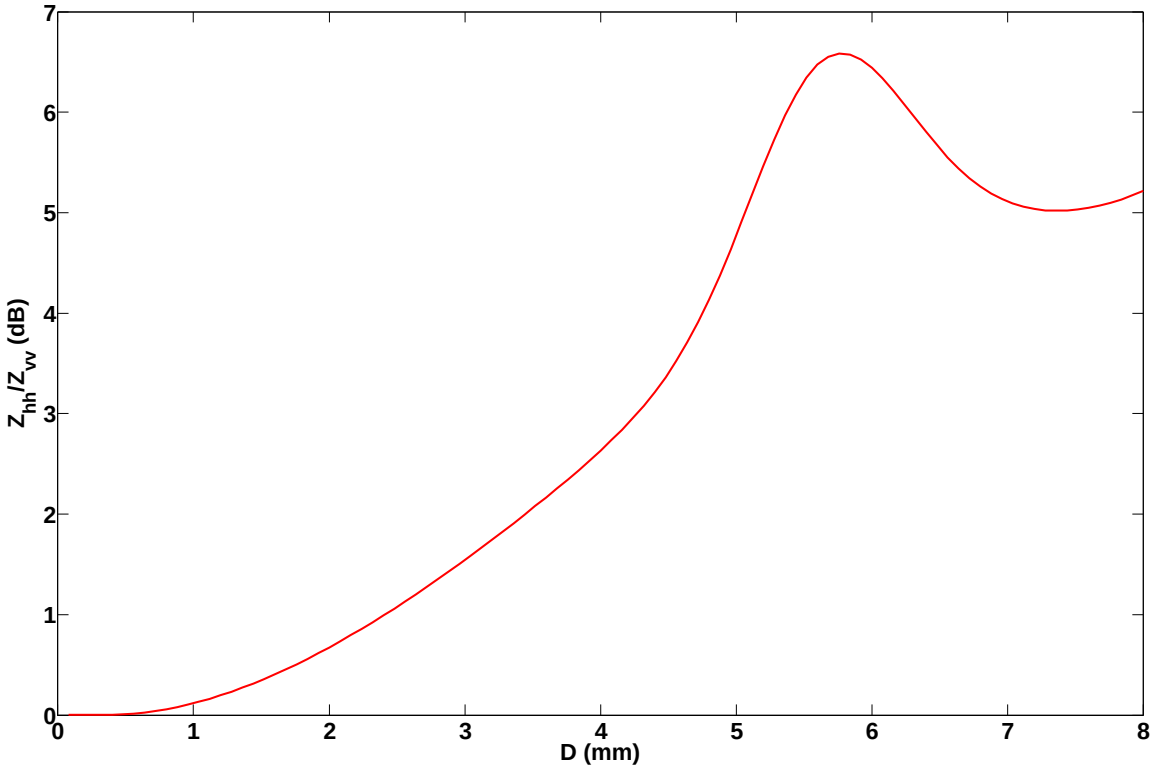

Figure 5.4: Reflectivity at horizontal direction (Z_{hh}) and vertical direction (Z_{vv}) polarizations as a function of raindrop size.

compared to $3.1683 + j0.0006$ for ice at 0^oC for 5 GHz for example, the water on the surface of hailstone will significantly affect the backscattering amplitude and consequently, the Doppler and differential reflectivity spectra. Moreover, a water-coated hailstone can produce different backscattering amplitudes for different melting ratio. Therefore, the melted hailstone's backscattering amplitude connects the melting ratio and spectra together, and makes the retrieval of melting ratio using Doppler and Z_{DR} spectrum possible.

In this work, the backscattering amplitude of melted hailstones (f_a and f_b) with diameter from 5 mm to 25 mm (with step of 0.7 mm) and with f_w from 0% to 100% (with setp of 5%) are pre-calculatied at C-band using the T-matrix method (Zhang et al. 2001a; Jung et al. 2007). The real and image parts of backscattering amplitude from smallest (5 mm) and largest (25 mm) hailstone as a function of melting ratio f_w are exemplified in Fig. 5.5. The one to one relationship between the f_w and the $f_a(f_b)$ is needed, so that in the retrieval the Doppler and Z_{DR} spectra can be directly expressed as the function of f_w in the following forms.

$$S_{hh}(v)dv = \frac{\lambda^4}{\pi^5 |k_w|^2} N[D(v)] F_{hh}\{f_w[D(v)]\} \frac{dD(v)}{dv} dv \qquad (\mathrm{mm^6 m^{-3}}) \tag{5.29}$$

$$S_{vv}(v)dv = \frac{\lambda^4}{\pi^5 |k_w|^2} N[D(v)] F_{vv}\{f_w[D(v)]\} \frac{dD(v)}{dv} dv \qquad (\mathrm{mm^6 m^{-3}}) \tag{5.30}$$

where $\sigma_{hh}[D(v)] = F_{hh}\{f_w[D(v)]\}$ and $\sigma_{vv}[D(v)] = F_{vv}\{f_w[D(v)]\}$, and F_{hh} and F_{vv} are the functions that used to calculate $\sigma_{hh}[D(v)]$ and $\sigma_{vv}[D(v)]$ from $f_w[D(v)]$. In this work, the 3^{rd}, 5^{th} and 7^{th} order polynomial fitting have been tested and the results are presented in Fig. 5.5 using lines with different colors. For the small particle with equivalent diameter of 5 mm, the fitting results of these three approaches are quite similar. However, for large particle with equivalent diameter of 25 mm (bottom panels), the higher order fitting provides much better results. Although polynomial with order higher than 7^{th} can provide slight improvement, it requires larger computational power. Therefore, the 7^{th} polynomial is selected for this work.

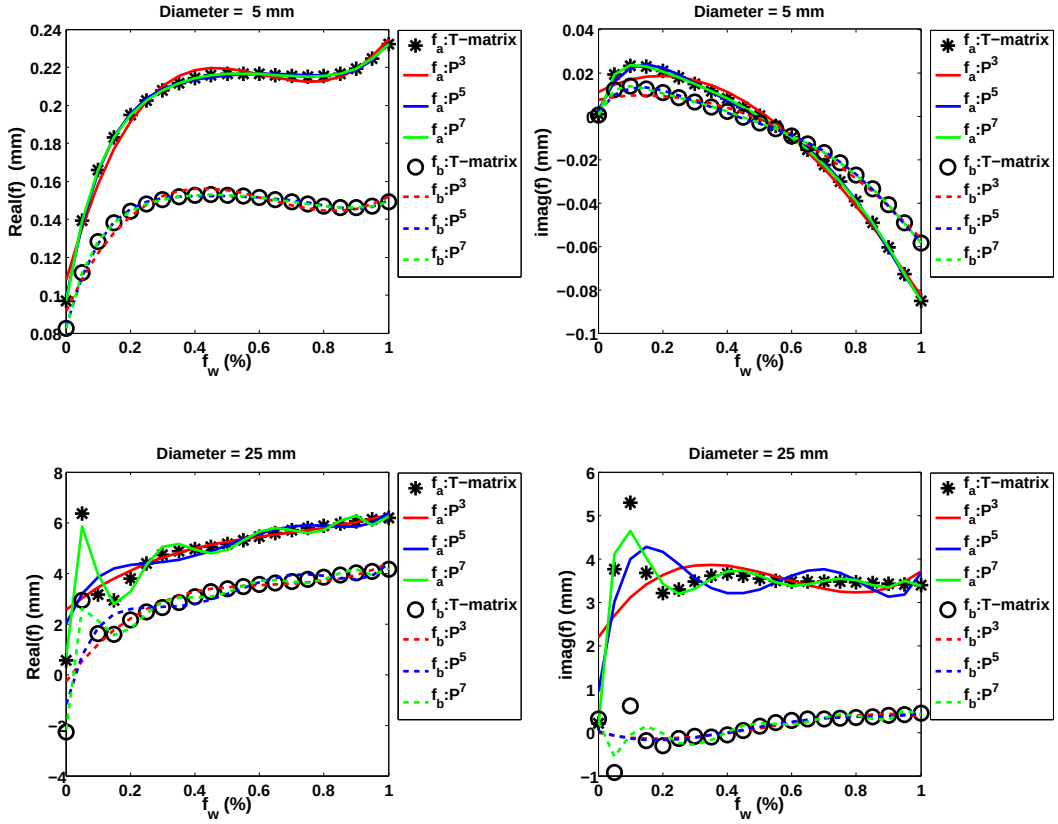

Figure 5.5: Polarimetric backscattering amplitudes (f_a and f_b as a function of equivolume diameter. The results from T-matrix are denoted by asterisks. The polynomial fitting of the T-matrix results is denoted by red, blue and green lines for the 3^{rd}, 5^{th} and 7^{th} order fittings, respectively.

The Doppler and Z_{DR} spectra for the mixture of raindrops and melting hailstones can be written as the combination of pure rain and pure melted hail in the following equations.

$$S_{hh}(v)dv = S^r_{hh}(N^r_w, D_0, \mu)dv + S^h_{hh}(N^h_w, \Lambda, f_w)dv \tag{5.31}$$

$$Z_{DR}(v)dv = \frac{S^r_{hh}(N^r_w, D_0, \mu)dv + S^h_{hh}(N^h_w, \Lambda, f_w)dv}{S^r_{vv}(N^r_w, D_0, \mu)dv + S^h_{vv}(N^h_w, \Lambda, f_w)dv} \tag{5.32}$$

where superscript r and h represent pure rain and melting hail, respectively. It should be noted that the Doppler and Z_{DR} spectra are obtained from sufficiently high elevation angle. Therefore, the separation in spectral components can be obtained from the particles' terminal velocities.

Several factors could produce spectrum broadening such as turbulence, antenna motion, shear and the change in orientation or vibration of hydrometeors (Doviak and Zrnić 1993). It is common to model the effect of spectral broadening as a convolution of the original spectrum from precipitation with a Gaussian kernel (Doviak and Zrnić 1993):

$$S^{mod}_{hh}(v) = S_{broad}(v) * S_{hh}(v) = \frac{1}{\sqrt{2\pi}\sigma_b}\int \exp[-\frac{(v-\bar{v})^2}{2\sigma_b^2}]S_{hh}(\bar{v})d\bar{v} \tag{5.33}$$

where $S^{mod}_{hh}(v)$ is the model spectrum used in the retrieval procedure, the asterisk (*) is the convolution operator, and σ_b is the width of the Gaussian Kernel (m s^{-1}). This broadening could be the summation of independent contributions, that is $\sigma_b^2 = \sigma_s^2 + \sigma_\alpha^2 + \sigma_o^2 + \sigma_t^2$ as discussed in Section 2.2.2.1.

5.4 Sensitivity Analysis

Before the discussion of the retrieval technique, it is necessary to verify that the DSD parameters from both raindrops and hailstones, melting ratio, ambient wind, and spectrum broadening have impacts on the Doppler and differential reflectivity spectra. If the parameter of interest cannot produce noticeable changes, it is not likely to be retrieved correctly and reliably. In this testing, only one parameter is

changed while others are kept constant each time. As a result, we can study the dependence of spectrum on the parameter of interest independently. The effect of ambient wind v_0 on the spectrum is straightforward, which can shift the Doppler spectrum by an amount of v_0 according to Eq. (5.4). In the test, the v_0 is set as 0 and the retrieval of v_0 is discussed in Section 5.5.2. In order to study the impact of each parameter on Doppler spectrum and differential reflectivity spectrum, the analysis of raindrops and melting hails is performed independently. Subsequently, the mixture of both types of hydrometeors are considered. The simulation is designed for C-band radar, and the ambiguous velocity is set at 16 m s^{-1} in this study. Therefore velocity aliasing can be observed if the radial component of the terminal velocities is larger than 16 m s^{-1}.

5.4.1 Contributions from raindrops

From Eq. (5.7), it is clearly shown that the Doppler spectrum from raindrop is determined by four parameters of N_w^r ($m^{-3}mm^{-1}$), D_0 (mm), μ (dimensionless) and σ_b (m s^{-1}). It should be noted that the shedding process is not considered in this work, although it will change the DSD of raindrops and melting hails. The dependence of Doppler and Z_{DR} spectra on these four parameters is demonstrated in Fig. 5.6 and 5.7. In the test, the sign of radial velocity from the terminal velocity is negative (downward motion).

Note that in the plot of Z_{DR} spectra, the spectral components associated with Doppler spectrum below -20 dB are not shown. The following conclusions can be obtained from Fig. 5.6 and 5.7.

1. The N_w^r is set from 5000 to 9000 with the step of 1000. An increase of N_w^r leads to an increase in the amplitude of $S_{hh}(v)$. From $N_w^r = 5000$ to $N_w^r = 9000$, the maximum difference of $S_{hh}(v)$ can be as high as 3 dB when the v is approximately -7 m s^{-1}. Moreover, $Z_{DR}(v)$ keeps the same for different N_w^r,

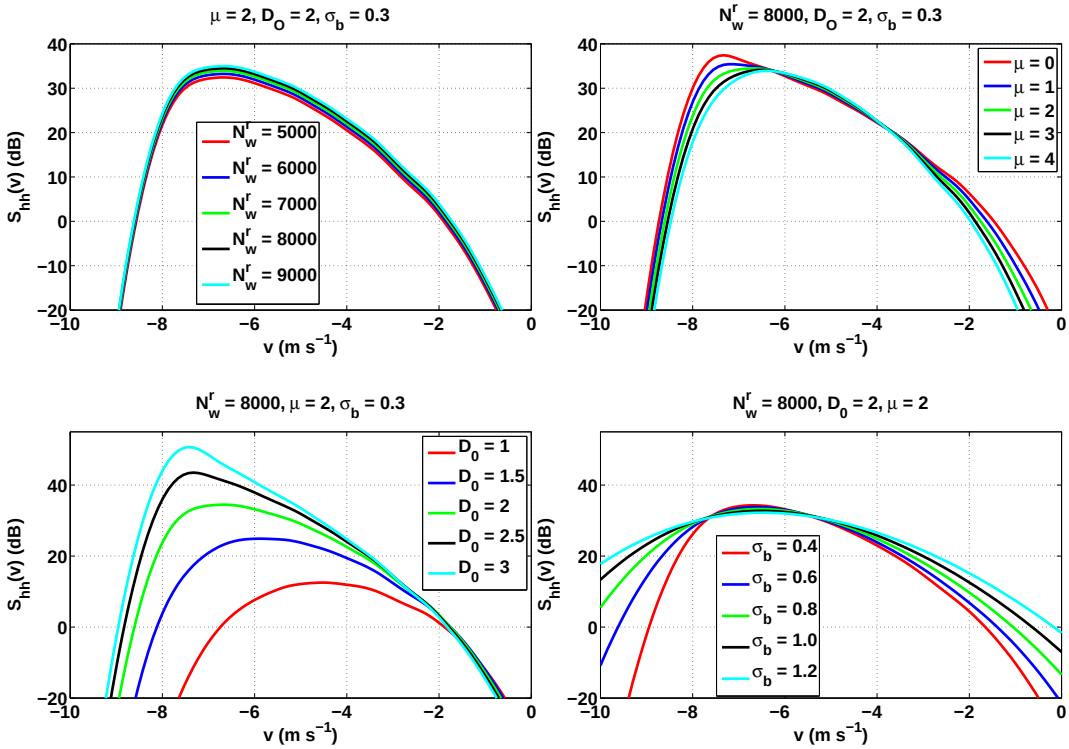

Figure 5.6: Simulated Doppler spectra of rain for hh polarization. The elevation angle is 45^o. The dependence of Doppler spectra on DSD parameters of N_w (top left), μ (top right), D_0 (bottom left) and on spectral broadening σ_b (bottom right), respectively. The X axis is the Doppler velocity (v) in m s^{-1}, and Y axis is the Doppler spectrum from horizontal direction polarization in dB.

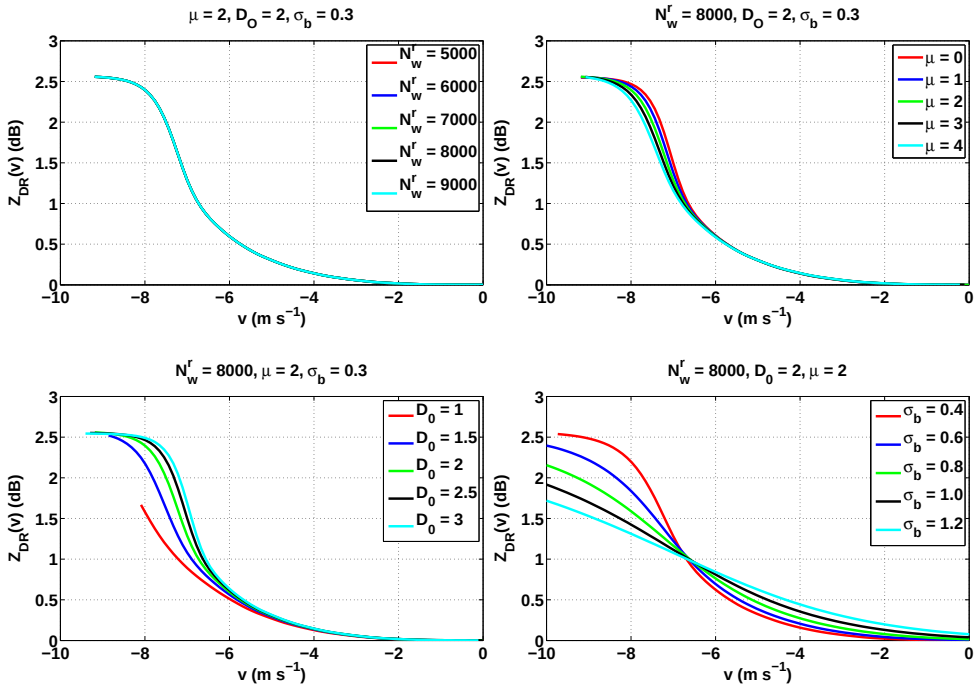

Figure 5.7: Similar to Fig. 5.6, but for Z_{DR}.

which is consistent with the conclusion in Zhang et al. (2001a). It is because the differential reflectivity spectrum is defined by Eq. (5.28), where the N_w^r is canceled. In other words, the Z_{DR} spectrum from pure raindrop is only determined by μ and D_0.

2. The shape parameter μ varies from 0 to 4 with the step of 1. A large difference of approximately 7.5 dB in $S_{hh}(v)$ between $\mu = 0$ and $\mu = 4$ can be observed at approximately -7.6 ms^{-1}. For given N_w^r, D_0 and σ_b, the $Z_{DR}(v)$ of larger drops (v = -8 m s^{-1} for example) decreases with the increasing of μ. For smaller drops (v = -1 m s^{-1} for example) the $Z_{DR}(v)$ is 0 dB as expected. This result is consistent with the results demonstrated byMoisseev et al. (2006). The decrease of μ can be thought of as the increase of the number of large drops. As a result, the magnitude of Doppler spectrum and Z_{DR} spectrum from large drops (high radial velocities due to Doppler sorting) will increase. The maximum

difference of $Z_{DR}(v)$ between $\mu = 0$ and $\mu = 4$ can be around 0.3 dB when v is approximately -7.6 m s^{-1}.

3. The median volume diameter of a raindrop D_0 changes from 1 mm to 3 mm with a step of 0.5 mm. The D_0 has the most significant effect on $S_{hh}(v)$ among the four parameters, which can produce a difference of $S_{hh}(v)$ as high as 40 dB. The increase of D_0 has similar effect to the increase of the number of large drops. As a result, the magnitude of Doppler spectrum and Z_{DR} spectrum from large drops (high radial velocities) will increase. This result is also consistent with the conclusion from the work of Moisseev et al. (2006). Compared to the previous two parameters, D_0 has the most significant impact on both Doppler and Z_{DR} spectra, and is likely to be better retrieved.

4. The spectrum broadening width σ_b varies from 0.4 m s^{-1} to 1.2 m s^{-1} with a 0.2 m s^{-1} step. The σ_b alters the spectrum shape to be wider. Significant broadening effect on the Doppler spectrum and Z_{DR} spectrum can be observed.

Based on the above analysis, it is clear that the D_0 and σ_b have significantly stronger impact on the shape and amplitude of Doppler and Z_{DR} spectra than N_w^r and μ. In other words, one can expect that D_0 and σ_b can be retrieved more accurately compared to N_w^r and μ due to inevitable noise.

5.4.2 Contribution from hailstones

From Eq. (5.5), the exponential DSD of hailstones is defined by N_w^h and Λ. Therefore, four parameters of N_w^h, Λ, f_w, and σ_b determine the Doppler spectrum and differential reflectivity spectrum of melting hailstone. The dependence of the $S_{hh}(v)$ and $Z_{DR}(v)$ on these four parameters is shown in Fig. 5.8 and 5.9. Similar to the case of pure raindrop in Section 5.4.1, the v_0 is set as 0, the terminal velocities are negative, and the following conclusions can be obtained.

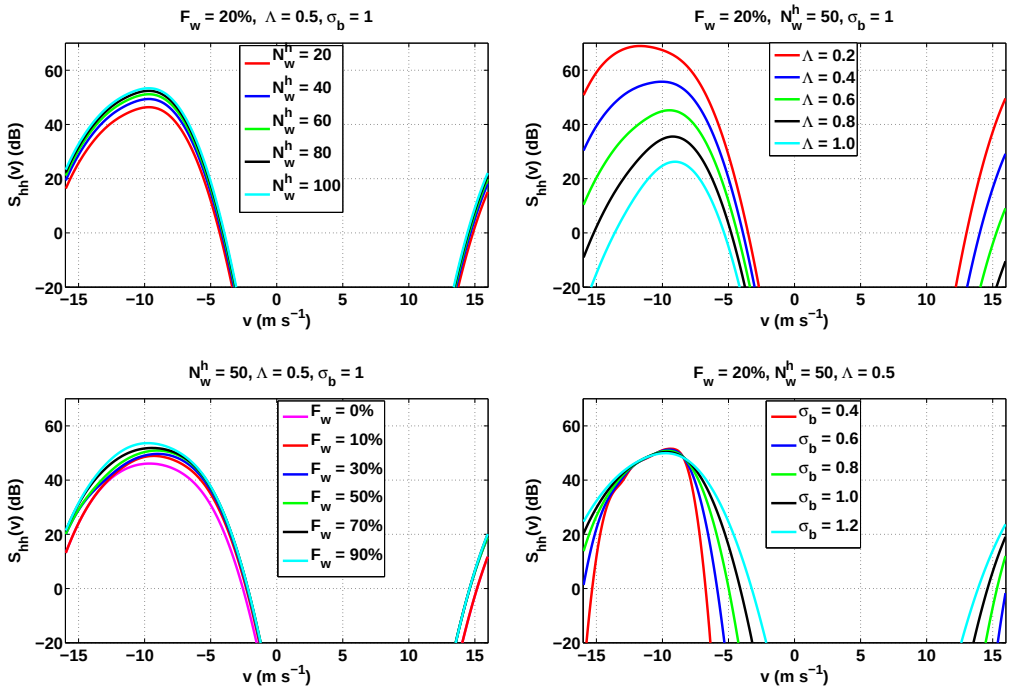

Figure 5.8: Simulated Doppler spectra of hail for hh polarization. The elevation angle is 45^o. The dependence of the Doppler spectrum on DSD parameters of N_w^h (top left), Λ (top right), on spectral broadening σ_b (bottom left), and melting ratio f_w (bottom right), respectively. The X axis is the Doppler velocity in m s^{-1}, and Y axis is the Doppler spectrum from horizontal direction polarization in dB.

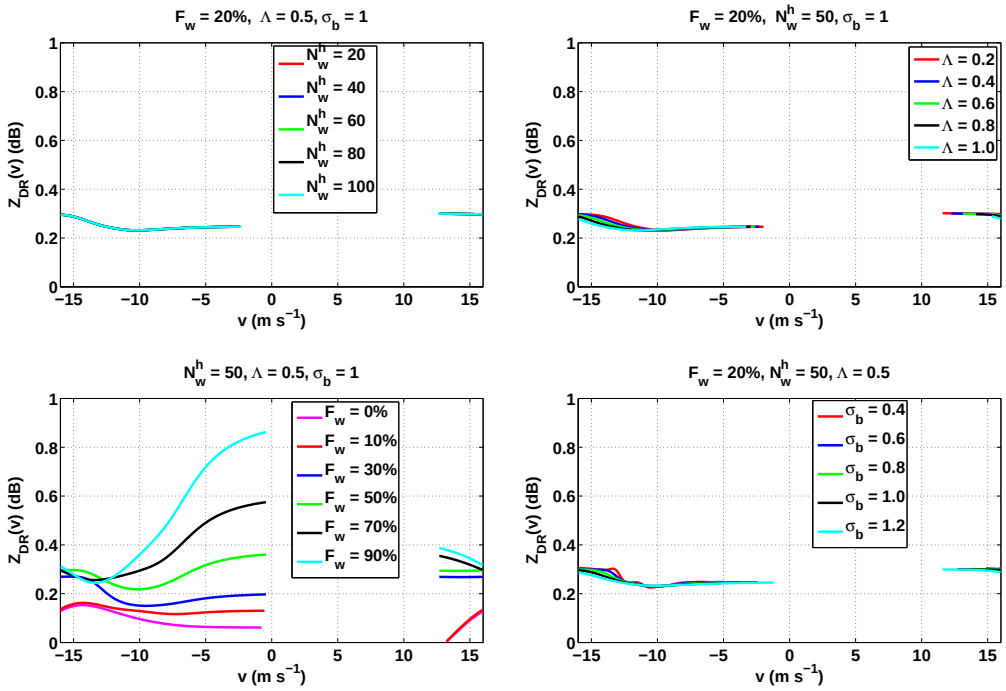

Figure 5.9: Similar to Fig. 5.8, but for Z_{DR}.

1. The Λ is set as 0.5, and N_w^h is set as 20, 40, 60, 80 and 100 which corresponds to hailrate of 3.18 mm/hour to 10.45 mm/hour. With the increasing of N_w^h, the amplitude of $S_{hh}(v)dv$ increases. The maximum difference from $N_w^h = 20$ to $N_w^h = 100$ can be as high as 10 dB. Similar to the raindrops, the $Z_{DR}(v)$ from melting hails is independent of N_w^h.

2. The N_w^h is set as 50, and the Λ is set to 0.2, 0.4, 0.6 0.8 and 1.0 which corresponds to hailrate of 2.79 mm/hour to 44.14 mm/hour. Significant effect of Λ on the $S_{hh}(v)$ can be observed, and the maximum difference can be more than 30 dB. Since the axis ratio for all the hailstones is set to 0.75, the Z_{DR} spectrum is more "flat". In other words, Λ does not have significant effect on Z_{DR} spectrum.

3. The melting ratio of hailstone is set to 0%, 10%, 30%, 50%, 70% and 90%. From 0% to 90%, the maximum spectrum difference can be as high as 15 dB. It

should be noted that when F_w is above 50%, the spectrum does not show much (< 1 dB) difference, therefore the retrieval of F_w can be in error for this case.

4. The spectrum broadening σ_b is set the same as the one for raindrops. The significant broadening of Doppler spectrum can be observed for large σ_b. Unlike the case of pure raindrop, the spectrum broadening for melting hails have limited effect on $Z_{DR}(v)$. It is because the constant axis ratio used in the test.

5.4.3 Contribution from a mixture of raindrops and melting hailstones

From the analysis in the previous two parts, it is clear that N_w^r of pure raindrops has small impact on the Doppler spectrum, and has no impact on the differential reflectivity spectrum. It is speculated that large retrieved errors N_w^r can occur. Furthermore, the amplitude of Doppler spectrum from the hailstones has larger value than the one from raindrops. In other words, the changes in the shape and amplitude of Doppler spectrum and Z_{DR} spectrum can be dominated by the contribution from melting hails. It is important and of interest to study the impacts of D_0 and μ from raindrops and f_w, N_w^h and Λ from hailstones on Doppler and Z_{DR} spectra from a mixture of raindrops and melting hailstones. The impact of σ_b on the mixture spectrum is also included in this section.

The same test used for pure raindrops and melting hailstones is performed, and the results are presented in Fig. 5.10 and 5.11. The conclusions are summarized in the following.

1. D_0 and μ change the low velocity portion (defined by velocity from -8 to 0 m s^{-1}) of the spectrum (from raindrops); and the f_w, N_w^h and Λ only change the high velocity portion (defined by velocity from -16 to -8 m s^{-1}) of the spectrum (from hailstones).

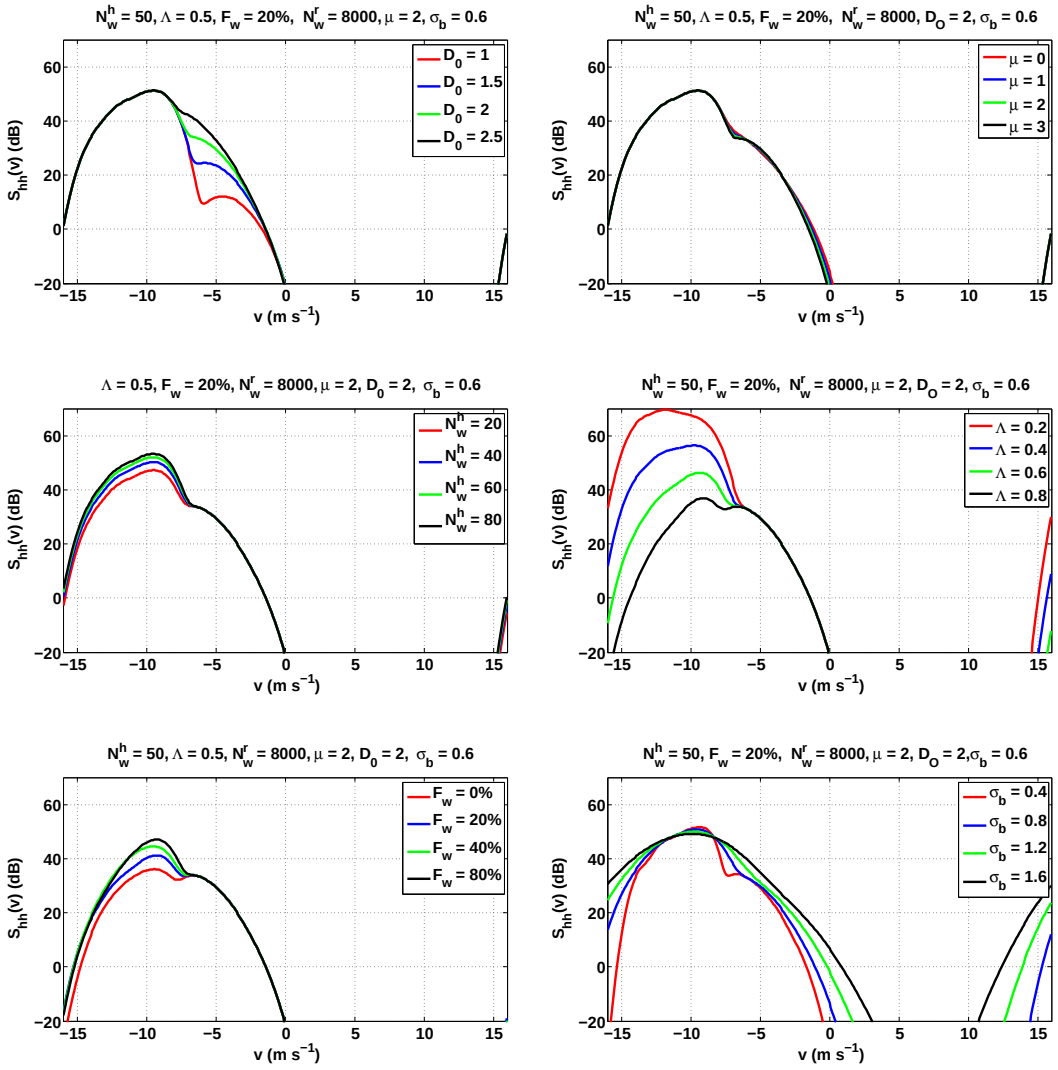

Figure 5.10: Simulated Doppler spectra from a mixture of hailstones and raindrops. The elevation angle is 45^o. The dependence of the spectral density on DSD parameters of raindrops of D_o (top left) and μ (top right); N_w^h (middle left) and Λ (middle right); and melting ratio f_w (bottom left), and spectral broadening σ_b (bottom right), The X axis is the Doppler velocity in m s^{-1}, and Y axis is the Doppler spectrum from horizontal direction polarization in dB.

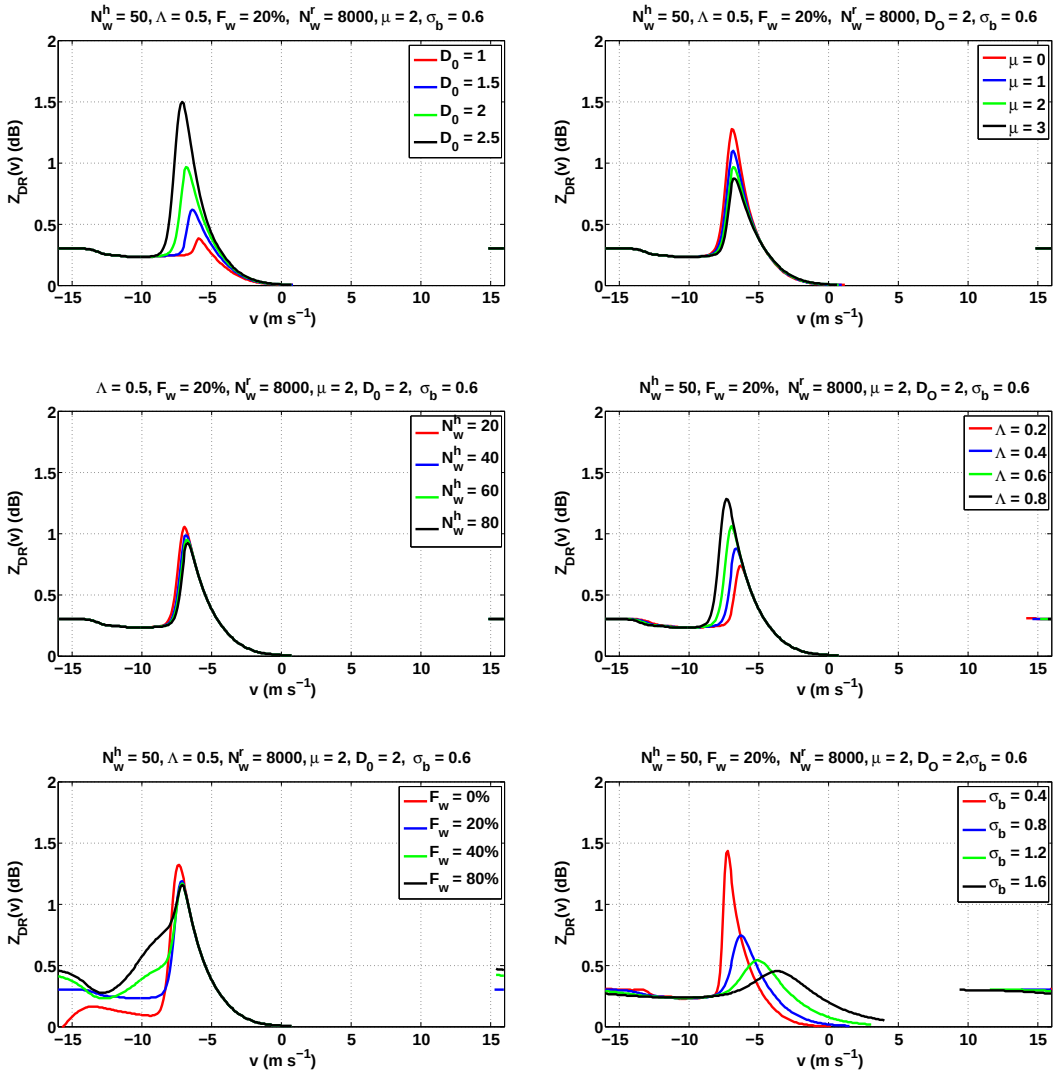

Figure 5.11: Similar to Fig. 5.10 but for $Z_{DR}(v)$.

2. The Λ has the most significant impact on Doppler spectrum.

3. Spectrum broadening σ_b smoothen the spectrum from both raindrops and hailstones. The Doppler spectrum with double-peak feature (one from raindrops and the other is from hailstones) can only be observed for smaller σ_b of 0.4 m s^{-1}.

In this section, the dependence of Doppler spectrum and Z_{DR} spectrum on the DSD, melting ratio and spectrum broadening was investigated. It is obvious that D_0, Λ, N_w^h, f_w and σ_b have significant impact on the shape and amplitude of the Doppler spectrum, and D_0, f_w and σ_b have obvious impact on the Z_{DR} spectrum. Those five parameters are likely to be retrieved more accurately. On the other hand, N_w^r and μ have small impact on Doppler spectra, and N_w^r does not affect the Z_{DR} spectrum, therefore can not be retrieved as accurate as previous five parameters.

5.4.4 Impact of elevation angles

The impact of the elevation angles on Doppler spectrum and differential reflectivity spectrum is examined now. The $S_{hh}(v)$ and $Z_{DR}(v)$ from elevation angles of 10^o, 45^o, 75^o and 90^o are presented in Fig. 5.12 and 5.13. From Eq. (5.4), it is clear that with the decrease of elevation angle γ, the contribution of the terminal velocity to radial velocity becomes smaller. For $\gamma = 0^o$, the radial velocity from the terminal velocity of all the precipitations are all zeros. In other words, no Doppler sorting of hydrometeors is occurred, although the differential reflectivity from large hydrometeors are maximized. On the other hand, for $\gamma = 90^o$, the Doppler sorting capability of the falling velocities is maximized. In other words, hydrometeors with different size can be separated in Doppler spectrum. This is manifested by the increase of spectrum components as increasing elevation angle. However, the benefit of polarimetric measurements is compromised.

Furthermore, the influence of raindrop shapes on the Z_{DR} spectrum measurements is larger for smaller elevation, which can be observed on the top left panel of Fig. 5.13. On the other hand, for $\gamma = 90^o$, the $Z_{DR}(v)$ is 0 at all the radial velocity components due to the spherical symmetry particles shape. No useful Z_{DR} spectrum information is available to the retrieval. Therefore, in the selection of elevation angles, there is a trade-off between the large number of spectral components and significant Z_{DR} spectrum information. The elevation angle of 45^o used in the retrieval follows the one used in Moisseev et al. (2006) and Spek et al. (2007).

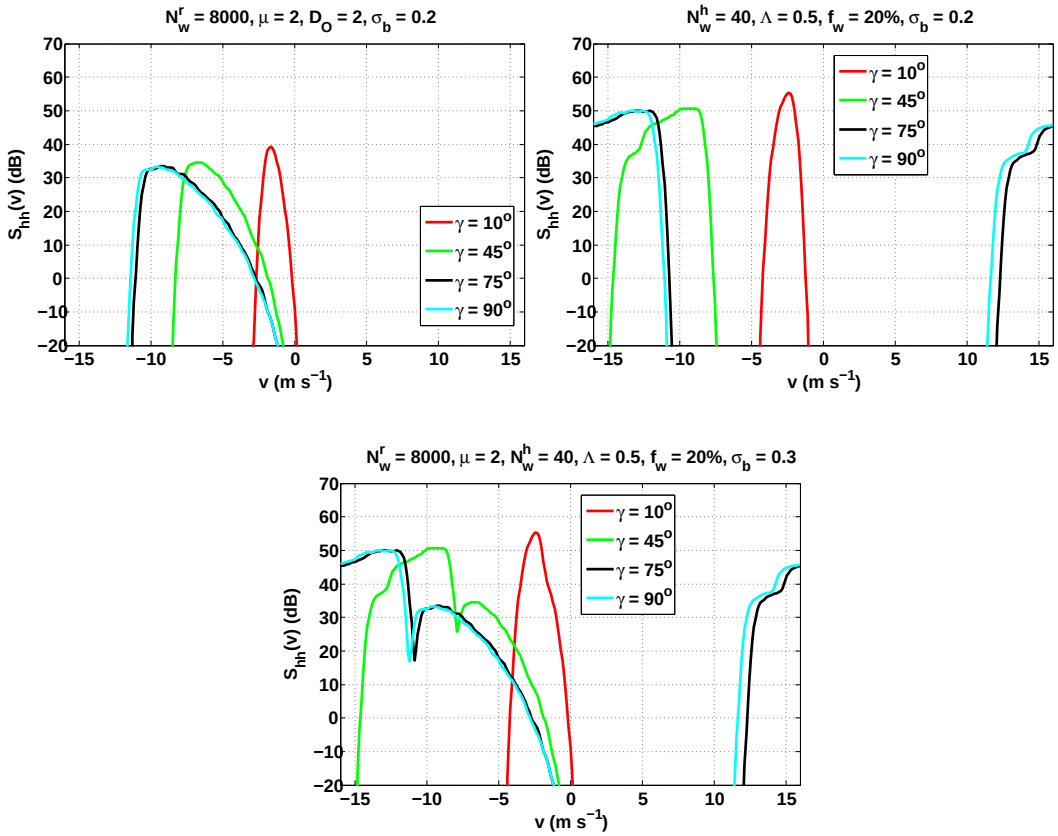

Figure 5.12: Simulated Doppler spectra from pure rain (top left), pure hail (top right) and mixture of rain and hail (bottom) for hh polarization. The elevation angle of 10^o, 45^o, 75^o and 90^o, respectively. The X axis is the Doppler velocity in m s^{-1}, and Y axis is the spectral reflectivity in dB

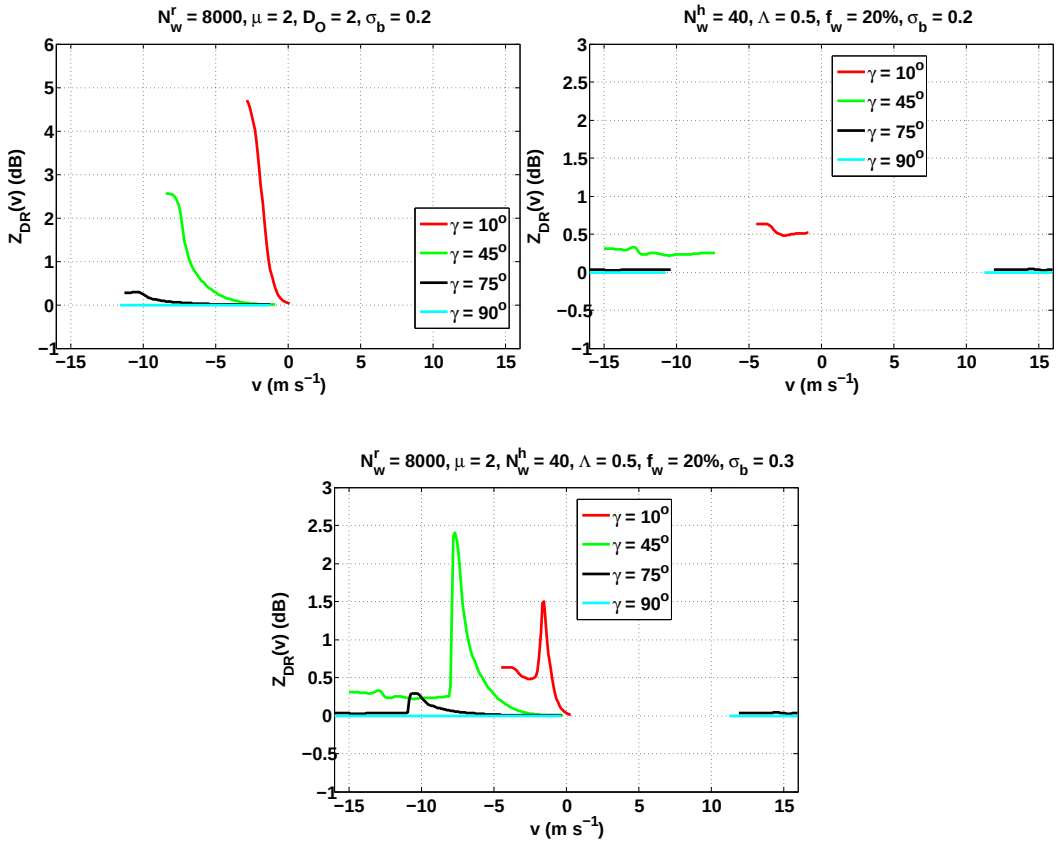

Figure 5.13: Similar to Fig. 5.12, but for $Z_{DR}(v)$.

5.5 Retrieval of Particles' DSDs and the Melting Ratio

From previous analysis, it is clear that the model of Doppler spectrum and differential reflectivity spectrum is determined by eight parameters of N_w^r, D_0, μ, N_w^h, Λ, F_w, σ_b and v_0. Therefore, one can formulate the retrieval problem as an optimization of fitting observations to model spectra described in the following.

$$\min_{N_w^r, D_0, \mu, N_w^h, \Lambda, F_w, \sigma_b, v_0} \sum_{v=-v_a}^{v_a} \{\log[S_{hh}^{mod}(v, N_w^r, D_0, \mu, N_w^h, \Lambda, F_w, \sigma_b, v_0)dv] - \log[S_{hh}^{meas}(v)dv]\}^2 \tag{5.34}$$

$$\min_{N_w^r, D_0, \mu, N_w^h, \Lambda, F_w, \sigma_b, v_0} \sum_{v=-v_a}^{v_a} \{\log[Z_{DR}^{mod}(v, N_w^r, D_0, \mu, N_w^h, \Lambda, F_w, \sigma_b, v_0)dv] - \log[Z_{DR}^{meas}(v)dv]\}^2 \tag{5.35}$$

where S_{hh}^{meas} and Z_{DR}^{meas} are the measured Doppler and differential reflectivity spectra, and S_{hh}^{mod} and Z_{DR}^{mod} are the modeled Doppler spectrum and differential reflectivity spectra defined in Eq. (5.31) and (5.32), respectively. In order to suppress the statistical fluctuation, the optimization is performed in the log-domain (Sato et al. 1990). Similar approach is also adopted in the work of Moisseev et al. (2006) and Spek et al. (2007).

5.5.1 Introduction of genetic algorithm

The nonlinear least square fitting method, such as Levenberg-Marquardt Algorithm (LMA), is usually implemented in the retrieval process (e.g., Sato et al. 1990; Moisseev et al. 2006; Spek et al. 2007). In this work, the Genetic Algorithm (GA), which can solve both constrained and unconstrained optimization problems based on natural selection, is proposed for the retrieval. The GA can be used to solve a variety of optimization problems that are not well suited for standard optimization algorithms, including problems in which the objective function is discontinuous, nondifferentiable, stochastic, or highly nonlinear. Compared to traditional deterministic optimization

algorithms such as LMA, the GA strategy can increase the probability of obtaining the global minimum instead of local minimum (Sellami et al. 2007). The GA repeatedly modifies the population of individual solutions. At each step, the GA selects individuals from the current population termed parents and uses them to produce the children for the next generation. Over successive generations, the population "evolves" toward an optimal solution. A model of Doppler and Z_{DR} spectra is first developed using 8 parameters of the DSD of raindrops and melting hailstones (5 parameters), melting ratio, ambient radial velocity, and turbulence broadening. The GA is introduced to estimate the 8 parameters based on the minimization between the model and observed spectra. The GA retrieval for this work is summarized in the following steps.

1. In the retrieval problem, the N_w^r, f_w, ... are the individuals, and the fitness function is defined by the following two equations.

$$f_1(\Upsilon) = \sum_{v=-v_a}^{v_a} \{\log[S_{hh}^{mod}(v,\Upsilon)dv] - \log[S_{hh}^{meas}(v)dv]\}^2 \tag{5.36}$$

$$f_2(\Upsilon) = \sum_{v=-v_a}^{v_a} \{\log[Z_{DR}^{mod}(v,\Upsilon)dv] - \log[Z_{DR}^{meas}(v)dv]\}^2 \tag{5.37}$$

   where Υ is used to represent the population which is the set of the 8 parameters $(N_w^r, D_0, \mu, N_w^h, \Lambda, F_w, \sigma_b, v_0)$. The algorithm begins by creating a random initial population. If the first guess of each individual can be provided, the initial population will be around the first guess.

2. The value of the fitness function for the current population is computed and scored. A group of individuals associated with better (lower) fitness values in the current population is selected as parents (also called elite), and others are eliminated from current population.

3. Those parents are used to create the children that make up the next generation. Three ways can be used to create children for the next generation: the children

from survived elite parent; the crossover children created by combining the vectors of a pair of parents; and the mutation children created by introducing random changes to parents. In this retrieval problem, the method of crossover and mutation children is used.

4. The current generation is replaced by a new generation. Repeat the first three steps until the global optimal fitness value is achieved. Then the newest generation will be the final results. The optimal fitness can be defined as the output of fitness function reaches a pre-defined value (tolerance error), or the generation after pre-defined iterations.

5.5.2 Retrieval procedure

In section 5.5.1, the retrieval problem is formulated as an optimization problem of finding the minimal difference of the observed spectrum and model spectrum defined by the 8 unknowns. In order to increase the convergent rate in the retrieval, the intervals for the following 6 parameters are selected.

$$0\% \leq \quad F_w \quad \leq 100\% \tag{5.38}$$

$$0 \leq \quad D_0 \quad \leq 5 \tag{5.39}$$

$$-4 \leq \quad \mu \quad \leq 4 \tag{5.40}$$

$$0 \leq \quad N_w^h \quad \leq 80 \tag{5.41}$$

$$0 \leq \quad \Lambda \quad \leq 5 \tag{5.42}$$

$$0 \leq \quad \sigma_b \quad \leq 5 \tag{5.43}$$

It should be noted that generally the interval of these parameters are not necessary for GA problems. However, in this work, some parameters have limited values from previous observations and research. For example, the melting ratio F_w should be between 0% and 100%. Therefore, optimal results can be reached with fewer iterations if the interval of these parameters are used. Following the procedure developed by

Moisseev et al. (2006), one simplification was made by removing the estimation of the ambient air velocity v_0 from the GA fitting. It should be noted that v_0 is estimated by finding the lag at which the cross correlation of modeled and measured spectra is maximum (Moisseev et al. 2006). Moreover, in this work, in order to further decrease the statistical fluctuation, 20 Doppler spectra from two adjacent azimuth angles and 10 consecutive range gates are averaged.

5.6 Evaluation of the Retrieval Algorithm

The performance of the GA retrieval algorithm is demonstrated and evaluated in this section using simulations. The normalized error from initial guess and error after the retrieval is completed, is defined by $\epsilon_i = |\psi_m - \psi_i|/\psi_m$ and $\epsilon_r = |\psi_m - \psi_r|/\psi_m$, respectively, where ψ_m, ψ_i and ψ_r represent the model parameters, initial guess, and the retrieval results. The DSD parameters and the melting ratio of the model, initial guess, the mean and standard deviation of 30 realizations, and the mean ϵ_r ($\bar{\epsilon_r}$) are provided in Table 5.1. Since N_w^r has relative small effect on Doppler spectrum and has no effect on Z_{DR} spectrum as shown in section 5.4, large errors are expected in the retrieval result. The N_w^r in the model and initial guess is 8000 and 7000, respectively. The resultant mean and the standard deviation of the retrieval is 6947 and 1094, respectively. The high SD indicates the retrieval of N_w^r is unstable and sensitive to small changes in the Doppler spectrum. Similar to N_w^r, relative small effect on both spectra can explain the large SD of the retrieved μ, Better retrieval results can be observed for D_0, N_w^h, Λ, F_w and σ_b, which are manifested by small ϵ_r and small standard deviation. It is because these 5 parameters have significant effects on the Doppler spectrum and Z_{DR} spectrum compared to N_w^r and μ as shown previously.

The performance of the proposed retrieval technique is further tested and the impact of F_w on the retrieval is presented in Fig. 5.14. Large errors are likely to be generated in the retrieval of N_w^r and μ, and therefore they are not included in

	Model Value	Initial Value	Retrieval Result	$\bar{\epsilon_r}$
N_w^r	8000	7000	6947 (mean) 1094 (std)	13.16%
D_0	2	4.5	1.92 (mean) 0.077 (std)	4%
μ	2	1	1.03 (mean) 0.3 (std)	48.5%
N_w^h	60	40	63.51 (mean) 7.66 (std)	5.85%
Λ	0.6	0.4	0.6125 (mean) 0.0832 (std)	2.08%
F_w	60%	10%	61.376%(mean) 7.98% (std)	2.29%
σ_b	0.6	0.2	0.6124 (mean) 0.012% (std)	2.07%

Table 5.1: The DSD parameters and melting ratio of model, initial guess, and the mean and standard deviation of the retrieval results from 30 realizations.

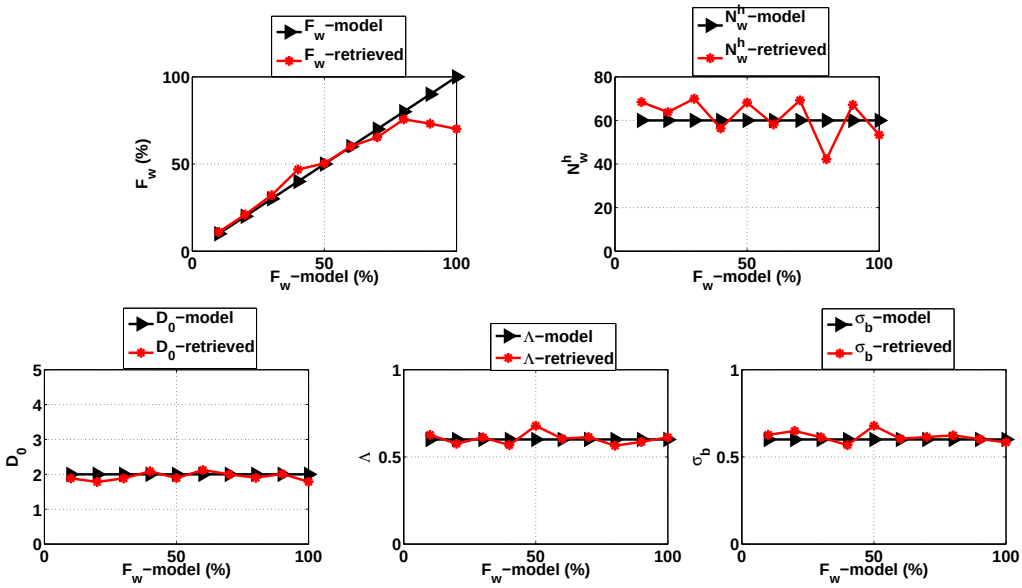

Figure 5.14: The retrieval results from F_w (top left), N_w^h (top right), D_0 (bottom left), Λ (bottom middle) and σ_b (bottom right) for different input F_w.

the sensitivity test. In Fig. 5.14, the F_w-model is changed from 10% to 100% with step of 10%. The N_w^h, D_0, Λ and σ_b are set as 60, 2, 0.6 and 0.6, respectively. When F_w-model change from 0% to 70%, the F_w can be retrieved accurately. However, after F_w-model reaches 70%, the retrieved F_w exhibits large errors and fluctuates around approximately 70%. It can be explained by examining Figs. 5.8 and 5.9, where F_w-model has limited effect on Doppler spectrum and Z_{DR} spectrum after F_w-model reaches 70%. Retrieval error of N_w^h can be observed with maximum ϵ_r of 0.2956 (when $F_w = 80\%$) and mean ϵ_r of 0.1279. On the other hand, it can be shown from from Fig. 5.14 that D_0, Λ and σ_b can be accurately retrieved with the mean ϵ_r of 0.0546, 0.0422 and 0.0431, respectively.

In the simulation, the elevation angle was 45^o, and 256 samples were used to generate the Doppler and Z_{DR} spectra. Moreover, 20 spectra were averaged in the retrieval to reduce the statistical fluctuations. In summary, the simulation results indicate that the GA algorithm can retrieve DSD parameters and melting ratio with small normalized errors and standard deviations.

5.7 Conclusion and Future Work

In this work, a new technique to retrieve the DSDs of raindrops and melting hailstones as well as the melting ratio of hailstones was developed using Doppler and Z_{DR} spectra. As a part of the proposed method, the relationship between the melting ratio and the backscattering cross section of hailstones was obtained using polynomial fitting to the pre-calculated T-matrix results at C-band. It has been shown that the GA can provide reasonable retrieval in the optimization problem of multiple unknown parameters.

A microphysical model was developed for the mixture of raindrops and melting hailstones. This model depends on eight parameters: the gamma drop size distribution of raindrops (N_w^r, D_0 and μ) and hailstones (N_w^h and Λ), the melting ratio

of hailstones (F_w), the spectral broadening (σ_b), and the ambient wind velocity (v_0). The output of the model is the Doppler spectrum and differential reflectivity spectrum. Moreover, it was suggested that the ambient wind velocity can be estimated independently through cross-correlation analysis. As a result, the retrieval becomes a minimization with 7 unknowns. Since the problem is designed to retrieve two types of hydrometeors (raindrops and melting hailstones), the presence of other type particles such as snow (mixture of air, water and ice) may produce additional errors in the retrieval.

Some assumptions and simplifications were made in the microphysical model of the hailstones. First, the shedding process was not considered although the shedding will change the DSD of raindrops. This algorithm retrieves the instant DSD of raindrops and hailstones only at relatively high elevation angles when the Doppler sorting is sufficient. Second, when a hailstone start to melt, the water fraction on the surface of the hailstone will decrease its terminal velocity. The amount of decrease in velocity is proportional to the amount of water on the hail's surface. Although few models were developed to describe relations between the melting and the terminal velocity of hailstones in previous work (e.g. Rasmussen et al. 1984b; Rasmussen and Heymsfield 1987; List et al. 1973), however there is no well accepted model in current stage. Since the focus of this work is not the study of the terminal velocity under different melting ratios, the equation proposed by Mitchell (1996) was used in this work. The parameters in the model were obtained from the fitting results from plentiful hailstones samples from summer seasons, which could be used to represent the mean velocities under various melting ratios for each size. However, bias is expected in the terminal velocity calculation. Third, in order to mitigate the impact of random fluctuation on the retrieval results, spectra used for the retrieval have been averaged over 20 adjacent gates. In other words, the spatial resolution of the retrieval is compromised.

Since DSD and melting ratio retrieval is the most critical part of this study, it would be advantageous of validate the retrieved results. The special setup required by this retrieval (45^o elevation angle and higher) make it difficult to compare the retrieved parameters to in-situ instruments. However, indirect validations of the retrieved melting ratio, nonetheless, is still possible. Since the hailstones are assumed melting when they are falling, larger melting ratio is expected at low altitude compared to high altitude. Therefore retrieval algorithm can be tested at two different elevation angles (30^o and 45^o), and the melting ratio retrieved from 30^o is expected higher than from 45^o. Even this approach can not evaluate the performance quantitatively, but still can qualitatively show the feasibility of this algorithm in the melting ratio retrieval.

The spectral broadening has relative large influence on the retrieval accuracy. This is a general limitation applicable to most DSD parameters retrieval methods based on the analysis of spectra. The statistical analysis of the performance of this retrieval algorithm under different spectral broadening, elevation angle, FFT length, etc. is needed to further demonstrate the feasibility of the algorithm. Similar analysis can be found in the work from Moisseev et al. (2006). Since unusual setting is required for the radar to collect the data for this research (elevation angle of 45^o and higher), and the mixture of raindrops and hailstones is not a very common type of precipitation, there is no real data collected for this work in current stage. Real case analysis is the most important part to validate the application of the proposed method, and will be implemented in future work.

Chapter 6

Conclusions and Future Work

6.1 Summary and Conclusions

In this dissertation, the application of the spectral analysis and two AI methods to weather radar were explored in two areas of tornado detection and retrieval of microphysical properties for rain-hail mixture. A hybrid method of fuzzy logic and neural network was developed for tornado detection and is termed NFTDA, which can integrate tornado signatures in velocity, spectral, and polarimetric domains, with the goals of enhancing the performance compared to the convectional TDA. Moreover, a genetic algorithm (GA) was introduced to retrieve the DSD of both raindrops and melting hailstones, the melting ratio, ambient wind, and turbulence broadening using Doppler and Z_{DR} spectra for the case where rain and melting hails are present simultaneously within the radar volume. The important results from this dissertation are highlighted as follows.

- Three parameters of spectral flatness (σ_s), higher-order spectra of PRIB (P) and Eigen-ratio (χ_R) were defined to characterize the unique spectral signatures of tornadoes in addition to spectrum width (σ_v). It has been shown that larger σ_v, P, χ_R and lower σ_s can be observed from tornado spectra than those from non-tornado spectra. The dependence of these four parameters on range, reflectivity structure, and relative location within the radar resolution volume

were statistically analyzed using numerical simulations. It is shown that these feature parameters are complementary to each other and some spectral features can be maintained while the shear signature becomes degraded. In other words, the TSS has the potential to facilitate or improve tornado detection.

- The impact of super-resolution on tornado shear, spectral and polarimetric signatures was investigated using numerical simulations and analysis of real tornado cases. The results have shown that compared to legacy resolution, super-resolution can enhance tornado signatures, which can lead to better tornado detection.

- In this work, a novel NFTDA was developed to integrate the shear, spectral and polarimetric signatures of tornadoes using a fuzzy logic framework. A neural network was included to optimize the algorithm through a training process. The NFTDA is flexible enough to take in a portion of or all the tornado signatures. In this work, four different combinations of feature parameters (NFTDA-D, NFTDA-P, NFTDA-S and NFTDA-A) for legacy and/or super-resolutions were studied based on (1) the availability of feature parameters, (2) performance behavior, and (3) research values. Consequently, their performance were statistically analyzed as a function of range and tornado strength. Compared to the conventional shear-based TDA, NFTDA provides higher POD, lower FAR, and extended detection range.

- In this work, spectral analysis and GA method were proposed to estimate the DSD of both raindrops and melting hailstones, the melting ratio, the turbulence broadening and ambient air velocity. The model of Doppler and Z_{DR} spectra from the mixture of raindrops and melting hails was established and the impact of melting ratio on Doppler and Z_{DR} spectra was studied for the first time. In the GA retrieval, the relationship between the backscattering amplitude and the

melting ratio was obtained by polynomial fitting. In other words, there is no need to calculate the backscattering amplitude from T-matrix in each iteration and therefore, the retrieval can be accomplished in an efficient manner. The feasibility of the GA-based retrieval algorithm was demonstrated and verified using numerical simulations.

6.2 Future Work

The major tasks for subsequent research are proposed in the following.

- The tornado spectral signatures revealed in Doppler spectrum and polarimetric signatures in Z_{DR} and ρ_{hv} were studied and applied to NFTDA in this work. However, it is speculated that additional tornado features may reside in polarimetric spectra of Z_{DR} and ρ_{hv}, which can be used to further improve tornado detection and possibly prediction. In order to carry out this work, time series data from both polarizations are needed. For example, the high resolution polarimetric radar OU-PRIME on south campus can be a candidate for this research.

- In this work, the NFTDA is mainly designed for S-band radar such as WSR-88D, whose scanning patterns does not change constantly. On the other hands, many research and operational radars have flexible scanning patterns. It is of interest to systematically study the impact of scanning strategies on the performance of NFTDA with different combination of input signatures.

- The retrieval algorithm has been demonstrated using simulations. But a comprehensive statistical analysis of this algorithm is needed such as the sensitivity of the retrieval to different elevation angle, spectral broadening, FFT length and SNR. Moreover, implementation of this algorithm on real data is needed to further verify the feasibility of the proposed algorithm.

- The enhanced tornado debris and spectral signatures have been observed using super-resolution. Therefore, NFTDA using all the tornado signatures for super-resolution data (NFTDA-AS) can produce the best performance among all other combinations. The statistical performance of NFTDA-AS is needed to be analyzed using real tornado cases due to its attractive behavior.

Bibliography

Adlerman, E., K. Droegemeier, and R. Jones, 1999: A numerical simulation of cyclic mesocyclogenesis. *J. Atmos. Sci.*, **56**, 2045–2069.

Atlas, D., 1963: Radar analysis of severe storms. *Meteor. Monogrv.*, **27**, 177–220.

Atlas, D., R. C. Srivastava, and R. S. Sekhon, 1973: Doppler radar characteristics of precipitation at vertical incidence. *Rev. Geophys. Space Phys.*, **11**, 1–35.

Bachmann, S. and D. S. Zrnić, 2005: Spectral polarimetry for identifying and separating mixed biological scatterers. *32nd Conference on Radar Meteorology*, AMS, P9R.5.

Bachmann, S. and D. S. Zrnić, 2006: Spectral density of polarimetric variables separating biological scatterers in the VAD display. *J. Atmos. Oceanic Technol.*, **24**, 1186–1198.

Balakrishnan, N. and D. S. Zrnić, 1990: Estimation of rain and hail rates in mixed-phase precipitation. *J. Atmos. Sci.*, **47**, 565–583.

Balakrishnan, N. and D. S. Zrnic, 1990: Use of polarization to characterize precipitation and discriminate large hail. *J. Atmos. Sci.*, **47**, 1525–1540.

Battan, L. J. and J. B. Theiss, 1973: Wind gradients and variance of Doppler spectra in showers viewed horizontally. *J. Appl. Meteorol.*, **12**, 688–693.

Baum, B. A., V. Tovinkere, J. Titlow, and R. M. Welch, 1997: Automated cloud classification of global avhrr data using a fuzzy logic approach. *J. Appl. Meteorol.*, **36**, 1519–1540.

Bianco, L. and J. M. Wilczak, 2002: Convective boundary layer depth: improved measurement by Doppler radar wind profiler using fuzzy logic methods. *J. Atmos. Oceanic Technol.*, **19**, 1745–1758.

Bieringer, P. and P. S. Ray, 1996: A comparison of tornado warning lead times with and without NEXRAD Doppler radar. *Wea. Forecasting*, **11**, 47–52.

Bluestein, H. B., M. M. French, and L. R. Tanamachi, 2006: Close-range observations of tornadoes in supercells made with a dual-polarization, X-band, mobile Doppler radar. *Mon. Weather Rev.*, **135**, 1522–1543.

Bluestein, H. B., J. G. Ladue, H. Stein, and D. Speheger, 1993: Doppler radar wind spectra of supercell tornadoes. *Mon. Weather Rev.*, **121**, 2200–2221.

Bluestein, H. B., W.-C. Lee, M. Bell, C. C. Weiss, and A. L. Pazmany, 2003: Mobile Doppler radar observations of a tornado in a supercell near Bassett, Nebraska, on 5 June 1999, part II: Tornado-vortex structure. *Mon. Weather Rev.*, **131**, 2968–2984.

Bluestein, H. B., W. P. Unruh, and H. Stein, 1997: Doppler radar analysis of the Northfield, Texas, tornado of 25 May 1994. *Mon. Weather Rev.*, **125**, 212–230.

Brandes, E. A. and K. Ikeda, 2004: Freezing-level estimation with polarimetric radar. *J. Appl. Meteorol.*, **43**, 1541–1553.

Bringi, V. N. and V. Chandrasekar, 2001: *Polarimetric Doppler Weather Radar Principles and Applications*. Cambridge University Press, Cambridge, UK.

Brotzge, J. A., K. Brewster, B. Johnson, B. Philip, M. Preston, D. Westbrook, and M. Zink, 2005: CASA's first test bed: Integrated project 1. *32th Conference on Radar Meteorology*, Amer. Meteor. Soc., Albuquerque, NM, 14R.2.

Brown, R. A., 1998: Nomogram for aiding the interpretation of tornadic vortex signatures measured by Doppler radar. *Wea. Forecasting*, **13**, 505–512.

Brown, R. A. and L. R. Lemon, 1976: Single Doppler radar vortex recognition. Part II: Tornadic vortex signatures. *Prepr. Radar Meteor. Conf.*, **104-109**.

Brown, R. A., L. R. Lemon, and D. W. Burgess, 1978: Tornado detection by pulsed Doppler radar. *Mon. Weather Rev.*, **106**, 29–38.

Brown, R. A. and V. T. Wood, 1991: On the interpretation of single-Doppler velocity patterns within severe thunderstorms. *Wea. Forecasting*, **6**, 32–48.

Brown, R. A., V. T. Wood, and D. Sirmans, 2002: Improved tornado detection using simulated and actual WSR-88D data with enhanced resolution. *J. Atmos. Oceanic Technol.*, **19**, 1759–1771.

Burgess, D. W., L. R. Lemon, and R. A. Brown, 1975: Tornado characteristics revealed by doppler radar. *Geophys. Res. Lett.*, **183-184**.

Burgess, D. W., V. T. Wood, and R. A. Brown, 1982: Mesocyclone evolution statistics. *12nd Conference on Severe Local Storms*, AMS, San Antonio, TX., 422–424.

Capsoni, C. and M. D'Amico, 1998: A physically based radar simulator. *J. Atmos. Oceanic Technol.*, **15**, 593–598.

Capsoni, C., M. D'Amico, and R. Nebuloni, 2001: A multiparameter polarimetric radar simulator. *J. Atmos. Oceanic Technol.*, **18**, 1799–1809.

Chandran, V., B. Carswell, B. Boashash, and S. L. Elgar, 1997: Pattern recognition using invariants defined from high order spectra: 2-d image inputs. *IEEE Trans. Image Processing*, **6**, 703–712.

Chandran, V. and S. L. Elgar, 1993: Pattern recognition using invariants defined from high order spectra- one-dimensional inputs. *IEEE Trans. Signal Processing*, **41**, 205–212.

Cheng, L. and M. English, 1983: A relationship between hailstone concentration and size. *J. Atmos. Sci.*, **40**, 204–213.

Chiu, S. L., 1996: Selecting input variables for fuzzy models. *J. Intelligent Fuzzy Sys.*, **4**, 243–256.

Cornman, L. B., R. K. Goodrich, C. S. Morse, and W. L. Ecklund, 1998: A fuzzy logic method for improved moment estimation from doppler spectra. *J. Atmos. Oceanic Technol.*, **15**, 1287–1305.

Council, N. R., 2002: *Weather Radar Technology beyond NEXRAD*.

Crum, T. D. and R. L. Alberty, 1993: The WSR-88D and the WSR-88D operational support facility. *Bull. Amer. Meteor. Soc.*, **74**, 1669–1687.

Davies-Jones, R., 1984: Streamwise vorticity: The origin of updraft rotation in supercell storm. *J. Atmos. Sci.*, **20**, 2991–3006.

Doviak, R. J. and D. S. Zrnić, 1993: *Doppler Radar and Weather Observations*. Academic Press, San Diego, Calif., 130 pp, 130-134 pp.

Dowell, D. C., C. R. Alexander, J. M. Wurman, and L. J. Wicker, 2005: Centrifuging of hrdrometeors and debris in tornadoes: radar-reflectivity patterns and wind measurments errors. *Mon. Weather Rev.*, **133**, 1501–1524.

Fabry, F. and R. J. Keeler, 2003: Innovative signal utilization and processing. *Radar and Atmospheric Science: A Collection of Essays in Honor of David Atlas*, R. M. Wakimoto and R. C. Srivastava, Eds., AMS, Boston, Mass., 199–214.

Forbes, G. S., 1981: On the reliability of hook echoes as tornado indicators. *Mon. Weather Rev.*, **109**, 1457–1466.

Fujita, T., 1958: Mesoanalysis of the illinois tornadoes of 9 April 1953. *J. Atmos. Sci.*, **15**, 288–296.

Gaweda, A. and J. Zurada, 2001: Input selection in data-driven fuzzy modeling. *Proc. 10th IEEE Internat. Conf. Fuzzy Systems*.

Goddard, J. W. F., S. M. Cherry, and V. N. Bringi, 1982: Comparison of dual-polarized radar measurements of rain with ground-based disdrometer measurements. *J. Appl. Meteorol.*, **21**, 252–256.

Gorgucci, E., G. Scarchilli, V. Chandrasekar, and V. N. Bringi, 2002: Estimation of raindrop size distribution parameters from polarimetric radar measurements. *J. Atmos. Sci.*, **59**, 2373–2384.

Gourley, J. J., P. Tabary, and J. P. Chatelet, 2007: A fuzzy logic algorithm for the separation of precipitating from nonprecipitating echoes using polarimetric radar observation. *J. Atmos. Oceanic Technol.*, **24**, 1439–1451.

Green, A. V., 1975: An approximation for shape of large raindrops. *J. Appl. Meteorol.*, **14**, 1578–1583.

Hendry, A. and G. C. McCormick, 1976: Radar observations of the alignment of precipitation particles by electrostatic fields in thunderstorms. *J. Geophys. Res.*, **81**, 5353–5357.

Holt, A. R., 1984: Some factors affecting the remote sensing of rain by polarization diversity radar in the 3 to 35 ghz frequency range. *Radio Sci.*, **19**, 1399–1412.

Ice, R. L., D. A. Warde, D. Sirmans, and D. Rachel, 2004: Open RDA-RVP8 signal processing. Part I: simulation study. WSR-88D Radar Operations Center Rep. 87pp.

Jang, J.-S. R., 1996: Input selection for anfis learning. *Proc. IEEE Internat. Conf. Fuzzy Systems*, 1493–1499.

Janssen, L. H. and G. A. V. D. Spek, 1985: The shape of Doppler spectra from precipitation. *IEEE Trans. Aerosp. Electron. Syst.*, **21**, 208–219.

Jung, Y., G. Zhang, and M. Xue, 2007: Assimilation of simulated polarimetric radar data for a vonvective storm using the ensemble kalman filter. Part I: observation operators for reflectivity and polarimetric variables. *Mon. Weather Rev.*, **136**, 2228–2245.

Kessinger, C., S. Ellis, and J. V. Andel, 2003: The radar echo classifier: A fuzzy logic algorithm for the WSR-88D. *3rd Conference on Artificial Intelligence Applicaitons to the Environmental Science*, AMS.

Knight, N. C., 1982: Hailstone shape factor and its relation to radar interpretation of hail. *J. Climate Appl. Meteor.*, **25**, 1956–1958.

Kumjian, M. R. and A. V. Ryzhkov, 2008: Polarimetric signatures in supercell thunderstorms. *J. Appl. Meteorol.*, **47**, 1940–1961.

Kundu, P. K. and I. M. Cohen, 2002: *Fluid Mechanics*. Academic Press, 730 pp.

Lakshmanan, V., T. Smith, G. J. Stumpf, and K. Hondl, 2007: The warning decision support system - integrated information (WDSS-II). *Wea. Forecasting*, **22**, 592–608.

Law, J. O. and D. A. Parson, 1943: The relationship of raindrop size to intensity. *Trans. Amer. Geophys. Union.*, **24**, 452–460.

Liao, L., R. Meneghini, T. Iguchi, and A. Detwiler, 2005: Use of dual-wavelength radar for snow parameter estimates. *J. Atmos. Oceanic Technol.*, **22**, 1494–1506.

Liao, X. and Z. Bao, 1998: Circularly integrated bispectra: Novel shift invariant features for high-resolution radar target recognition. *Electron. Lett.*, **34**, 1879–1880.

List, R., U. W. Rentsch, A. C. Byram, and E. P. Lozowski, 1973: On the aerodynamics of spheroidal hailstone models. *J. Appl. Meteorol.*, **30**, 653–661.

Liu, H. and V. Chandrasekar, 2000: Classification of hydrometeors based on polarimetric radar measurements: Development of fuzzy logic and neuro-fussy system, and in-situ verification. *J. Atmos. Oceanic Technol.*, **17**, 140–164.

Liu, H., V. Chandrasekar, and G. Xu, 2001: An adaptive neural network scheme for radar rainfall estimation from WSR-88D observations. *J. Appl. Meteorol.*, **40**, 2038–2050.

Marshall, J. S. and W. Palmer, 1948: The distribution of raindrops with size. *J. Meteor.*, **5**, 165–166.

Marzban, C. and G. J. Stumpf, 1996: A neural network for tornado prediction based on Doppler radar-derived attributes. *J. Appl. Meteorol.*, **35**, 617–626.

Marzban, C. and G. J. Stumpf, 1998: A neural network for damaging wind prediction. *Wea. Forecasting*, **13**, 151–163.

Marzban, C. and A. Witt, 2001: A bayesian neural network for severe-hail size prediction. *Wea. Forecasting*, **16**, 600–610.

Matrosov, S. Y., 1998: A dual-wavelength radar method to measure snowfall rate. *J. Appl. Meteorol.*, **37**, 1510–1521.

Matson, R. and A. W. Huggins, 1980: The direct measurement of the sizes, shapes and kinematics of falling hailstones. *J. Atmos. Sci.*, **37**, 1107–1125.

Maxwell-Garnett, J. C., 1904: Colors in metal glasses and in metallic films. *Philos. Trans. Roy. Soc. London*, **A203**, 385–420.

Mendel, J. M., 1995: Fuzzy logic systems for engineering: A tutorial. *Proc. IEEE*, **83**, 345–377.

Metcalf, J. I., 1988: A new slant on the distribution and measurement of hydrometeor canting angles. *J. Atmos. Oceanic Technol.*, **5**, 571–578.

Mitchell, D. L., 1996: Use of mass- and area-dimensional relationships for determining precipitation particle terminal velocities. *J. Appl. Meteorol.*, **53**, 1710–1723.

Mitchell, E. D., S. V. Vasiloff, G. J. Stumpf, A. Witt, M. D. Eilts, J. T. Johnson, and K. W. Thomas, 1998: The National Severe Storms Laboratory tornado detection algorithm. *Wea. Forecasting*, **13**, 352–366.

Moisseev, D. N. and V. Chandrasekar, 2007: Ice particles classification using dual-polarization spectral observations. *33rd Conference on Radar Meteorology*, AMS, 8A.6.

Moisseev, D. N. and V. Chandrasekar, 2008: Polarimetric spectral filter for adaptive clutter and noise suppression. *J. Atmos. Oceanic Technol.*, **26**, 215–228.

Moisseev, D. N., V. Chandrasekar, C. M. H. Unal, and H. W. J. Russchenberg, 2006: Dual-polarization spectral analysis for retrieval of effective raindrop shapes. *J. Atmos. Oceanic Technol.*, **23**, 1682–1695.

Moisseev, D. N., C. M. H. Unal, H. W. J. Russchenberg, and L. Ligthart, 2002: A new method to seperate ground clutter and atmospheric reflection in the case of similar Doppler velocities. *IEEE Trans. Geosci. Remote Sens.*, **40**, 239–246.

Monson, M. H., 1996: *Statistical digital signal processing and modeling*. Wiley, 624P.

Nespor, V., W. F. Krajewski, and A. Kruger, 2000: Wind-induced error of rain drop size distribution measurement using a two-dimensional video disdrometer. *J. Atmos. Oceanic Technol.*, **17**, 1483–1492.

Nikias, C. L. and M. R. Raghuveer, 1987: Bispectrum estimation: A digital signal processing framework. *Proc. IEEE*, **75**, 869–891.

Oppenheim, A. V. and J. S. Lim, 1981: The importance of phase in signals. *Proc. IEEE*, **69**, 529–541.

Papoulis, A. and S. U. Pillai, 2002: *Probability, Random Variables, and Stochastic Processes*. McGraw-Hill, New York, NY.

Polger, P. D., B. S. Goldsmith, and R. C. Bocchierri, 1994: National Weather Service warning performance based on the WSR-88D. *Bull. Amer. Meteor. Soc.*, **75**, 203–214.

Pruppacher, H. R. and R. L. Pitter, 1971: A semi-empirical determination of the shape of cloud and rain drops. *J. Atmos. Sci.*, **28**, 86–94.

Rasmussen, R. M. and A. J. Heymsfield, 1987: Melting and shedding of graupel and hail. Part I: model physics. *J. Atmos. Sci.*, **19**, 2754–2763.

Rasmussen, R. M., V. Levizzani, and H. R. Pruppacher, 1984a: A wind tunnel and theoretical study on the melting behavior of atmospheric ice particles: III. experiment and theory for spherical ice particles of radius < 500 um. *J. Atmos. Sci.*, **41**, 381–388.

Rasmussen, R. M., V. Levizzani, and H. R. Pruppacher, 1984b: A wind tunnel and theoretical study on the melting behavior of atmospheric ice particles: III. experiment and theory for spherical ice particles of radius > 500 um. *J. Atmos. Sci.*, **41**, 381–388.

Root, B., T. Yu, and M. Yeary, 2010: The added value of surface data to radar-derived rainfall rate estimation using an artificial neural network. *J. Atmos. Oceanic Technol.*, submitted.

Ross, T. J., 2005: *Fuzzy logic with engineering applications*. 2nd ed. Wiley, 151 pp.

Ryzhkov, A. and D. Zrnić, 1996: Assessment of rainfall measurement that uses specific differential phase. *J. Appl. Meteorol.*, **35**, 2080–2090.

Ryzhkov, A. V., D. W. Burgess, D. S. Zrnic, T. Smith, and S. E. Giangrande, 2002: Polarimetric analysis of a 3 May 1999 tornado. *21st Conf. on Severe Local Storms*, AMS, 515–518.

Ryzhkov, A. V., T. J. Schuur, D. W. Burgess, and D. S. Zrnic, 2005: Polarimetric tornado detection. *J. Appl. Meteorol.*, **44**, 557–570.

Sachidananda, M. and D. S. Zrnić, 2000: Clutter filtering and spectral moment estimation for Doppler weather radars using staggered pulse repetition time (PRT). *J. Atmos. Oceanic Technol.*, **17**, 323–331.

Sato, T., H. Doji, H. Iwai, I. Kimura, S. Fukao, M. Yamamoto, T. Tsuda, and S. Akto, 1990: Computer processing for deriving drop-size distributions and vertical air velocities from VHF Doppler radar spectra. *Radio Sci.*, **25**, 961–973.

Sellami, A., M. Zagrouba, M. Bouaicha, and B. Bessais, 2007: Application of genetic algorithms for the extraction of electrical parameters of multicrystalline silicon. *Meas. Sci. Technol*, **18**, 1472–1476.

Serafin, R. J. and J. W. Wilson, 2000: Operational weather radar in the United States: progress and opportunity. *Bull. Amer. Meteor. Soc.*, **81**, 501–518.

Shao, Y. and M. Celenk, 2001: Higher-order spectra (HOS) invariants for shape recognition. *Pattern Recognition*, **34**, 2097–2113.

Siggia, A. D. and R. E. Passarelli, 2004: Gaussian model adaptive processing (GMAP) for improved ground clutter cancelation and moment estimations. *Third European Conf. on Radar Meteorology and Hydrology*, **Visby, Sweden**, 67–73.

Simmons, K. M. and D. Sutter, 2005: WSR-88D radar, tornado warnings, and tornado casualties. *Wea. Forecasting*, **20**, 301–310.

Smith, R. L. and D. W. Holmes, 1961: Use of Doppler radar in meteorological observations. *Mon. Weather Rev.*, **89**, 1–7.

Smith, T. M., K. L. Elmore, and S. A. Dulin, 2004: A damaging downburst predicition and detection algorithm for the WSR-88D. *Wea. Forecasting*, **19**, 240–250.

Speheger, A. D., 2006: On the imprecision of radar signature locations and storm path forecasts. *Natl. Wea. Dig.*, **30**, 3–10.

Spek, A. L. J., C. M. H. Unal, D. N. Moisseev, H. W. J. Russchenberg, V. Chandrasekar, and Y. Dufournet, 2007: A new technique to categorize and retrieve the microphysical properties of ice particles above the melting layer using radar dual-polarization spectral analysis. *J. Atmos. Oceanic Technol.*, **25**, 482–497.

Spring, S., et al., 2009: WSR-88D dual polarization initial operational capabilities. *25th Conference on International Interactive Information and Processing Systems (IIPS) for Meteorology, Oceanography, and Hydrology*, AMS.

Stout, G. E. and F. A. Huff, 1953: Radar records Illinois tornadogenesis. *Bull. Amer. Meteor. Soc.*, **34**, 281–284.

Sugeno, M. and T. Yasukawa, 1993: A fuzzy-logic-based approach to qualitative modeling. *IEEE Tran. Fuzzy System*, **1**, 7–31.

Torres, S. M. and C. D. Curtis, 2007: Initial implementation of super-resolution data on the NEXRAD network. *23th Conference on interactive information processing systems (IIPS) Ffor meteorology, oceanography, and hydrology*, AMS.

Tugnait, J. K., 1994: Detection of non-Gaussian signals using integrated polyspectrum. *IEEE Trans. Signal Processing*, **42**, 3137–3149.

Ulbrich, C. W., 1983: Natural variations in the analytical form of the raindrop size distribution. *J. Climate Appl. Meteor.*, **22**, 1764–1775.

Unal, C. M. H. and D. N. Moisseev, 2004: Combined Doppler and polarimetric radar measurements: correction for spectrum aliasing and nonsimultaneous polarimetric measurements. *J. Atmos. Oceanic Technol.*, **21**, 443–456.

Vivekanandan, J., D. S. Zrnic, S. M. Ellis, R. Oye, A. V. Ryzhkov, and J. Straka, 1999: Cloud mircophysics retrival using s-band dual-polarization radar measurements. *Bull. Amer. Meteor. Soc.*, **80**, 381–388.

Vulpiani, G., S. Giangrande, and F. S. Marzano, 2009: Rainfall estimation from polarimetric S-band radar measurements: validation of a neural network approach. *J. Appl. Meteorol.*, **26**, 2022–2036.

Wakasugi, K., A. Mizutani, M. Matsuo, S. Fukao, and S. Kato, 1987: Further discussion on deriving drop-size distribution and vertical air velocities from VHF Doppler radar spectra. *J. Atmos. Oceanic Technol.*, **4**, 170–179.

Wang, Y., T.-Y. Yu, M. Yeary, A. Shapiro, S. Nemati, M. Foster, and J. D. L. Andra, 2008: Tornado detection using a neuro-fuzzy system to integrate shear and spectral signatures. *J. Atmos. Oceanic Technol.*, **25**, 1136–1148.

Williams, C. R., 2002: Simultaneous ambient air motion and rain-drop size distribution retrieved from uhf vertical incident profiler observations. *Radio Sci.*, **37**, 8–1–8–3.

Witt, A., M. D. Eilts, G. J. Stumpf, E. D. Mitchell, J. T. Johnson, and K. W. Thomas, 1998: Evaluating the performance of WSR-88D severe storm detection algorithms. *Wea. Forecasting*, **13**, 513–518.

Wong, R. and N. Chidambaram, 1985: Gamma size distribution and stochastic sampling errors. *J. Appl. Meteorol.*, **24**, 568–579.

Wood, V. T. and R. A. Brown, 1997: Effects of radar sampling on single-Doppler velocity signatures of mesocyclones and tornadoes. *Wea. Forecasting*, **12**, 928–938.

Wurman, J. and S. Gill, 2000: Finescale radar observations of the Dimmitt, Texas (2 June 1995), tornado. *Mon. Weather Rev.*, **128**, 2135–2163.

Yager, R. and D. Filev, 1994: Generation of fuzzy rules by mountain clustering. *J. Intelligent Fuzzy Sys.*, **2**, 209–219.

Yanovsky, F., H. W. J. Russchenberg, and C. M. H. Unal, 2005: Retriveal of information about turbulence in rain by using Doppler-polarimetric radar. *IEEE Trans. Microwave Theory Technol.*, **53**, 444–450.

Yeary, M., S. Nemati, T.-Y. Yu, and Y. Wang, 2007: Tornadic time series detection using eigen analysis and a machine intelligence-based approach. *IEEE Trans. Geosci. Remote Sens.*, **4**, 335–339.

Yu, T.-Y., R. R. Rodiel, and R. D. Palmer, 2008: Investigation of Non-Gaussian weather spectra in a tornadic supercell. *J. Atmos. Oceanic Technol.*, **in press**.

Yu, T.-Y., Y. Wang, A. Shapiro, M. Yeary, D. S. Zrnic, and R. J. Doviak, 2007: Characterization of tornado spectral signatures using higher order spectra. *J. Atmos. Oceanic Technol.*, **24**, 1997–2013.

Zhang, G., J. Viekanandan, and E. Brandes, 2001a: A method for estimating rain rate and drop size distribution from polarimetric radar measurements. *IEEE Trans. Geosci. Remote Sens.*, **39**, 830–841.

Zhang, X., Y. Shi, and Z. Bao, 2001b: A new feature vector using selected bispectra for signal classification with application in radar target recognition. *IEEE Trans. Signal Processing*, **49**, 1875–1885.

Zrnić, D. S., 1975: Simulation of weatherlike Doppler spectra and signals. *J. Appl. Meteorol.*, **14**, 619–620.

Zrnić, D. S., 2007: Polarimetric upgrade of the WSR-88D (NEXRAD) network. *33rd Conference on Radar Meteorology*, AMS, 10.1.

Zrnić, D. S., V. N. Bringi, N. Balakrishman, K. Aydan, V. Chandrasekar, and J. Hubbert, 1993: Polarimetric measurements in a severe hailstorm. *Mon. Weather Rev.*, **121**, 2223–2238.

Zrnić, D. S., D. W. Burgess, and L. D. Hennington, 1985: Doppler spectra and estimated windspeed of a violent tornado. *J. Climate Appl. Meteor.*, **24**, 1068–1081.

Zrnić, D. S. and R. J. Doviak, 1975: Velocity spectra of vortices scanned with a pulsed-Doppler radar. *J. Appl. Meteorol.*, **14**, 1531–1539.

Zrnić, D. S., R. J. Doviak, and D. W. Burgess, 1977: Probing tornadoes with a pulse Doppler radar. *Quart. J. R. Met. Soc.*, **103**, 707–720.

Zrnić, D. S. and M. Istok, 1980: Wind speeds in two tornadic storms and a tornado, deduced from Doppler spectra. *J. Appl. Meteorol.*, **19**, 1405–1415.

Zrnić, D. S., A. Ryzhkov, J. Straka, Y. Liu, and V. Chandrasekar, 2001: Testing a procedure for automatic classification of hydrometeor types. *J. Atmos. Oceanic Technol.*, **18**, 892–913.

AppendixA

The tornado outbreaks on 10 May 2003 was of primary interest in this work. The tornado spectral signatures and debris signatures from two volume scanns were examined in Chapter 3. More examples of σ_v, P, σ_s, χ_R, Z_{DR}, ρ_{hv} and Doppler spectra from this tornado event are presented in this appendix as complement to further demonstrate tornado signatures.

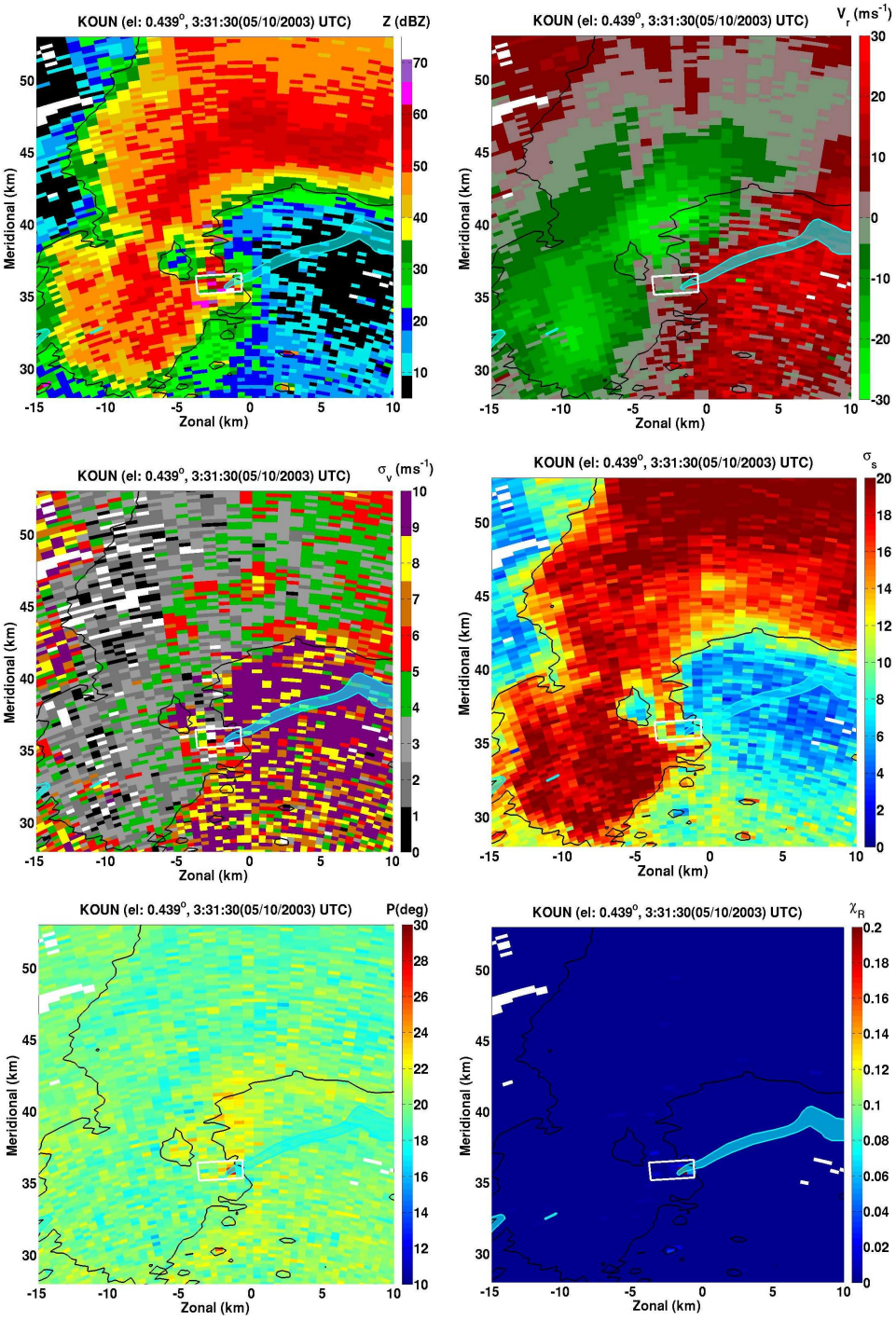

Figure 6.1: Examples of reflectivity (top left), radial velocity (top right), spectrum width (middle left) spectral flatness (middle right), PRIB (bottom left), eigen-ratio (bottom right) at 331 UTC 10 May 2003

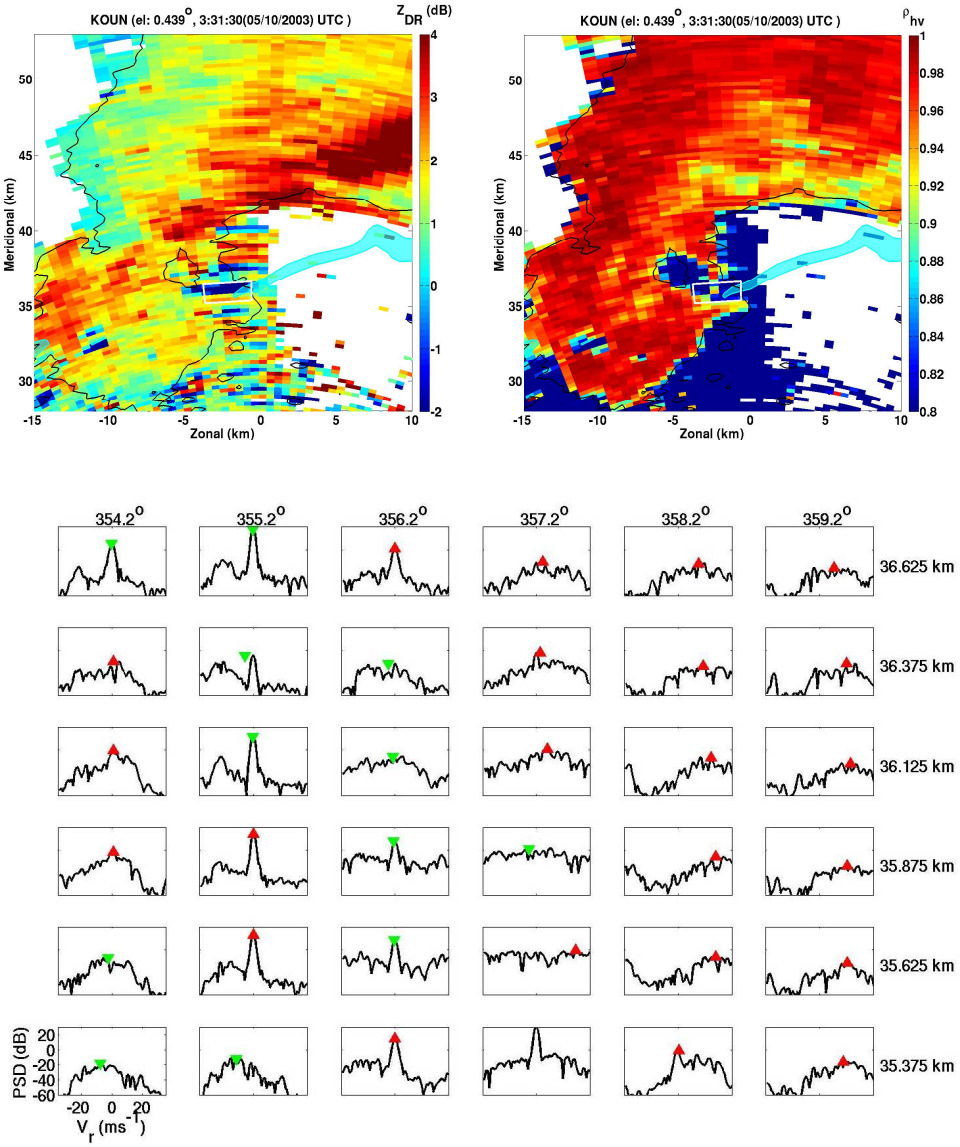

Figure 6.2: Examples of differential reflectivity (top left), cross-correlation coefficent (top right) and Doppler spectra within the white box (bottom) at 331 UTC 10 May 2003

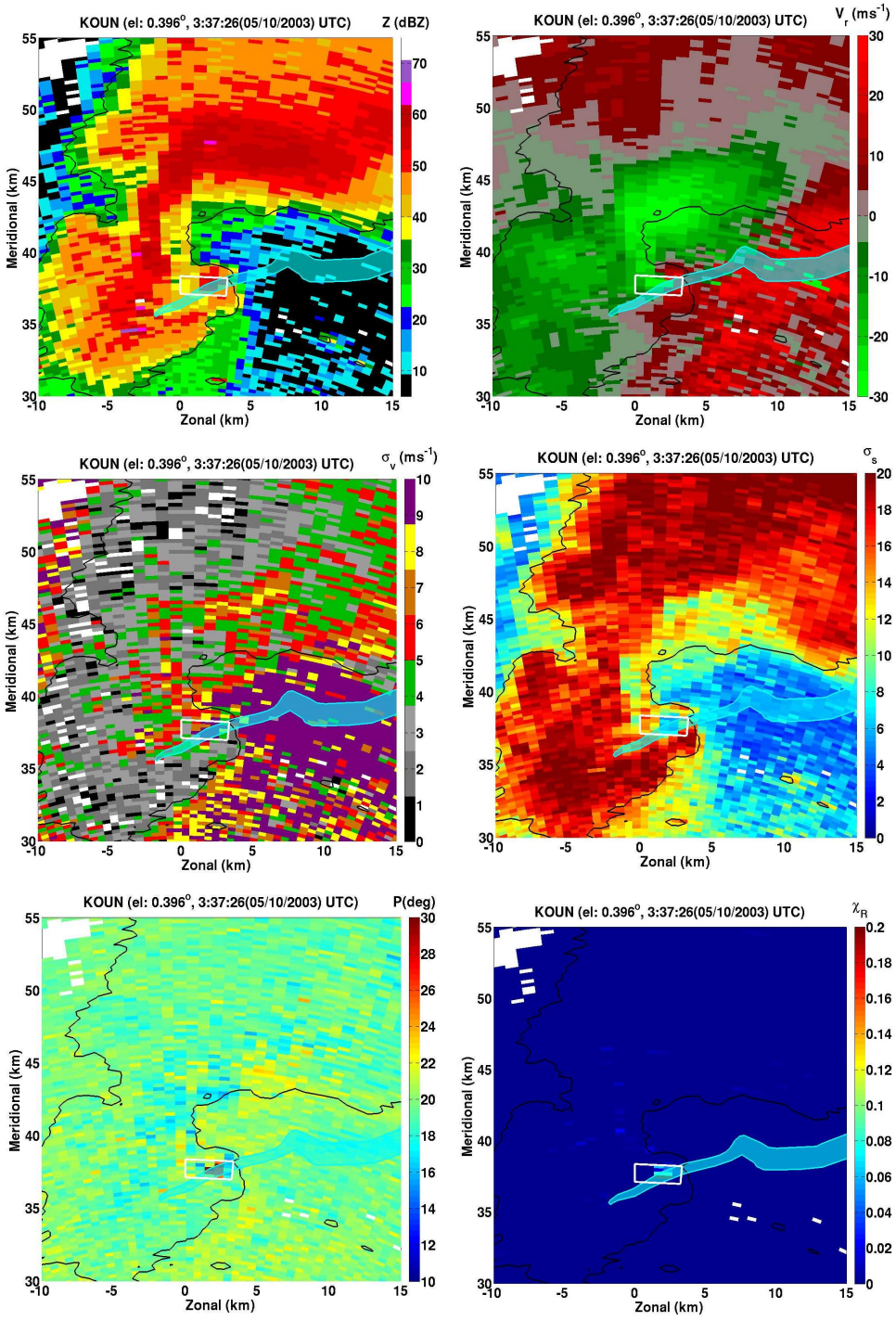

Figure 6.3: Similar to Fig. 6.1 but at 337 UTC 10 May 2003

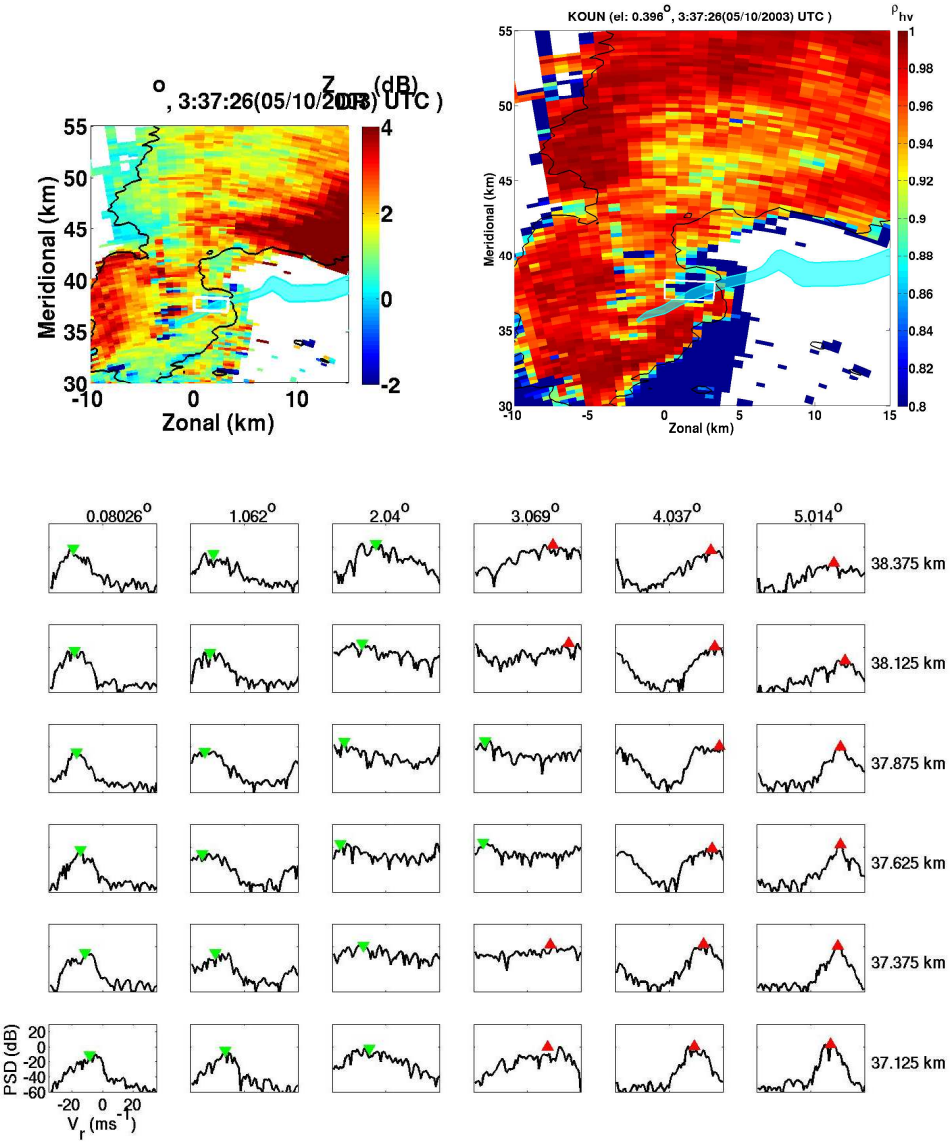

Figure 6.4: Similar to Fig. 6.2 but at 337 UTC 10 May 2003

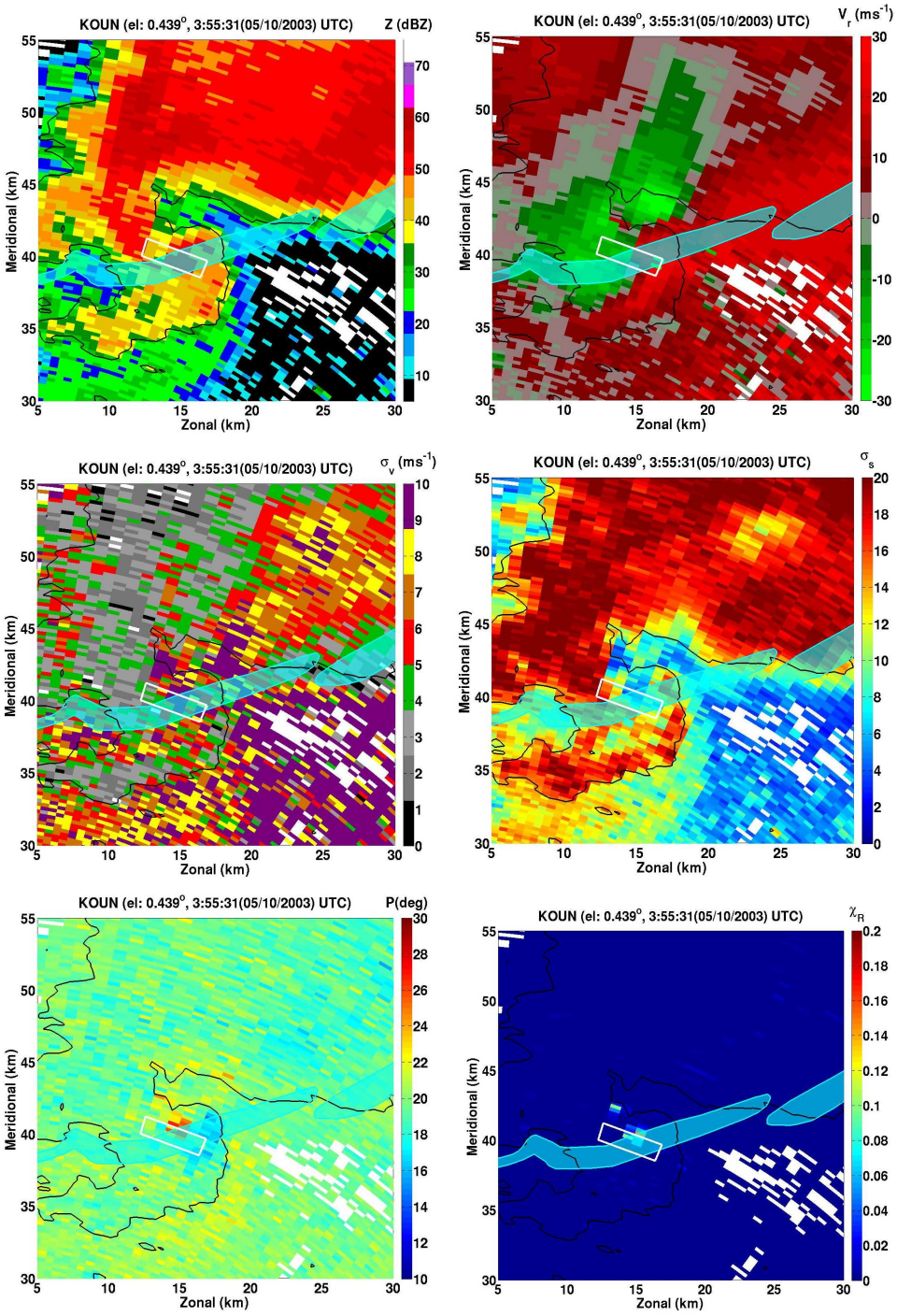

Figure 6.5: Similar to Fig. 6.1 but at 355 UTC 10 May 2003

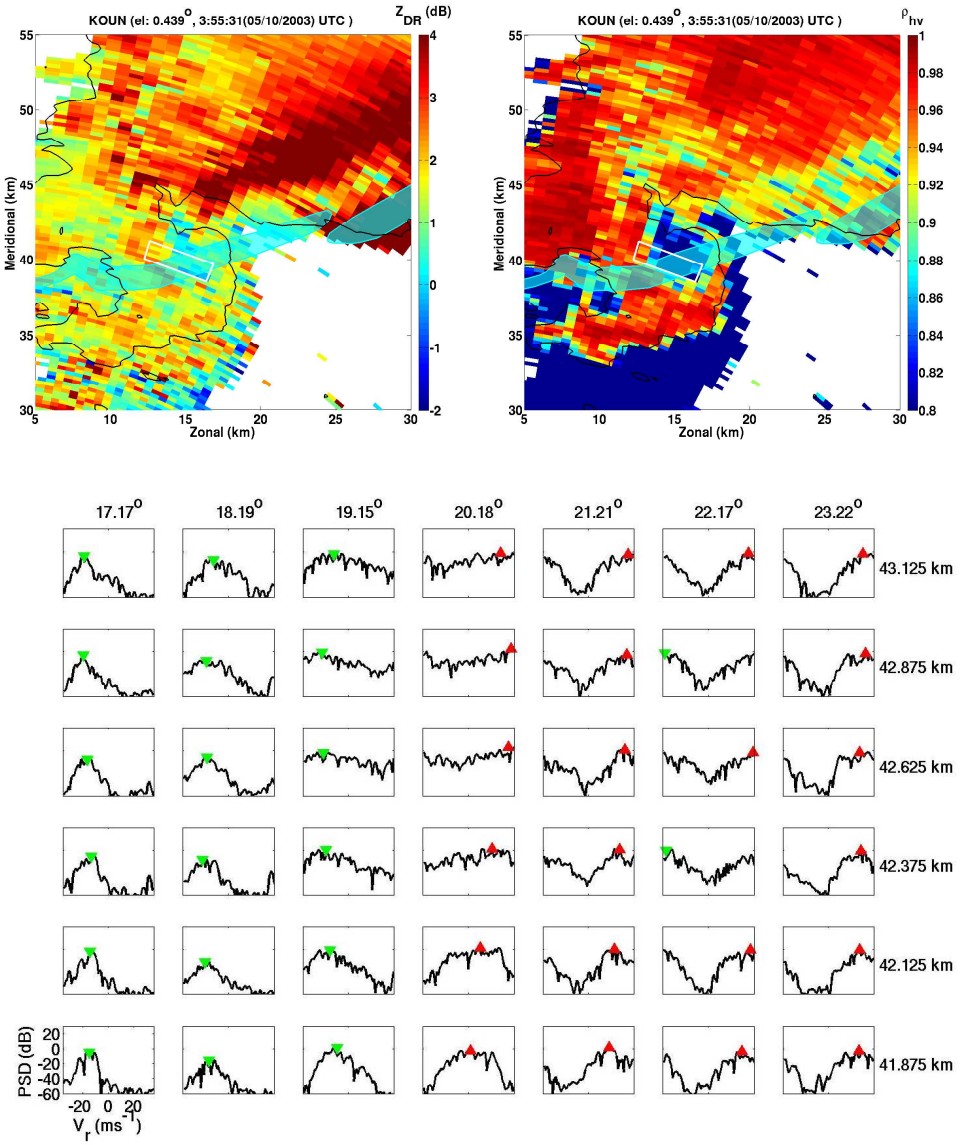

Figure 6.6: Similar to Fig. 6.2 but at 355 UTC 10 May 2003

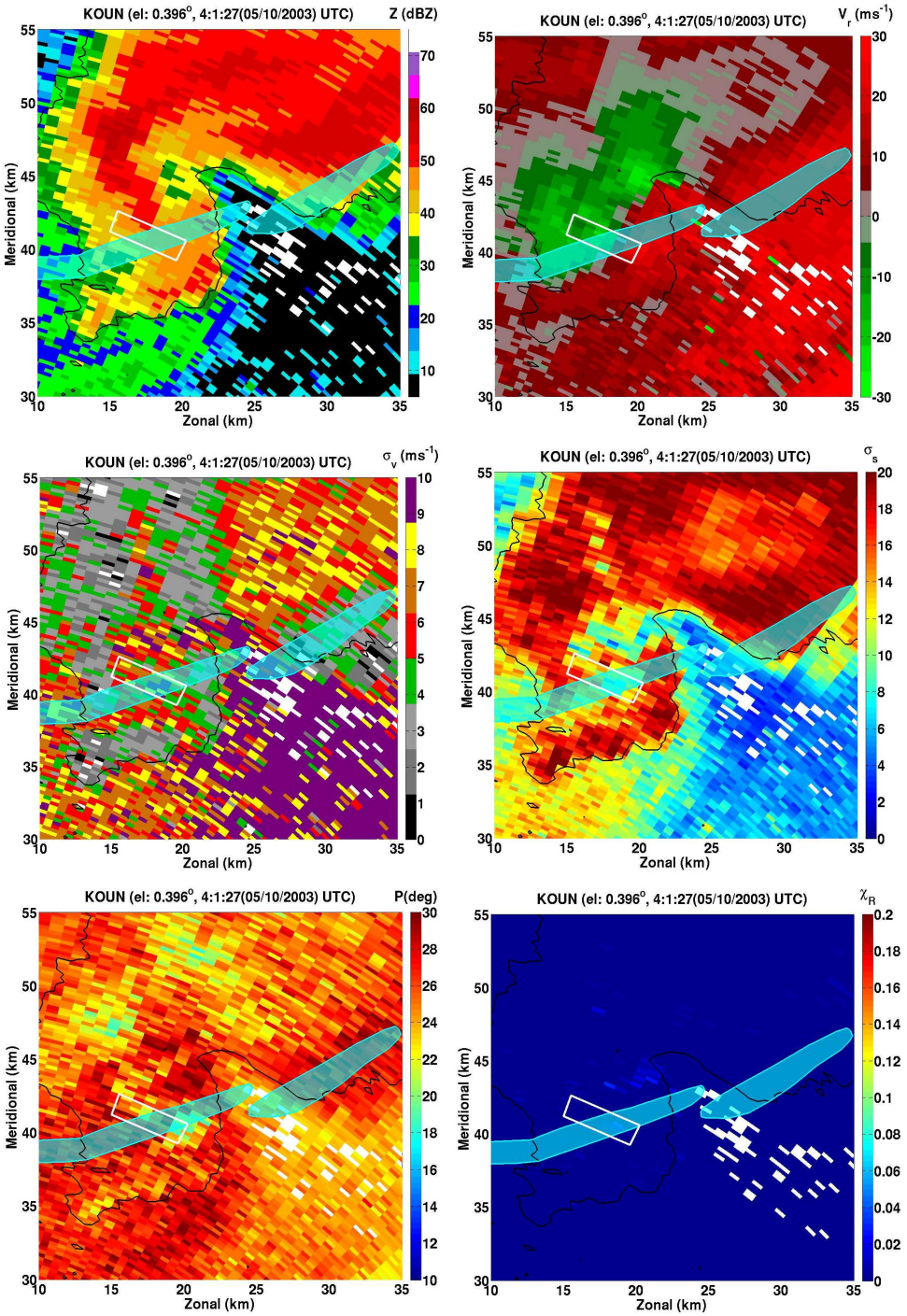

Figure 6.7: Similar to Fig. 6.1 but at 401 UTC 10 May 2003

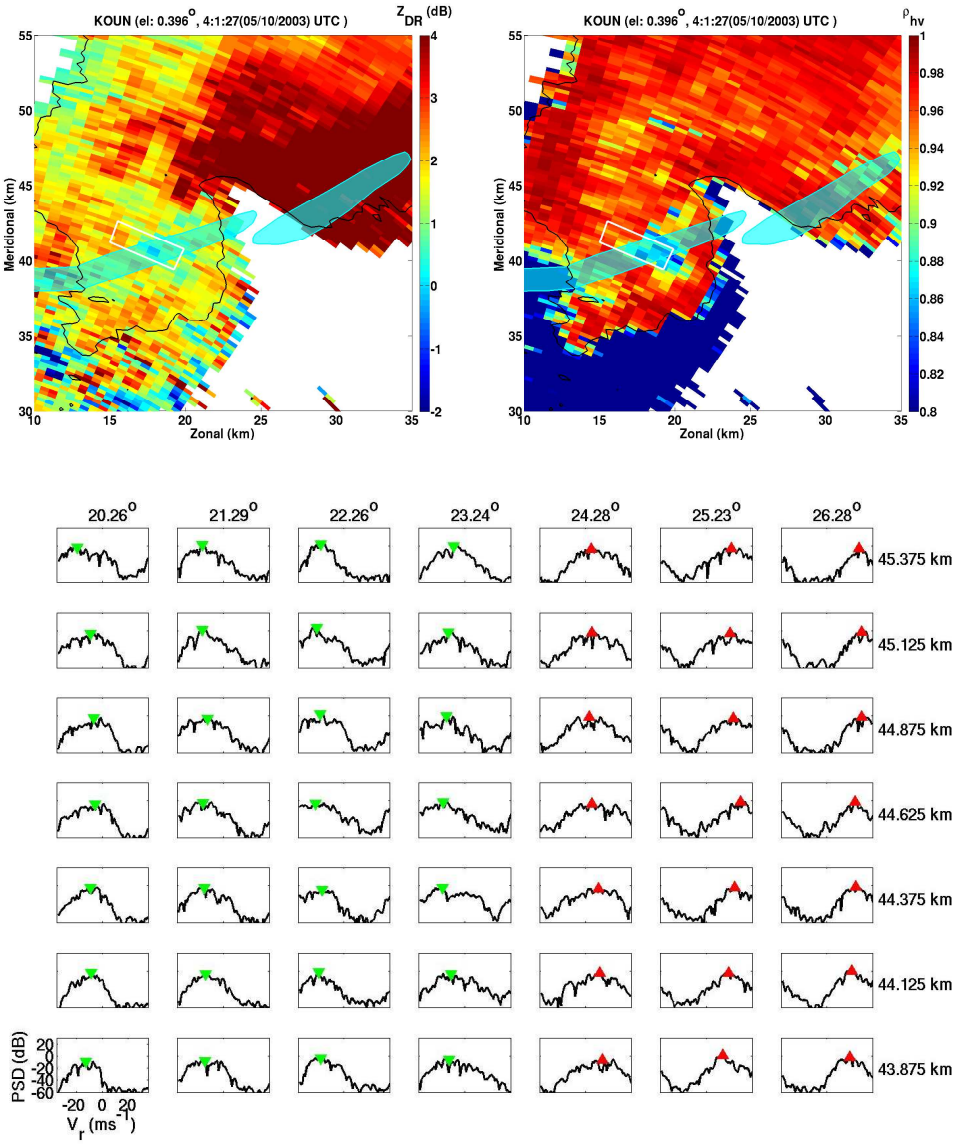

Figure 6.8: Similar to Fig. 6.2 but at 401 UTC 10 May 2003

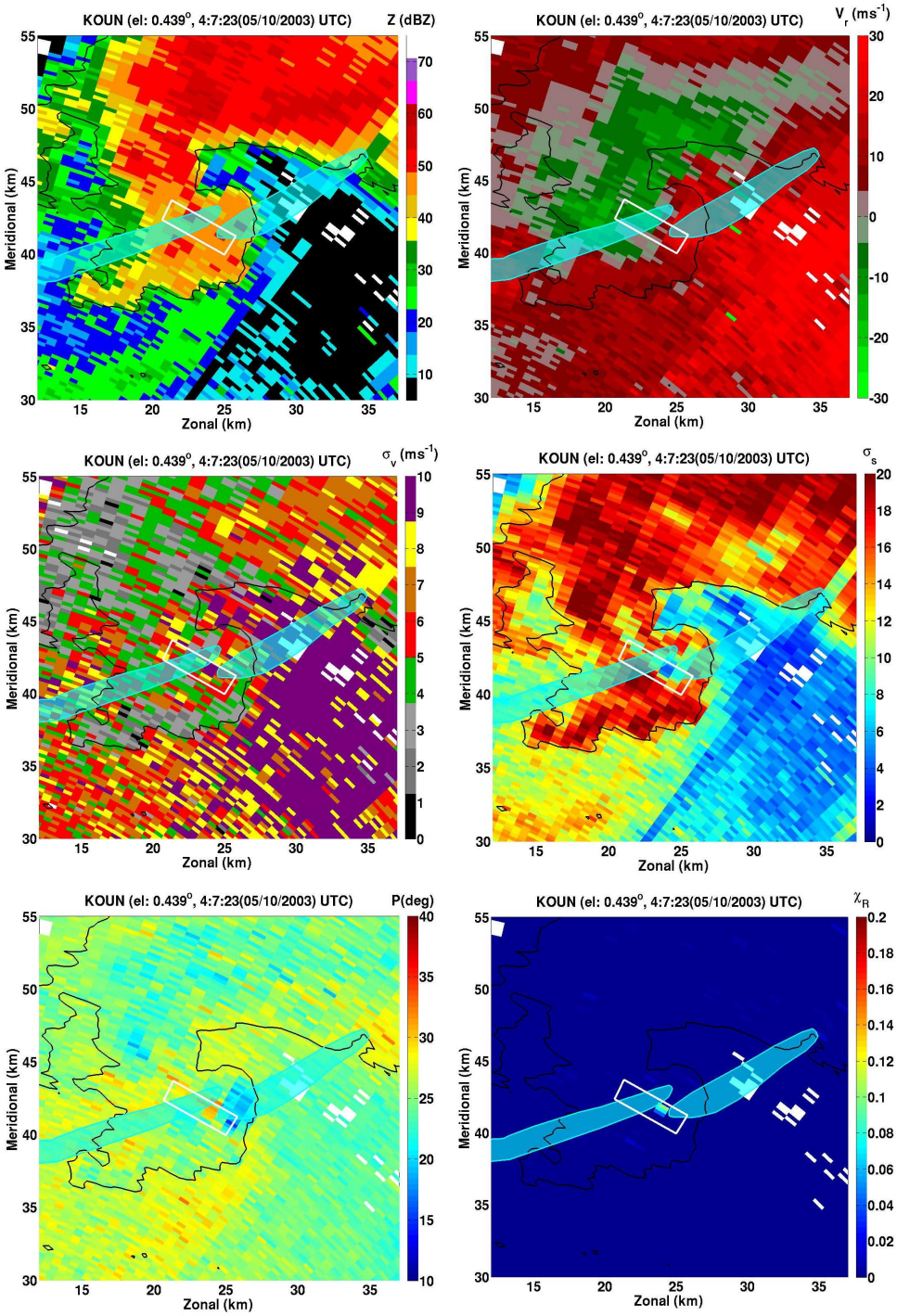

Figure 6.9: Similar to Fig. 6.1 but at 407 UTC 10 May 2003

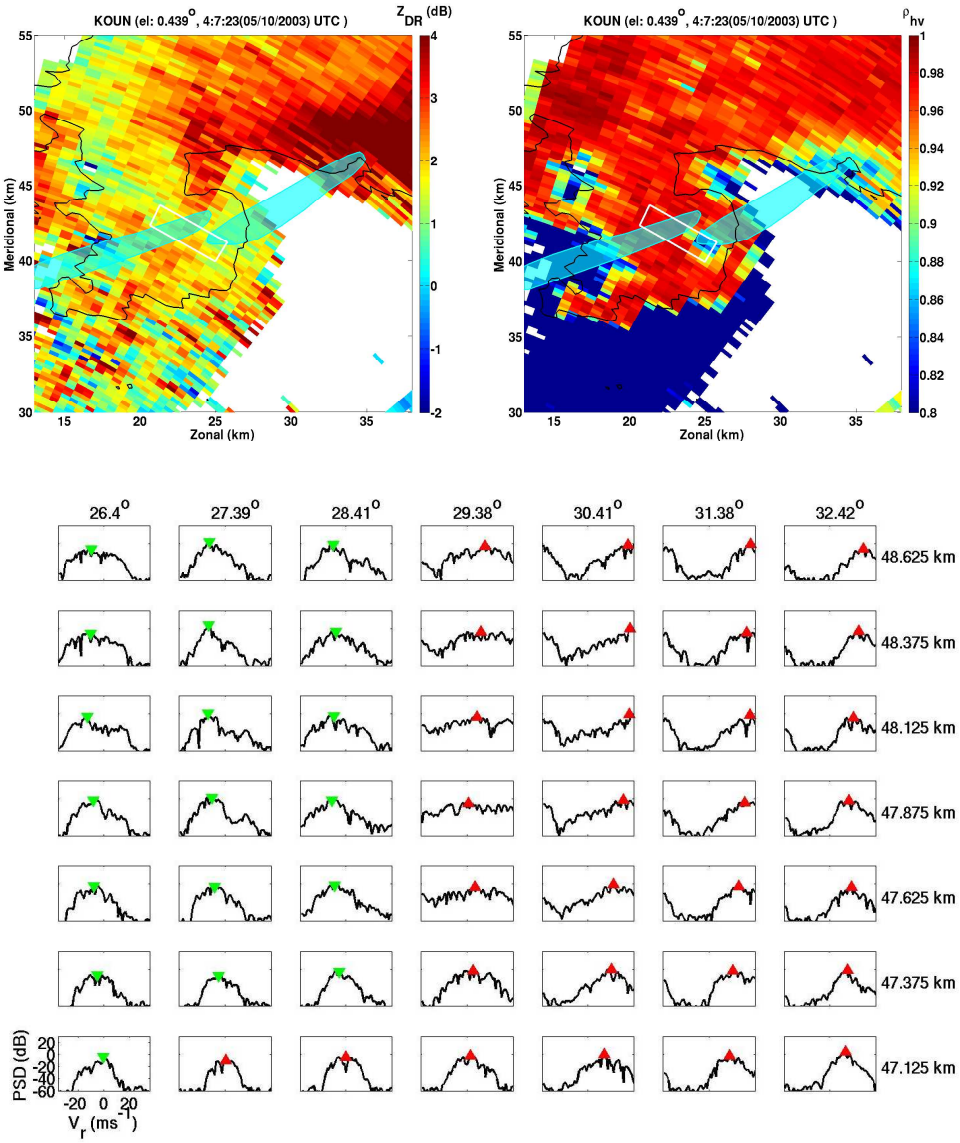

Figure 6.10: Similar to Fig. 6.2 but at 407 UTC 10 May 2003

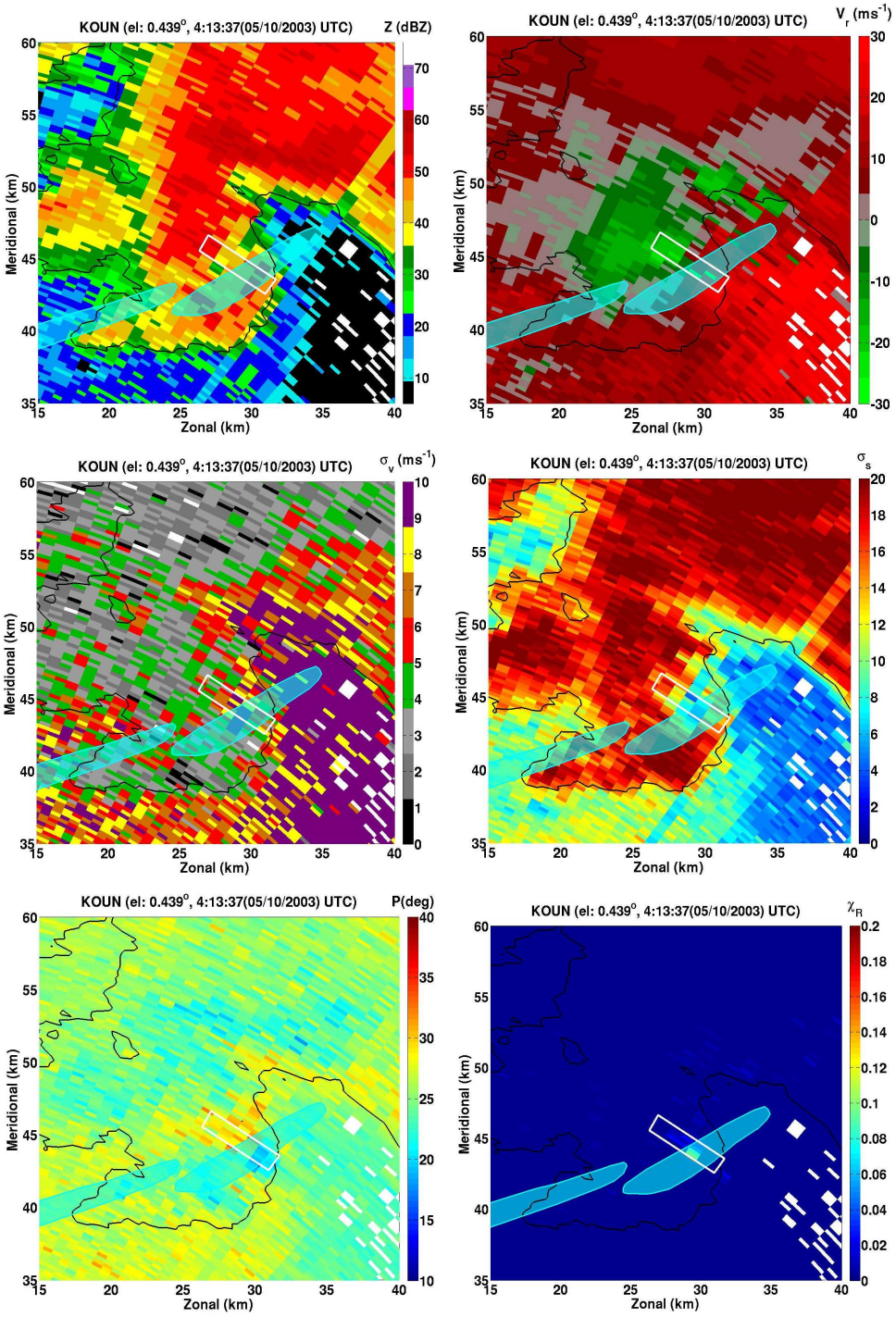

Figure 6.11: Similar to Fig. 6.1 but at 413 UTC 10 May 2003

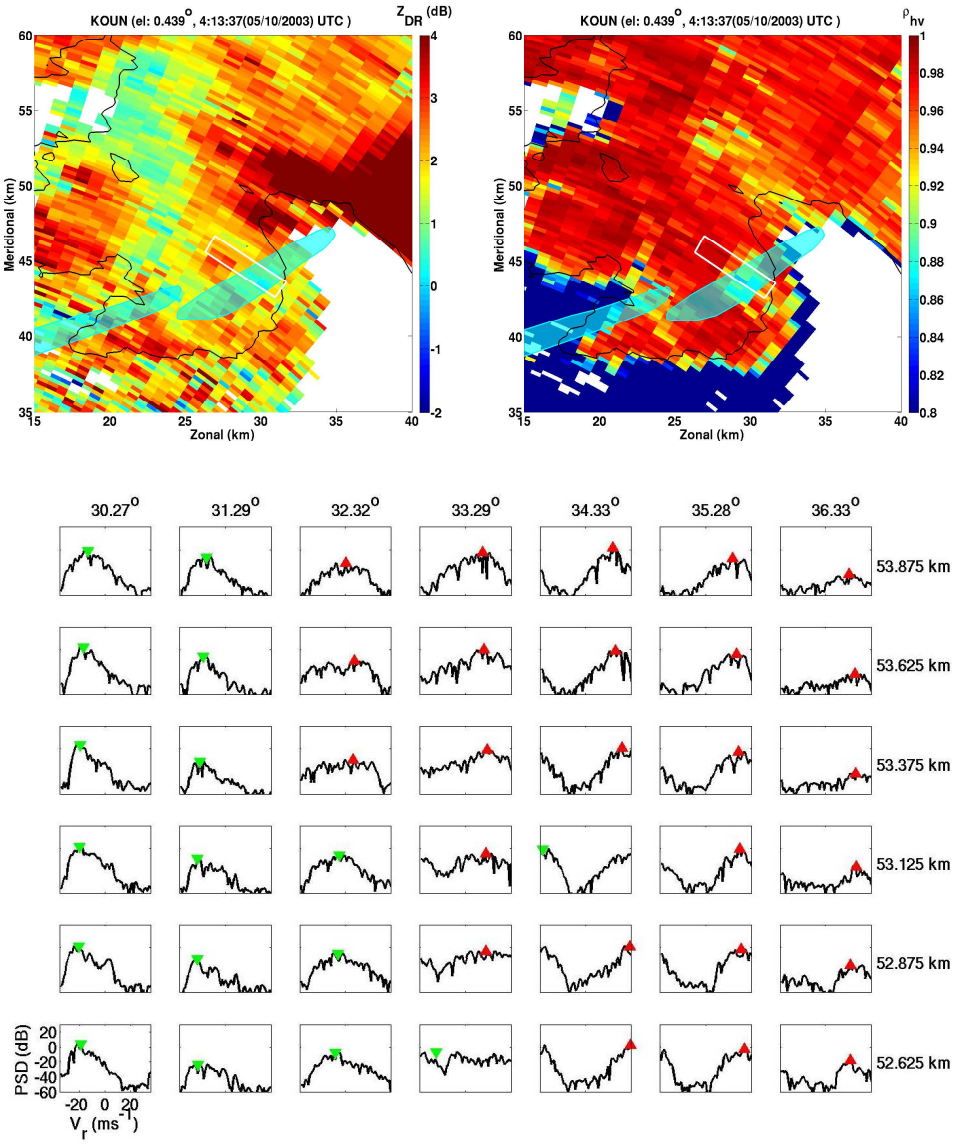

Figure 6.12: Similar to Fig. 6.2 but at 413 UTC 10 May 2003

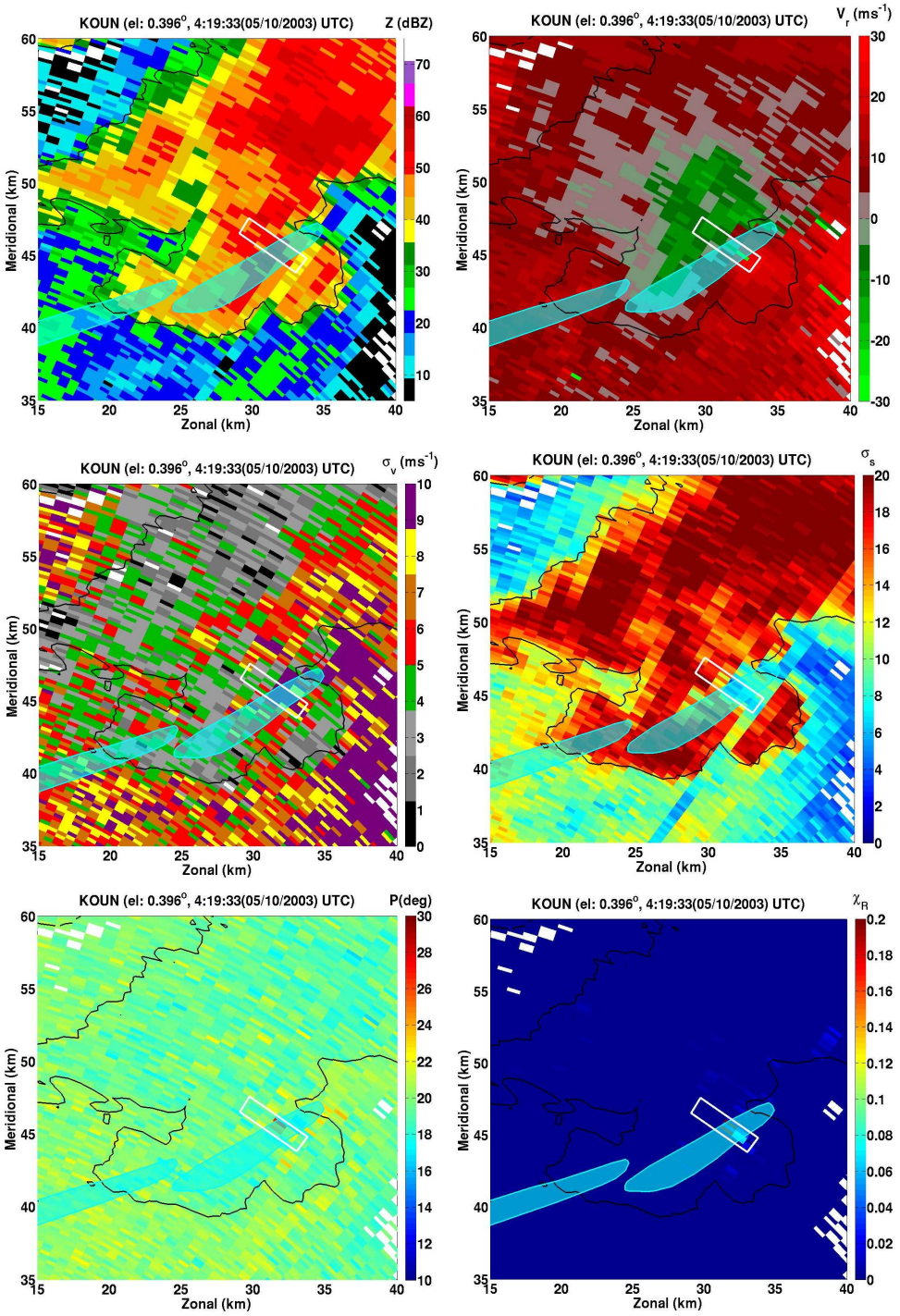

Figure 6.13: Similar to Fig. 6.1 but at 419 UTC 10 May 2003

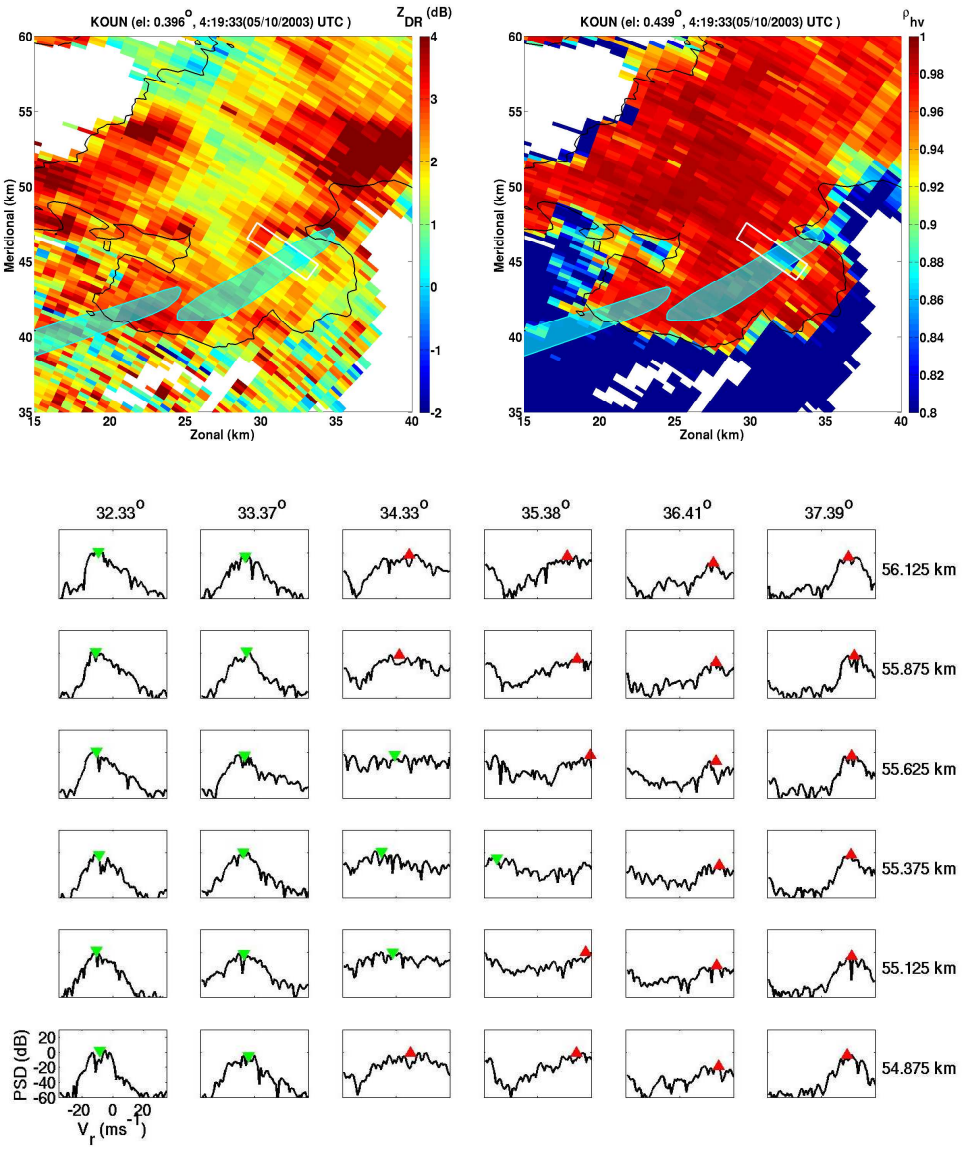

Figure 6.14: Similar to Fig. 6.2 but at 419 UTC 10 May 2003